Chapter A4 of the book:
Quantum Information Processing: Lecture Notes of the 44th IFF
Spring School 2013, Ed: David P. DiVincenzo, Juelich, 2013.

A 4 Superconducting Qubits

William D. Oliver
MIT Lincoln Laboratory
Lexington, MA, U.S.A.

Contents

1 Introduction

Superconducting qubits are solid-state artificial atoms, comprising lithographically defined Josephson tunnel junctions and superconducting interconnects [1]. When cooled to milli-Kelvin temperatures, these superconducting circuits exhibit quantized states of flux, charge, or junction phase depending on design parameters. Such superconducting artificial atoms have already proven a useful vehicle for advancing the scientific community's general understanding of coherence, quantum mechanics, and atomic physics, particularly in regimes not easily accessible with natural atoms and molecules. Their potential for lithographic scalability, compatibility with microwave control, and operability at nanosecond time scales make superconducting qubits a promising candidate for quantum information science and technology applications.

Spectacular improvement in the capabilities of superconducting qubits over the past decade has brought these qubits from a scientific curiosity to the threshold of technological reality [2]. Many individual efforts contributed to this improvement, starting with the demonstration of nanosecond-scale coherence in a Cooper pair box by Nakamura and co-workers [3] in 1999. In 2002, Vion *et al.* [4] developed a qubit with T_2 coherence time of hundreds of nanoseconds based on the concept of design and operation at first-order noise-insensitive bias points. Burkard *et al.* [5] elucidated the importance of symmetry in qubit designs, which in conjunction with Bertet *et al.* brought persistent-current flux qubit coherence times into the few microsecond range [6]. In 2005-2006, Ithier *et al.* [7] and Yoshihara *et al.* [8] measured extensively the noise properties of superconducting qubits to better understand the sources of decoherence. The "transmon" qubit developed by Schoelkopf and co-workers significantly reduced the charge sensitivity of the Cooper pair box, which would later bring microsecond times to the cavity-QED architecture [9, 10]. The MIT/NEC group increased T_2 above 20 μs with a persistent-current flux qubit in a 2D geometry using dynamical decoupling sequences [11], and the 3D-cavity approach developed at Yale [12] and now used by several groups has further increased this time above 100 μs [13] with as-yet unpublished reports above 150 μs. This *five-orders-of-magnitude* improvement in the primary single-qubit metric can be justly termed a "Moore's Law for quantum coherence" [14], approaching levels required for a certain class of quantum error correction codes (surface codes) [15, 16, 17]. In addition, the control of single- [18, 19, 20, 21] and coupled [22, 23] qubits has also advanced, with reports of gate fidelities as high as 99.85% [21].

In conjunction with these improvements, there have been numerous, increasingly sophisticated demonstrations involving quantum coherence in these systems. A few examples (in an admittedly incomplete list) include: coherent superpositions of macroscopic states [24, 25, 26], coherent and Rabi oscillations [3, 4, 27, 28, 29, 30, 31, 32, 33, 34, 35] in multiple qubit modalities, including a very long-lived (0.2 ms) CPB [36], Landau-Zener transitions [37], Stueckelberg oscillations [38, 39, 40, 41, 42, 43], microwave cooling [44, 45, 46, 47, 48, 49], amplitude spectroscopy [50, 51], electromagnetically induced transparency [52, 53] and coherent population trapping [54], geometrical phase [55], and cavity quantum electrodynamics [56, 57, 58, 59, 60, 61, 62, 63]. Significant progress has also been made toward their application to quantum information science [64, 65, 66], including state initialization [44, 49], tunable [67, 68, 69, 70, 71, 72] and long-distance [73, 74] coupling, quantum control [75, 76, 77, 78, 79, 80], quantum state [81, 133] and process [83, 84] tomography, randomized benchmarking [18, 19, 20, 21], measurement [85, 86, 87, 88, 89, 90, 91, 92, 93, 94, 95, 96, 97], architectures [16, 98, 99], preliminary demonstrations of error correction (without feedback) [100], and algorithm demonstrations [101, 102].

Based on these advances, there is a growing motivation to make further improvements and, indeed, there remains much work to do. The intrinsic and spin-echo T_2 times are generally not T_1-limited (i.e., $T_2 < 2T_1$) in the longest-lived samples (although exceptions do exist, e.g., Ref. [11]). Inhomogeneous dephasing arises from low-frequency (e.g., $1/f$-type) noise, although its microscopic origin is not yet well understood. The limiting source(s) of energy relaxation also remain unclear. Ideally, coherence times should be made as high as possible, as exceeding quantum error correction (QEC) thresholds reduces considerably their resource requirements. There is a general consensus within the community that understanding and mitigating sources of decoherence in superconducting qubits is one key that will enable more-advanced circuits and systems engineering [1].

In this light, these lecture notes serve to provide an admittedly brief overview of superconducting qubits with a focus on:

- survey of junctions and qubits
- noise spectroscopy and decoherence mitigation
- single qubit control.

We have made an effort to include relevant references so that interested readers can follow up on specific topics in more detail. Of course, in doing so, we have most certainly missed topics and references that deserve to be included. We also err on the side of presenting our own work a bit too much. While this can be somewhat annoying to readers, particularly to those who work in this field and are familiar with the broad range of excellent works available, our intent is to present experiments with an authority that comes from first-hand experience and not necessarily to ascribe to them a special status. In this spirit, we hope the reader finds this review useful.

2 Survey of Josephson junctions and superconducting qubit modalities

2.1 Josephson junctions

2.1.1 Josephson equations

We begin this section with a review of the Josephson junction, the elemental building block of superconducting qubits. The Josephson junction is formed by two superconducting electrodes separated by an insulating tunnel barrier [103, 104, 105, 106]. It is described by two constituent Josephson equations.

A supercurrent flows through the device, even in the absence of a voltage, due to Josephson tunneling. The value of the supercurrent is determined by the phase difference between the superconducting order parameters of the two electrodes according to the first Josephson equation,

$$I = I_{\rm c} \sin \phi \tag{1}$$

where $I_{\rm c}$ is the critical current of the junction and ϕ is the phase difference across it. The critical current is related to the superconducting gap of the electrode materials as well as the type and thickness of the insulating barrier. It is often characterized by a critical current density $J_{\rm c}$ and

the area A of the junction such that $I_c = J_c \times A$. The second Josephson equation relates the time evolution of the phase to the voltage drop across the junction;

$$V = \frac{\Phi_0}{2\pi}\frac{d\phi}{dt} \tag{2}$$

where $\Phi_0 \equiv h/2e$ is the superconducting flux quantum with value,

$$\Phi_0 = 2.07 \times 10^{-15}\ \text{Wb} = 2.07\ \text{mA} \cdot \text{pH} = 2.07\ \text{mV} \cdot \text{ps}. \tag{3}$$

Importantly for superconducting qubits, the Josephson junction exhibits a dynamic inductance inductance L_J that is nonlinear in the junction phase. Using the relation $V = L_J dI/dt$ with Eqs. 1 and 2, the standard definition for the Josephson inductance is:

$$L_J = \frac{\Phi_0}{2\pi I_c \cos\phi} = \frac{\Phi_0}{2\pi(I_c^2 - I^2)^{1/2}} = \frac{\Phi_0}{2\pi I_c(1-\gamma^2)^{1/2}} \equiv \frac{L_{J0}}{(1-\gamma^2)^{1/2}}, \tag{4}$$

where $\gamma \equiv I/I_c$ is the reduced current, L_{J0} is the inductance at $I = 0$, and $I < I_c$ is assumed. The inductance increases with current I and diverges as $I \to I_c$. An alternative definition that includes the time dependence of the inductance, $V = d\left[L_J I\right]/dt$, and does not diverge is given in Ref. [91]. In the $I \to 0$ limit, these two definitions both give L_{J0}.

For completeness, if the junction is biased with a constant voltage then the current will oscillate according to the relation (using Eqs. 1 and 2),

$$I = I_c \sin\left(\phi_0 + \frac{2\pi}{\Phi_0}\, V\, t\right) \tag{5}$$

with a frequency-to-voltage factor $483.6\ \text{MHz}/\mu V$. In turn, a transient fluctuation of the current through the junction will transiently change the phase creating a transient voltage fluctuation across the junction.

2.1.2 RCSJ model

A "short" Josephson junction may be modeled using the "resistively- and capacitively shunted junction" (RCSJ) model (the Stewart-McCumber model [107, 108]). It is sometimes just called the RSJ model. Here, "short" means that the junction is smaller than the typical length scale of variations in the Josephson phase (the size of a Josephson vortex), around $10 - 30\ \mu\text{m}$ for typical qubit materials [109]; qubit junctions tend to be much smaller than this. Within this model, the junction itself is an element that obeys Eqs. 1 and 2, in parallel with a capacitor (essentially a parallel plate capacitor due to the electrodes and tunneling barrier) and a resistor which models the intrinsic loss of the junction. When the junction is in its normal state ($I > I_c$), the Josphson element is omitted and the junction resistance is the normal tunneling resistance R_n. This resistance can be related to I_c through the Ambegaokar-Baratoff relation [110],

$$\frac{\pi}{4}V_{\text{gap}}(\Theta) = \frac{\pi}{4}\frac{2\Delta(\Theta)}{e} = I_c R_n \tag{6}$$

where $V_{\text{gap}} = 2\Delta/e$ is the total gap voltage for a Cooper pair, Δ is the temperature-dependent superconducting gap and Θ is temperature. For currents less than I_c, the resistance is the "subgap resistance" R_{sg}, which is explicitly manifest in the hysteretic $I - V$ trace of a junction.

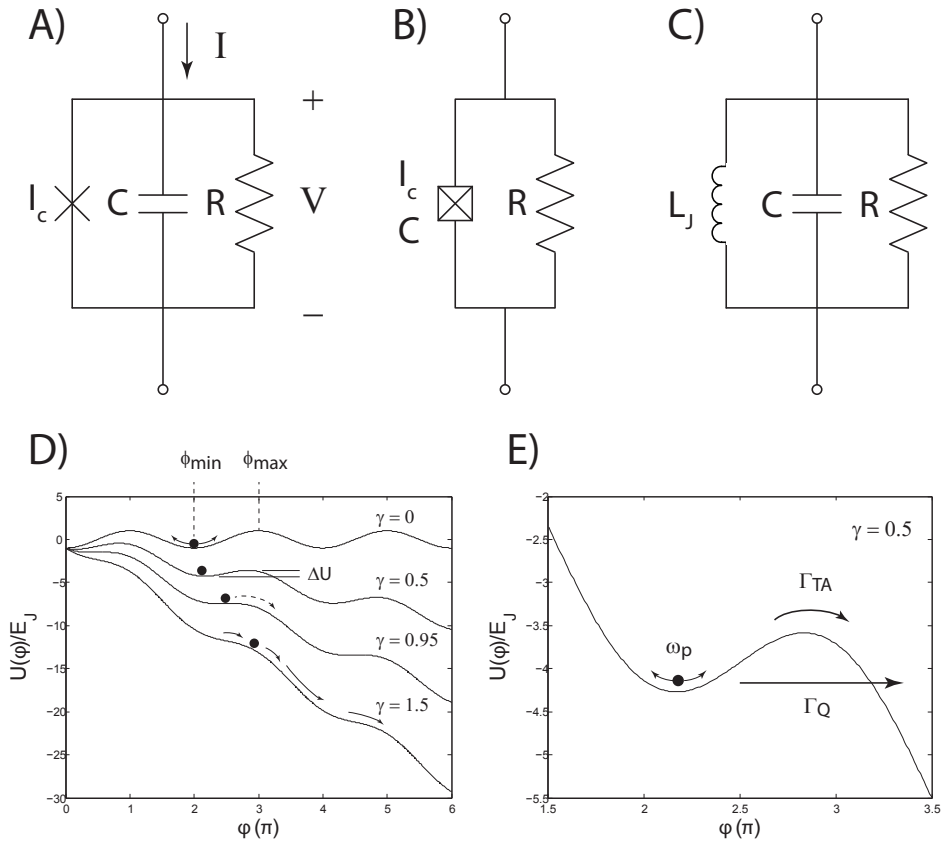

Fig. 1: A) *RCSJ model for a Josephson junction. The X indicates the junction with critical current $I_{\rm c}$, in parallel with a capacitor C and resistor R which damps the junction.* **B)** *Equivalent circuit using the "boxed-X" to represent the junction and its capacitance.* **C)** *Equivalent circuit that replaces the junction with an inductor that has the value of the Josephson inductance. The parallel combination is a resonant circuit oscillating at the plasma frequency.* **D)** *Washboard potential U for several values of reduced current γ. This potential represents the dynamics of the RCSJ model. For $\gamma = 0$, the "phase particle" representing the junction state is trapped in a well and oscillates at the plasma frequency. As γ is increased, the potential tilts. As $\gamma \rightarrow 1$, the phase particle may diffuse around the washboard, being occasionally retrapped by the damping. While ϕ is changing with time, a voltage exists across the junction. For $\gamma > 1$, the particle runs down the washboard, and the junction is manifestly in the normal state.* **E)** *Phase particle in a single well at $\gamma = 0.5$. The particle may escape the well due to thermal activation over the barrier with a rate $\Gamma_{\rm TA}$, or due to quantum tunneling through the well with a rate $\Gamma_{\rm Q}$.*

Ideally, a major component of the subgap resistance is due to equilibrium quasiparticles with resistance $R_{\rm qp} = R_{\rm n} \exp[\Delta/k_{\rm B}\Theta]$. In practice, at the $10 - 100$ mK temperatures used for superconducting qubits, the apparent losses are higher (*e.g.,* excess non-equilibrium quasiparticles) and the RCSJ model resistance may be used to parameterize the observed loss.

The circuit equation for the RCSJ model is obtained by summing the current along the three parallel paths (element, capacitor, and resistor),

$$I = I_{\rm c} \sin\phi + \frac{V}{R} + C\frac{dV}{dt} \tag{7}$$

$$= I_{\rm c} \sin\phi + \frac{1}{R}\frac{\Phi_0}{2\pi}\dot{\phi} + C\frac{\Phi_0}{2\pi}\ddot{\phi} \tag{8}$$

where the "dot" indicates time derivative. Bringing the current I over to the right side casts the equation in the form of a particle with "mass" $m \equiv C(\Phi_0/2\pi)^2$ in a tilted washboard potential $U(\phi)$,

$$0 = \frac{\partial U(\phi)}{\partial \phi} + m\frac{1}{RC}\dot{\phi} + m\ddot{\phi} \tag{9}$$

where the potiential $U(\phi)$ is

$$U(\phi) = E_{\rm J}\left(-\gamma\phi - \cos\phi\right), \tag{10}$$

and we have defined the Josephson energy $E_{\rm J} \equiv I_{\rm c}\Phi_0/2\pi$.

These equations describe a particle with mass m in a washboard potential that can be tilted by applying a current γ. If the well is not tipped too much, the particle remains in a single well. For small oscillations, the particle oscillates with a finite-bias plasma frequency $\omega_{\rm p}$ related to the curvature of the potential,

$$\omega_{\rm p} = \sqrt{\frac{1}{m}\frac{d^2U(\phi)}{d\phi^2}} = \frac{1}{\sqrt{L_{\rm J}C}} = \omega_{\rm p0}(1-\gamma^2)^{1/4} \tag{11}$$

$$\omega_{\rm p0} = \frac{1}{\sqrt{L_{\rm J0}C}} \tag{12}$$

where $\omega_{\rm p0}$ is the zero-bias, Josephson plasma frequency, defined in terms of the $I = 0$ Josephson inductance $L_{\rm J0}$ and the capacitance C. If the well is tilted too much, the particle will escape and start "running" down the washboard. A voltage develops across the junction, related to the temporal change in ϕ associated with the moving particle. There is also a damping term in Eq. 9 proportional to the phase velocity with a "viscous damping" coefficient m/RC. The dampling acts to localize the particle in a well such that, for moderate tilting, the particle may diffuse around the washboard, occasionally being retrapped by the damping.

2.1.3 Thermal activation

In the thermal regime ($k_{\rm B}\Theta \gg \hbar\omega_{\rm p}$), the rate at which a particle escapes from a well is related to thermal activation over the potential barrier ΔU,

$$\begin{aligned}\Delta U &= U(\phi_{\rm max}) - U(\phi_{\rm min}) \\ &= 2E_{\rm J}\left[\sqrt{1-\gamma^2} - \gamma\arccos(\gamma)\right] \\ &\approx E_{\rm J}\frac{4\sqrt{(2)}}{3}\left(1-\gamma\right)^{3/2}\end{aligned} \tag{13}$$

where $\phi_{\max} = \pi - \arcsin(\gamma)$ is the phase at the local maximum of the potential, $\phi_{\min} = \arcsin(\gamma)$ is the phase at a local minimum of a well, and the approximation holds for currents approaching the critical current, $\gamma \to 1$ [109, 113].

In the presence of Ohmic damping [111], the escape rate is

$$\Gamma_{\rm TA} = a_{\rm t} \frac{\omega_0}{2\pi} e^{-\frac{\Delta U}{k_{\rm B}\Theta}} \tag{14}$$

which contains the usual Arrhenius factor $\exp(-\Delta U/k_{\rm B}\Theta)$, an "attempt rate" to escape $\omega_0/2\pi$, and a prefactor $a_{\rm t}$ that incorporates the effect of damping [112],

$$a_{\rm t} = \frac{4a}{\left[(1 + Qk_{\rm B}\Theta/1.8\Delta U)^{1/2}\right]^{1/4}} \tag{15}$$

and contains the junction quality factor $Q = \omega_{\rm p} RC$ [113, 114, 115, 116]. Higher Q values correspond to lower damping.

2.1.4 Macroscopic quantum tunneling

The presence of a potential well raises the question, "Does a Josephson junction degree of freedom (the phase) exhibit quantum mechanical behavior?" In a series of papers foundational to the field of superconducting qubits, Clarke, Devoret, Esteve, and Martinis demonstrated that a junction indeed exhibits quantum mechanical tunneling through the junction's washboard potential barrier in addition to thermal activation over the barrier [113, 114, 115, 116].

The escape rate $\Gamma_{\rm TA}$ due to thermal activation has the property that it should go to zero as temperature is decreased to zero due to the Arrhenius factor $\exp(-\Delta U/k_{\rm B}\Theta)$. However, quantum tunneling provides another means of escape which becomes dominant and saturates the total escape rate at low temperatures. In the quantum regime ($k_{\rm B}\Theta \ll \hbar\omega_{\rm p}$), to lowest order in $1/Q$, the quantum tunneling rate at zero temperature is

$$\Gamma_{\rm Q} = \frac{a_{\rm q}\omega_{\rm p}}{2\pi} e^{\left[-\frac{7.2\Delta U}{\hbar\omega_{\rm p}}\left(1+\frac{0.87}{Q}\right)\right]} \tag{16}$$

where $a_{\rm q} \approx \left[120\pi(7.2\Delta U/\hbar\omega_{\rm p})\right]^{1/2}$ [115]. Dissipation suppresses quantum tunneling through the factor $1/Q$, and so a signature of quantum tunneling is one indication that Josephson junctions can have low dissipation.

Conceptually, the escape rate is measured at a particular current $I < I_{\rm c}$ while the junction is in the zero-voltage state, and then this current is stepped to find the escape rate for different barrier heights. In practice, the escape-rate measurements can be implemented by a different means: ramping the current through the junction at a rate slow compared with the other rates in the problem. One then records the current (or, equivalently, the time from the start of a linear current ramp) at which the junction switches to the normal state. Note that this current is properly called the "switching current" and not the "critical current," because thermal or quantum escape mechanisms will generally act before the critical current is reached. This experiment is repeated many times (typically thousands) to build up the switching-current distribution, from which the escape rate can be calculated [117]. The escape rate measurement is repeated as a function of the junction's ambient temperature, and the rate was shown to saturate at a particular "escape temperature" as the ambient temperature was reduced, an observation consistent with a quantum tunneling picture [115, 116]. For details related to these experiments, the reader is directed to the cited references and the references therein.

2.2 DC SQUID: a tunable junction

The DC SQUID (superconducting quantum interference device) is a superconducting loop interrupted by two junctions [118]. The net critical current of the SQUID can be tuned by threading a magnetic flux through the loop. In this sense, the SQUID is a tunable Josephson junction, and this feature is used to make "tunable" superconducting qubits, *i.e.,* qubits with a parameter related to the junction $I_{\rm c}$ that is tunable by the magnetic field that threads the SQUID loop.

2.2.1 DC SQUID equations

A SQUID is a superconducting loop interrupted by two junctions, as illustrated in Fig. 2A. A current I flows into the SQUID, and subsequently separates into two currents I_j in the branches ("arms") $j = 1, 2$. In each arm of the SQUID, there is a Josephson junction with critical current I_{cj}, phase ϕ_j, and Josephson inductance $L_{{\rm J}j}$ (not illustrated). There is also in general a geometric inductance L_j in each arm. The total inductance around the loop is L. The current passing through branch j is given by the Josephson current equation (Eq. 1), such that the total current is

$$I = I_{\rm c1} \sin\phi_1 + I_{\rm c2} \sin\phi_2. \tag{17}$$

Alternatively, one may transform into a basis of symmetric ($I_{\rm p}$) and antisymmetric (circulating current, $I_{\rm m}$) currents:

$$I_{\rm p} = \frac{I_1 + I_2}{2} \tag{18}$$

$$I_{\rm m} = \frac{I_1 - I_2}{2} \tag{19}$$

$$I = 2I_{\rm p}. \tag{20}$$

Note that only $I_{\rm m}$ is illustrated in Fig. 2A.

An external magnetic field $B_{\rm ext}$ is applied to the SQUID, and it contributes a flux $\Phi_{\rm ext}$ to the loop, illustrated in Fig. 2B. The superconducting order parameter must be single valued, and this requirement imposes a quantization condition: the total phase difference around the loop must quantized in units of the flux quantum Φ_0. This comprises a normalized superposition of the externally applied flux, a screening flux due to the SQUID current and geometric inductances, and the Josephson junctions. This condition may be expressed as,

$$\begin{aligned} 2\pi n &= \frac{2\pi}{\Phi_0} \oint_C (\vec{A} + \Lambda \vec{J_s}) \cdot d\vec{l} = \oint_C \nabla\phi \cdot d\vec{l} \\ 2\pi n &= \phi_2 + \beta_{\rm L2} \sin\phi_2 - \phi_1 - \beta_{\rm L1} \sin\phi_1 - \phi_{\rm ext} \end{aligned} \tag{21}$$

where n is the number of flux quanta Φ_0, $\beta_{\rm L1,\,L2} \equiv L_{1,2}/L_{\rm J1,\,J2}$ are the ratios of the geometric inductance to the Josephson inductance for arms 1 and 2, $\beta_{\rm L1,\,L2} \sin\phi_{1,\,2}$ are the flux contributions due to current passing through the geometric inductances $L_{1,\,2}$ normalized by $\Phi_0/2\pi$, and $\phi_{\rm ext} = 2\pi\Phi_{\rm ext}/\Phi_0$ is the external flux normalized by $\Phi_0/2\pi$. Note that we have chosen a path in the center of the superconductor where the current $\vec{J_s}$ is negligible. This means that we have assumed the kinetic inductance contribution, related to $\Lambda\vec{J_s}$, is negligible (see Ref. [104]).

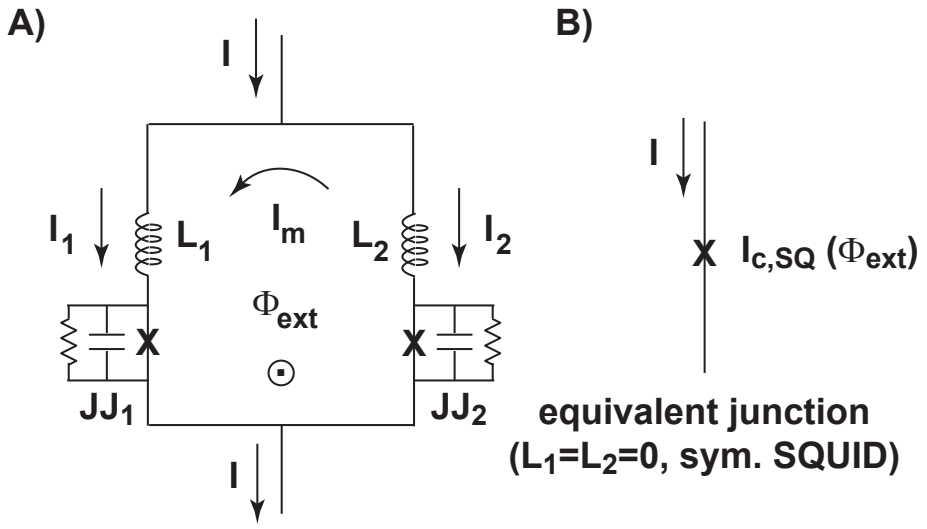

Fig. 2: **A)** *Circuit diagram of a SQUID. Current I enters and leaves the SQUID. The current I_j flows through branch $j = 1, 2$ with arm inductance L_j and a Josephson junction with phase critical current I_{cj}, phase ϕ_j, capacitance C_j, and damping resistor R_j. An external magnetic field B_{ext} threads a flux Φ_{ext} through the loop. A circulating current $I_{\rm m}$ develops in response to the applied flux.* **B)** *Equivalent Josephson junction with a critical current tuned by the external flux $\Phi_{\rm ext}$. The inductances are taken to be zero, and the equivalence is precise for symmetric SQUID junctions.*

2.2.2 Zero-inductance case, $I_{\rm c1} = I_{\rm c2}$

If the SQUID arm inductances are small compared with the Josephson inductancs, then the ratios $\beta_{\rm L1,\,L2}$ are negligible and can be dropped from Eq. 21. The equations for the SQUID current are:

$$I = I_{\rm c1}\sin\phi_1 + I_{\rm c2}\sin\phi_2 \tag{22}$$

$$2\pi n = \phi_2 - \phi_1 - \phi_{\rm ext}. \tag{23}$$

Furthermore, if one assumes the critical currents are equal, $I_{\rm c1} = I_{\rm c2} \equiv I_{\rm c}$, then these equations can be combine to yeild

$$I = 2I_{\rm c}\cos\left(\frac{\phi_{\rm ext}}{2}\right)\sin\left(\phi_1 + \frac{\phi_{\rm ext}}{2}\right). \tag{24}$$

The extrema occur for $dI/d\phi_1 = 0$, which leads to the relation (in terms of $\Phi_{\rm ext}$)

$$I_{\rm c,SQ}(\Phi_{\rm ext}) = 2I_{\rm c}\left|\cos\left(\frac{\pi\Phi_{\rm ext}}{\Phi_0}\right)\right|. \tag{25}$$

The critical current of the SQUID $I_{\rm c,SQ}$ is a function of the externally applied flux. As we show in Section 2.2.5, one may view the SQUID in Fig. 2A as a single junction with critical current given by Eq. 25, and a corresponding Josephson inductance that is now a function of both the current I and the SQUID flux $\Phi_{\rm ext}$ (Fig. 2B). The critical current can be tuned between 0 and $2I_{\rm c}$.

2.2.3 Zero-inductance case, $I_{c1} \neq I_{c2}$

In the case that the junctions have different areas and/or different critical current densities, their critical currents will not be identical. In this case, the critical currents can be tuned with the flux by the following expression (see Ref. [103] for a clever derivation),

$$I_{c,SQ}(\Phi_{ext}) = \left[I_{c1}^2 + I_{c2}^2 + 2I_{c1}I_{c2}\cos\left(\frac{2\pi\Phi_{ext}}{\Phi_0}\right)\right]^{1/2} \tag{26}$$

The form of Eq. 26 is indicative of an interference effect, and it will oscillate as a function of Φ_{ext} between a maximum $|I_{c1} + I_{c2}|$ and a minimum $|I_{c1} - I_{c2}|$. It reduces to Eq. 25 in the limit $I_{c1} = I_{c2}$.

2.2.4 Non-zero inductance case

The non-zero inductance case can be solved numerically (see Ref. [103] for an example using Lagrange multipliers to incorporate the quantization constraint). For a symmetric SQUID ($I_{c1} = I_{c2}$ and $L_1 = L_2$), the SQUID critical current $I_{c,SQ}(\Phi_{ext})$ modulates between its full value $2I_c$ and a non-zero minimum value $I_{c,min}$ that increases as the total inductance increases. For differing inductances ($L_1 \neq L_2$), the SQUID critical current $I_{c,SQ}(\Phi_{ext})$ becomes distorted with flux and is no longer symmetric about $\Phi_{ext} = 2\pi n$. One consequence is that the SQUID critical current will not be at its maximum value for $\Phi_{ext} = 0$. A similar asymmetry is used for convenience in the phase-qubit SQUID readout to obtain $dI_{c,SQ}/d\Phi_{ext} \neq 0$ sensitivity to an external magnetic field in the absence of a static bias, $\Phi_{ext} = 0$.

2.2.5 Equivalence to a Josephson junction

The formal equivalence between the SQUID (Fig. 2A) and a Josephson junction (Fig. 2B) can be clarified by writing the equation of motion for the SQUID while allowing for variations in component values. We adopt the following parameterization:

$$\mathcal{V} \equiv \frac{\mathcal{V}_1 + \mathcal{V}_2}{2} \tag{27}$$

$$\Delta\mathcal{V} \equiv \frac{\mathcal{V}_1 - \mathcal{V}_2}{2}, \tag{28}$$

in which $\mathcal{V}_{1,2}$ represents any pair of components, *e.g.*, the RCSJ critical currents, resistances, and capacitances. Using these definitions, one may write,

$$I_{c1} = I_c + \Delta I_c \qquad I_{c2} = I_c - \Delta I_c \tag{29}$$

$$G_1 = G + \Delta G \qquad G_2 = G - \Delta G \tag{30}$$

$$C_1 = C + \Delta C \qquad C_2 = C - \Delta C \tag{31}$$

where we have defined the normal-state conductances $G_{1,2} \equiv 1/R_{1,2}$ corresponding to the normal-state resistances $R_{1,2}$. We take the inductances in Fig. 2A to be zero to show the equivalence.

Following the approach of Section 2.1.2, current conservation yields the following equations for the SQUID current:

$$I = I_1 + I_2 = I_{c1}\sin\phi_1 + G_1\frac{\Phi_0}{2\pi}\dot{\phi}_1 + C_1\frac{\Phi_0}{2\pi}\ddot{\phi}_1 + I_{c2}\sin\phi_2 + G_2\frac{\Phi_0}{2\pi}\dot{\phi}_2 + C_2\frac{\Phi_0}{2\pi}\ddot{\phi}_2. \tag{32}$$

Using the Eq. 27 and Eq. 28, one may write,

$$I = I_0 + \Delta I \tag{33}$$

$$= I_{\rm c}\left(\sin\phi_1 + \sin\phi_2\right) + G\frac{\Phi_0}{2\pi}\left(\dot{\phi}_1 + \dot{\phi}_2\right) + C\frac{\Phi_0}{2\pi}\left(\ddot{\phi}_1 + \ddot{\phi}_2\right)$$
$$+ \Delta I_{\rm c}\left(\sin\phi_1 - \sin\phi_2\right) + \Delta G\frac{\Phi_0}{2\pi}\left(\dot{\phi}_1 - \dot{\phi}_2\right) + \Delta C\frac{\Phi_0}{2\pi}\left(\ddot{\phi}_1 - \ddot{\phi}_2\right), \tag{34}$$

in which I_0 is the expression assuming all parameters are symmetric between the left and right arms, and ΔI is the expression that accounts for asymmetries in the SQUID parameters. No approximations have been made, and the expression is exact within the RCSJ model. Using the trigonometric identities,

$$\sin\phi_1 + \sin\phi_2 = 2\cos\left(\frac{\phi_1 - \phi_2}{2}\right)\sin\left(\frac{\phi_1 + \phi_2}{2}\right) \equiv 2\cos\phi_{\rm m}\sin\phi_{\rm p} \tag{35}$$

$$\sin\phi_1 - \sin\phi_2 = 2\cos\left(\frac{\phi_1 + \phi_2}{2}\right)\sin\left(\frac{\phi_1 - \phi_2}{2}\right) \equiv 2\cos\phi_{\rm p}\sin\phi_{\rm m}, \tag{36}$$

where $\phi_{\rm p,m} \equiv (\phi_1 \pm \phi_2)/2$ are symmetric and antisymmetric phases of the SQUID, the expression for the SQUID current becomes

$$I_0 = 2I_{\rm c}\cos\phi_{\rm m}\sin\phi_{\rm p} + 2G\frac{\Phi_0}{2\pi}\dot{\phi}_p + 2C\frac{\Phi_0}{2\pi}\ddot{\phi}_p \tag{37}$$

$$\Delta I = 2\Delta I_{\rm c}\cos\phi_{\rm p}\sin\phi_{\rm m} + 2\Delta G\frac{\Phi_0}{2\pi}\dot{\phi}_m + 2\Delta C\frac{\Phi_0}{2\pi}\ddot{\phi}_m. \tag{38}$$

The equation of motion for a symmetric SQUID (Eq. 37) is equivalent to Eq. 8 with the substitutions in Table 1. The last substitution in Table 1 follows from the assumption of zero-inductance

Josephson junction	**DC SQUID**
$G = 1/R$	$2G = 2/R$
C	$2C$
ϕ	$\phi_{\rm p}$
$I_{\rm c}$	$2I_{\rm c}\cos\phi_{\rm m} = 2I_{\rm c}\cos\left(\frac{\pi\Phi_{\rm ext}}{\Phi_0}\right)$

Table 1: *Corresponding paramters between a Josephson junction and its DC SQUID equivalent.*

and fluxoid quantization (Eq. 23) with $n = 0$. By construction we have restricted the range $\pi\Phi_{\rm ext}/\Phi_0 \in (-\pi/2, \pi/2)$, although this may be generalized by taking $|\cos(\pi\Phi_{\rm ext}/\Phi_0)|$. The resistance and capacitance substitutions follow from their parallel combination in the SQUID, again, in the absence of SQUID inductances. Defining $I_{\rm c,SQ} = 2I_{\rm c}|\cos(\pi\Phi_{\rm ext}/\Phi_0)|$, the current through the SQUID is

$$I = I_{\rm c,SQ}\sin\phi_{\rm p} \tag{39}$$

which is the first Josephson equation. The circulating current of the SQUID can similarly be related to $\sin\phi_{\rm m}$. It is interesting to note that the corrections to this ideal equivalence swaps the roles of $\phi_{\rm p}$ and $\phi_{\rm m}$. The correction dynamics are governed by the circulating current.

2.3 Superconducting qubits

In this section, we review the basic construction and operation of superconducting qubits. We will focus on "first-generation" qubits, including the charge, quantronium, persistent-current flux qubit, and phase qubits. We will also discuss briefly the "next-generation" qubits, including their evolution from the first-generation, their similarities, and their differences. Our goal here is to provide a high-level overview, including the Hamiltonian and the fundamentals of their operation. We refer the readers to the original proposals and experimental papers for more details.

In the following, we will define the charging energy in terms of the single-electron charging energy $E_{\rm C} \equiv e^2/2C$ [121]. This means that a superconducting Cooper pair has charging energy $4E_{\rm C}$. On the other hand, we will define the Josephson energy $E_{\rm J} \equiv I{\rm c}\Phi_0/2\pi$ in terms of the superconducting flux quantum $\Phi_0 = h/2e$. This follows a somewhat general convention, although it is certainly not a universal one.

2.3.1 Charge qubit

The charge qubit was among the first superconducting devices to demonstrate properties of quantum coherence, including evidence for quantum superposition of charge states [122, 123, 124, 125]. It was also the first superconducting circuit used to demonstrate coherent control and temporal oscillations [3].

The charge qubit is a Cooper pair box (CPB) (Fig. 3A), comprising a small superconducting island isolated by a Josephson junction and a capacitor to ground. The key feature of this island is that it is sufficiently small that the charging energy required to add a single Cooper pair to the island is much larger than the thermal energy at the milliKelvin temperatures of a dilution refrigerator,

$$4E_{\rm C} = 4\frac{e^2}{2C_\Sigma} \gg k_{\rm B}\Theta \tag{40}$$

where the capacitance $C_\Sigma = C_{\rm J} + C_{\rm g}$ is the total capacitance and generally must be less than 1 fF. The amount of charge on the island that is induced by the gate, expressed in units of extra Cooper pairs,

$$n_{\rm g} = \frac{C_{\rm g}V_{\rm g}}{2e} \tag{41}$$

is controlled by the voltage source $V_{\rm g}$. Although the Cooper pairs themselves are counted in discrete units, this reduced charge is continuous, because it is related to the polarization charge on the capacitor. Therefore, $n_{\rm g}$ is continuously tunable from n to $n+1$. The source of discrete island Cooper pairs is the junction itself via Josephson tunneling with Josephson energy $E_{\rm J}$. In the CPB, $E_{\rm C} \gg E_{\rm J}$ (or, at most, of order unity), and so the number of Cooper pairs on the island is a well-defined (localized) variable. The operator $\hat{n}$ will count the number of Cooper pairs that have tunneled on/off the island,

$$\hat{n}|n\rangle = n|n\rangle \tag{42}$$

and the classical (diabatic) states of the device are the charge states $|n\rangle$ and $|n+1\rangle$. The operator $\hat{n}$ is conjugate to the Josephson phase operator (the phase difference across a junction),

$$\hat{\phi}|\phi\rangle = \phi|\phi\rangle. \tag{43}$$

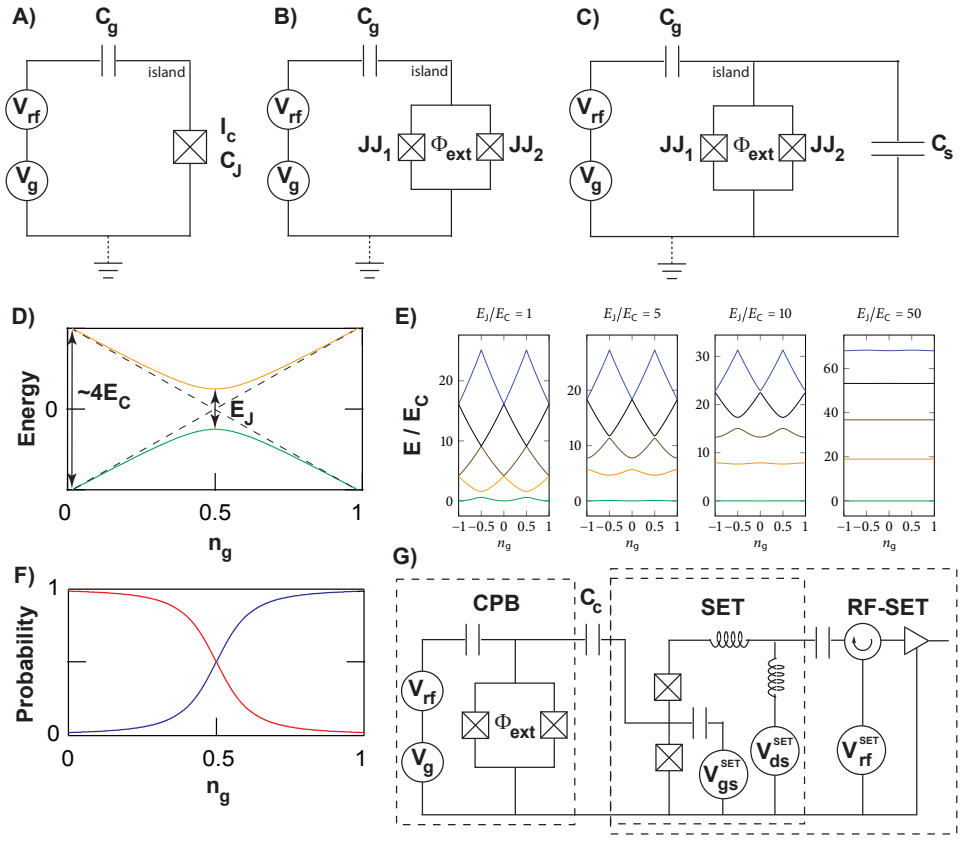

Fig. 3: Cooper Pair Box (CPB) and its derivatives. A) *Circuit diagram of a single-junction CPB. The number of extra Cooper pairs on the island, $n_{\rm g}$, is controlled by the gate voltage $V_{\rm g}$. The charge $n_{\rm g}$ is continuous, not discrete units of $2e$, because it is related to the polarization charge on the capacitor $C_{\rm g}$. Tuning $n_{\rm g}$ changes the electrostatic energy of the CPB by changing the amount of charge on the island subject to the charging energy $E_{\rm c}$.* **B)** *Split-junction CPB. A flux $\Phi_{\rm ext}$ tunes the critical current of the effective junction formed by the SQUID, thereby tuning the Josephson energy $E_{\rm J}$.* **C)** *Transmon: a capacitively shunted CPB. Adding a large parallel capacitor to the CPB flattens the energy levels and makes the CPB much less sensitive to charge fluctuations. The transmon may be realized as either a single junction (not shown) or a split-junction.* **D)** *Energy level diagram for the CPB within the two-level system approximation. The dashed lines are the classical charge states (diabatic energy levels). The solid lines are the eigenenergy levels that include Josephson coupling, which opens an avoided crossing of value $E_{\rm J}$. At the avoided crossing, the CPB is first-order insensitive to fluctuations in the charge.* **E)** *Multi-level energy diagram for the full CPB Hamiltonian assuming different values for the ratio $E_{\rm J}/E_{\rm C}$. As the ratio increases, the energy levels flatten and become less sensitive to charge. $E_{\rm J}/E_{\rm C} = 1$ is the CPB limit; $E_{\rm J}/E_{\rm C} = 50$ is the transmon limit.* **F)** *Probability of measuring 0 (red) or 1 (blue) Cooper pairs on the island using an SET readout. The probability is estimated by repeatedly measuring an identically prepared CPB. At the avoided crossing, the readout cannot distinguish the two classical states since $\langle n_{\rm g} \rangle = 0.5$.* **G)** *Simplified schematic for the readout of the CPB using a single-electron transistor (SET) operated in the DC transport regime, or as a resonant circuit (RF-SET). The CPB state modifies the SET island charge through the coupling capacitor $C_{\rm c}$, which modifies the DC current flowing through the island (drain-source current). Alternatively , it modifies the impedance seen by the RF source.*

See Appendix A for a brief review of their properties.

The CPB Hamiltonian is a sum of two terms,

$$\hat{\mathcal{H}}_{\rm CPB} = 4E_{\rm C}(\hat{n} - n_{\rm g})^2 + E_{\rm J}(1 - \cos\hat{\phi}) \tag{44}$$

$$\rightarrow 4E_{\rm C}(\hat{n} - n_{\rm g})^2 - E_{\rm J}\cos\hat{\phi} \tag{45}$$

where the second line removes the static offset energy $E_{\rm J}$, but is otherwise equivalent to the first line. The first term is the electrostatic energy, which is related to the island charge. The electrostatic energy levels plotted versus $n_{\rm g}$ are parabolae, each associated with a discrete Cooper pair state $n = 0, 1, \ldots$ with minima that occurs at the respective value n (see Fig. 3E, $E_{\rm J}/E_{\rm C} = 1$). Tuning the gate voltage will increase the energy parabolically away from these minima. When the island charage reaches $n + 1/2$, the energy levels of the parabolae associated with charge states $|n\rangle$ and $|n+1\rangle$ are degenerate. Josephson tunneling between n and $n+1$ Cooper pairs on the island mixes these states and opens an avoided crossing with a strength dictated by the Josephson energy. This is the second term of the Hamiltonian, and it is the junction energy written in the phase basis. The mixing of charge states is elucidated by writing the Hamiltonian in the charge basis (see Appendix A),

$$\hat{\mathcal{H}}_{\rm CPB} = \sum_n \left[4E_{\rm C}(\hat{n} - n_{\rm g})^2 |n\rangle\langle n| - \frac{E_{\rm J}}{2}\left(|n\rangle\langle n+1| + |n+1\rangle\langle n|\right)\right]. \tag{46}$$

Alternatively, in the phase basis, the Hamiltonian is

$$\hat{\mathcal{H}}_{\rm CPB} = 4E_{\rm C}\left(\frac{1}{i}\frac{\partial}{\partial\hat{\phi}} - n_{\rm g}\right)^2 - E_{\rm J}\cos\hat{\phi} \tag{47}$$

The choice of representation is one of convenience, depending on what is being calculated. For example, the formal solutions to the Schrödinger equation in the phase basis are written in terms of Mathieu functions [197].

The CPB can have both a tunable gate charge $n_{\rm g}$ and a tunable splitting $E_{\rm J}$ at the avoided crossing by replacing the junction in Fig. 3A with a SQUID as shown in Fig. 3B. In this case, the Josephson energy is a function of the external magnetic field applied to the SQUID loop,

$$\hat{\mathcal{H}}_{\rm CPB,SQ} = 4E_{\rm C}(\hat{n} - n_{\rm g})^2 - E_{\rm J}(\Phi_{\rm ext})\cos\hat{\phi} \tag{48}$$

$$E_{\rm J}(\Phi_{\rm ext}) = E_{\rm J,max}\left|\cos\left(\frac{\pi\Phi_{\rm ext}}{\Phi_0}\right)\right| \tag{49}$$

where we have assumed a symmetric SQUID and $E_{\rm J,max} = E_{\rm J1} + E_{\rm J2}$.

The CPB can be written within a two-level system approximation by expanding the Hamiltonian about the charge degeneracy point at $n_{\rm g} = 1/2$, taking the charge states to be $|0\rangle$ and $|1\rangle$,

$$\hat{\mathcal{H}}^{\rm TLS}_{\rm CPB} = -\frac{1}{2}\left[4E_{\rm C}(1 - 2n_{\rm g})\hat{\sigma}_{\rm x} + E_{\rm J}(\Phi_{\rm ext})\hat{\sigma}_{\rm z}\right] \tag{50}$$

$$\equiv -\frac{\hbar}{2}\left[\varepsilon\hat{\sigma}_{\rm x} + \Delta\hat{\sigma}_{\rm z}\right] \tag{51}$$

where $\hat{\sigma}_{\rm x,z}$ are the Pauli spin matrices (see Fig. 3D), and we have made the association,

$$\hbar\varepsilon = 4E_{\rm C}(1 - 2n_{\rm g}) \tag{52}$$

$$\hbar\Delta = E_{\rm J}(\Phi_{\rm ext}) \tag{53}$$

Although this Hamiltonian is often written with $\hat{\sigma}_{\rm x}$ and $\hat{\sigma}_{\rm z}$ switched, we have chosen this representation so that this Hamiltonian is diagonalized (qubit along z) when biased at $n_{\rm g} = 1/2$. This conforms with our usage in Section 3. At $n_{\rm g} = 1/2$, the eigenstsates are $\sigma_{\rm z}$ and the energy levels are first-order insensitive to charge noise. Away from $n_{\rm g} = 1/2$, the eigenstates are $\sigma_{\rm x}$-like, and the energy levels become sensitive to charge fluctuations due to there non-zero slope. The CPB is read out using a single-electron transistor (SET) operated as a sensitive charge electrometer (Fig. 3G). The SET is a superconducting island isolated by two junctions, similar to the CPB. The "drain" and "source" of the SET are the junction electrodes that connect to the island. When the SET is biased near a charge degeneracy point ($n_{\rm g} = n+1/2$), current can flow from drain to source with a value that depends strongly on the gate-source voltage $V_{\rm gs}$. The CPB island is coupled capacitively to the island and modifies the SET gate charge depending on the state of the CPB. The voltage $V_{\rm gs}$ sets a bias point such that there is a maximal change in drain-source current between the CPB states $|0\rangle$ and $|1\rangle$. The probability of detecting states $|0\rangle$ and $|1\rangle$ as a function of the CPB $n_{\rm g}$ is illustrated in Fig. 3F. Note that at the CPB charge-degeneracy point ($n_{\rm g} = 1/2$), the SET cannot distinguish between $|0\rangle$ and $|1\rangle$, because their probabilities of detection are equally likely. This results from the fact that $|0\rangle$ and $|1\rangle$ are classical (diabatic) charges states that are mixed into an equal superposition state at the avoided crossing due to $E_{\rm J}$ coupling.

The DC-SET readout is generally dissipative, because the small junctions experience phase diffusion during the readout. Another approach is to use a resonant circuit that involves the SET biased solidly in its superconducting state. In this RF-SET approach [85], an RF pulse near resonance with this circuit is applied to the SET and is reflected back through a circulator to an amplifier (see Fig. 3G). The CPB state modifies the SET impedance which, in turn, modifies the reflected phase of the RF signal sent to the SET. The RF-SET is a much faster approach to readout, and it is less dissipative than its DC counterpart.

2.3.2 Quantronium

An early design modification to the CPB was the quantronium [4] qubit (Fig.4A). Quantronium was the first qubit to demonstrate the use of the charge degeneracy point operation to mitigate low-frequency fluctuation and thereby extend dephasing times. To measure the state of the qubit while remaining at the charge degeneracy point, a large junction was added in parallel to the CPB forming a loop. Flux through this loop controlled an additional degree of freedom and, thereby, a new noise channel. However, the energy along this flux dimension also had a degeneracy point. The qubit was operated at this "double" charge-flux degeneracy point, and was thereby made insensitive to both charge and flux noise to first order. Dephasing times of around 500 ns were enabled by this approach, a 10x-100x improvement at the time [4].

Readout was performed by shifting the qubit away from the flux degeneracy point. In doing so, the qubit state was mapped onto circulating currents around the CPB-JJ loop. In the original work [4], a switching-current approach was used. A current pulse was applied to the loop close to the switching current of the large JJ. The exact value of the switching current was modified by state of the CPB; by choosing an appropriate current bias, the junction would switch for one state and not the other. By monitoring the presence or absence of a voltage pulse over several trials, one estimates the state occupation probability. The parallel capacitor in this approach acts as a "mass" to reduce phase fluctuations of the large junction and, thereby, narrow the switching-current distribution.

An alternative approach that does not rely on switching is to view the Josephson induc-

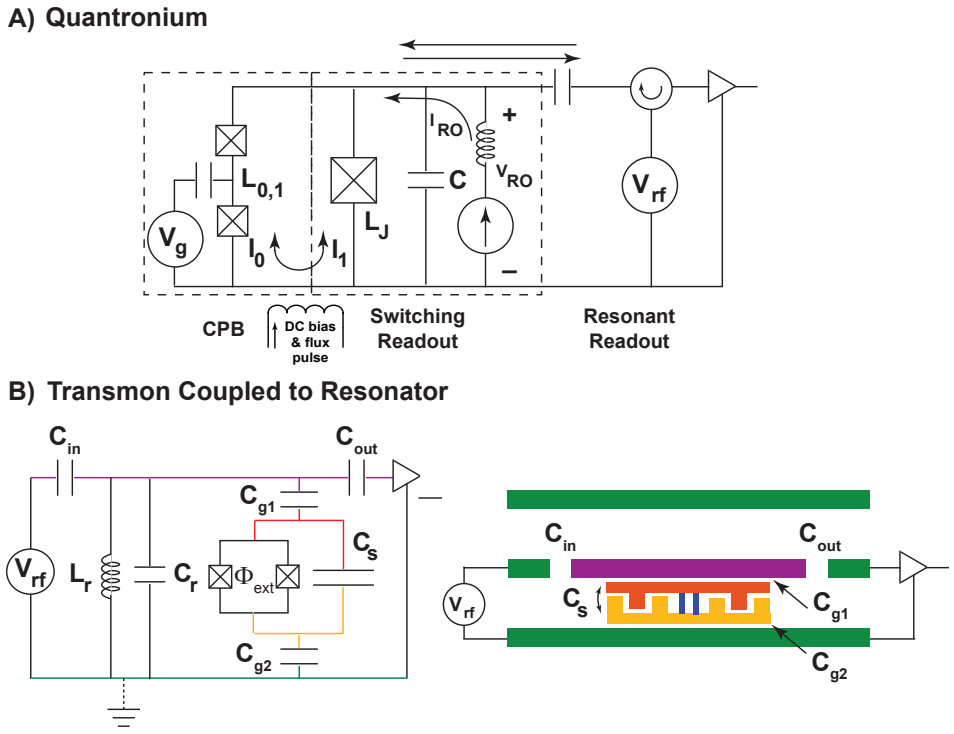

Fig. 4: Quantronium and transmon qubit readout A) *Quantonium circuit is a CPB with a large junction in parallel. The circuit has two degeneracy points: one charge and one flux due to the CPB-JJ loop. To read out quantronium, a flux pulse shifts the qubit away from the flux degeneracy point, and the qubit state corresponds to circulating currents clockwise or counter clockwise. The switching-current readout method sends a current pulse* $I_{\rm RO}$ *through the CPB-JJ circuit and monitors the voltage* $V_{\rm RO}$*from a state-dependent switching event. In the RF version of the readout, the large JJ and a parallel capacitor resonate at a frequency far detuned from the qubit (*e.g., *1.5 GHz in Ref. [181]), and the state-dependent CPB inductance shifts this resonant frequency. An RF pulse near resonance probes the circuit, and its reflection carries a state-dependent amplitude and phase. Figure adapted from Refs. [4, 181]* **B)** *Transmon coupled to a coplanar transmission line resonator, modeled in the circuit schematic as a lumped element resonator. In the dispersive limit,* $g \ll \Delta$*, an RF pulse probes the transmon-state-dependent resonance frequency and phase of the coplanar resonator. Adapted from Ref. [9].*

tance $L_{\rm J}$ of the large JJ and its parallel capacitance C as a lumped-element resonant circuit with resonance frequency $\nu \approx 1.5$ GHz. The CPB itself has a state-dependent inductance which serves to modify the resonance frequency. By probing this resonator with an RF pulse and monitoring the frequency and/or phase of the reflected pulse, the qubit state is determined. The advantage here is three fold. First, the junctions need not switch and so there is much less dissipation using this approach. Second, the readout can be implemented much more quickly, because one does not need to wait for quasiparticle relaxation to repeat the experiment. And, third, the resonator itself is nonlinear and, at higher amplitudes, can be operated as a Josephson bifurcation amplifier (nonlinear readout) [86, 88, 89]. One potential disadvantage is that the qubit dephasing may occur due to photon number fluctuations in the resonator.

2.3.3 Transmon

The transmon and its readout will be covered in detail within another lecture in this series. Here, we provide a brief overview for completeness and to make the historical connection with the CPB.

The CPB is sensitive to $1/f$ charge noise fluctuations due to its energy dispersion. Even with the first-order insensitivity afforded at the degeneracy point, charge offsets due to nearby charge fluctuators severely impact the operation of the CPB. A solution to remedy this problem was offered in Ref. [9], which introduced the transmon. The transmon is essentially a CPB with a large capacitor in parallel (Fig. 3C). The capacitor acts to flatten the energy level dispersion by increasing the $E_{\rm J}/E_{\rm C}$ ratio (Fig. 3E). Typical values for transmons are $E_{\rm J}/E_{\rm C} = 50 \ldots 80$. As a consequence, as compared to the conventional CPB, the transmon is much less sensitive to low-frequency charge noise and therefore has dramatically improved dephasing times. Aside from the different regime of parameters, the transmon Hamiltonian and its solutions have the same form as the CPB.

Because the transmon has relatively small charge dispersion, there is a negligibly small charge signature of the transmon states and a different approach to readout is required. By strongly coupling the qubit transversally to a resonator (either lumped element resonator, 2D distributed waveguide resonator, or a 3D cavity), one realizes essentially a Jaynes-Cummings Hamiltonian (see Fig. 4B),

$$\hat{\mathcal{H}}_{\rm JC} = 4E_{\rm C}(\hat{n} - n_{\rm g})^2 - E_{\rm J}(\Phi_{\rm ext})\cos\hat{\phi} + \hbar\omega_{\rm r}\hat{a}^\dagger\hat{a} + \hbar g\hat{n}(\hat{a} + \hat{a}^\dagger) \tag{54}$$

where $\hat{a}^\dagger$ and $\hat{a}$ are creation and annihilation operators of the resonator field, the third term is the energy of the resonator field, the fourth term is the coupling between the transmon and the resonator, and global energy offsets have been dropped. The prefactor g is the coupling strength between the transmon and the resonator, and $g = 2\beta e V^0_{\rm rms}$ for a coplanar waveguide, with $V^0_{\rm rms}$ the zero-point voltage of the cavity and β a voltage division ratio which is a function in terms of the capacitances in the circuit and acts to scale the coupling to the transmon. Within the two-level approximation for the transmon, the Hamiltonian is,

$$\hat{\mathcal{H}}^{\rm TLS}_{\rm JC} = \hbar\omega_{\rm r}\hat{a}^\dagger\hat{a} + \frac{\hbar\omega_{\rm q}}{2}\hat{\sigma}_{\rm z'} + \hbar g\hat{\sigma}_{\rm x'}(\hat{a} + \hat{a}^\dagger) \tag{55}$$

where the transmon portion of the Hamiltonian is written in its eigenbasis, as denoted by the prime notation on the $\hat{\sigma}_{\rm z',x'}$ operators. It has been demonstrated that superconducting circuits can operate within the strong-coupling regime $g \gg \gamma, \kappa$, where the coupling g is much larger than the decay rates of either the cavity, κ, or the transmon, γ.

In addition to enabling numerous beautiful cavity QED demonstrations with superconducting circuits, the Jaynes-Cummings-type Hamiltonian and its use of a strong, transverse coupling between the transmon and the resonator enables the readout of the transmon without the need for classical charge sensitivity. The readout is performed dispersively, by detuning the cavity frequency from the qubit frequency. This is a necessary operating condition in general, not just for readout, because the Purcell effect would otherwise enhance the decay rate of an atom (or qubit) resonantly coupled to a cavity field [10]. In the dispersive limit, the detuning $\Delta = \omega_{\rm q} - \omega_{\rm r}$ is larger than the coupling, $\sqrt{n}g \ll \Delta$. In this limit, the Hamiltonian can be expanded to second order in g/Δ [9] to yield the following dispersive, two-level system Hamiltonian,

$$\hat{\mathcal{H}}^{\rm TLS}_{\rm disp-JC} = \frac{\hbar(\omega_{\rm q}+\chi)}{2}\hat{\sigma}_{\rm z'} + \hbar(\omega_{\rm r} + \chi\hat{\sigma}_{\rm z'})\hat{a}^\dagger\hat{a}, \tag{56}$$

in which the original transverse coupling of the Jaynes-Cummings Hamiltonian is now manifest as a dispersive shift χ. The qubit frequency experiences a Lamb shift $\omega_{\rm q} + \chi$, and the resonator frequency experiences a transmon-state-dependent shift, $\omega_{\rm r} \pm \chi$, where $\chi = g^2/\Delta$ and we have ignored the shifts due to states outside the two-level manifold [9].

The primary trade-off made with the transmon is that the anharmonicity

$$\alpha = \frac{E_{12}}{E_{01}} - 1 \tag{57}$$

of the CPB has been dramatically reduced. In effect, by adding the capacitor, the CPB has come much closer to a harmonic oscillator ($\alpha = 0$). For the transmon, anharmonicities around $\alpha = -0.1$ are typical. This can be compared with the CPB anharmonicity typically around $\alpha = 5$. This is not catastrophic, obviously, given the success of the transmon, but it does carry implications for quantum control. To limit excitations to the two-level system manifold (and not simultaneously excite higher states), one must generally apply longer pulses. Longer temporal pulses correspond to narrower spectral width in the frequency domain; by lengthening the pulses, one can avoid off-resonantly driving nearby transitions. Another approach is to compensate the unwanted, off-resonance transitions with control methods [126].

2.3.4 Persistent-current flux qubit

The persistent-current flux qubit is a superconducting loop interrupted by three (Fig. 5A) or four (not shown) Josephson junctions. One the the junctions is smaller in area by a factor α, with a typical value $\alpha = 0.75$ for the three-junction qubit and $\alpha = 0.5$ for the four-junction qubit. In this section, we will focus primarily on the three-junction version of this qubit. The four junction qubit has the certain advantages due to its symmetry when fabricated using double-angle shadow evaporation [5, 6], but otherwise it operates similarly to the three-junction qubit.

The small junction acts as a flux-shuttle value that lets a fluxoid in and out of the loop. The larger junctions serve to add loop inductance. The loop itself has negligible inductance. We will assume symmetric large junctions with $E_{\rm J2} = E_{\rm J3} \equiv E_{\rm J}$ and junction capacitances $C_2 = C_3 \equiv C$. The small junction has capacitance αC and Josephson energy $\alpha E_{\rm J}$. The gate capacitances are used to model the effect of offset charges in the environment. We will assume symmetric gate capacitances $C_{\rm gA} = C_{\rm gB} \equiv C_{\rm g}$, with a value $C_{\rm g} = \gamma C$.

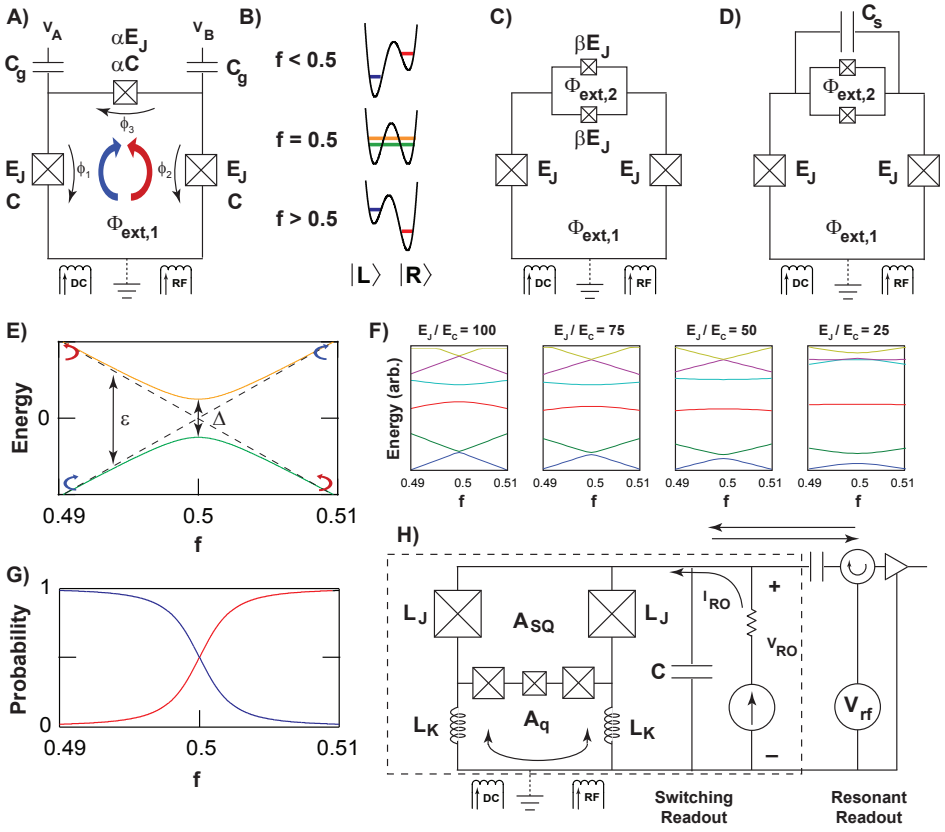

Fig. 5: Flux qubit and its derivatives A) *Three-junction flux qubit [128, 127]. One junction is smaller by a factor* α*. An external magnetic flux* $\Phi_{\mathrm{ext},1}$ *threads the loop, parameterized in reduced units,* $f = \Phi_{\mathrm{ext},1}/\Phi_0$*.* **B)** *Near* $f = 0.5$*, the qubit potential assumes a double well. For* $f < 0.5$*, the left well has a lower energy (clockwise current); for* $f > 0.5$*, the right well has a lower energy (counter-clockwise current). At* $f = 0.5$*, the diabatic state energies are degenerate. Tunnel coupling mixes the states, forming superpositions of the circulating currents and the qubit has no net magnetic polarization.* **C)** *Flux qubit with tunable* Δ *by splitting the small junction into a SQUID with its own flux bias* $\Phi_{\mathrm{ext},2}$*. The SQUID junctions are smaller by a factor* β*.* **D)** *Capacitively-shunted flux qubit. Decreasing the* $E_{\mathrm{J}}/E_{\mathrm{C}}$ *ratio flattens the energy bands but increases sensitivity to charge noise. A parallel capacitor across the small junction mitigates this noise [182, 129].* **E)** *Two-level system energy-level diagram. Flux tunes energy* ε *of the diabatic states (dashed lines). At* $f = 0.5$*, these states mix and open an avoided crossing* Δ*. At this point, the flux qubit is first-order insensitive to flux fluctuations.* **F)** *Multi-level energy level diagram for several values of the* $E_{\mathrm{J}}/E_{\mathrm{C}}$ *ratio. Larger capacitance (D) decreases this ratio, flattening the energy bands.* $E_{\mathrm{J}}/E_{\mathrm{C}} = 75$ *is a typical flux-qubit value.* $E_{\mathrm{J}}/E_{\mathrm{C}} < 50$ *is a capacitively shunted flux qubit.* **G)** *Probability of measuring clockwise (blue) or counterclockwise (red) circulating currents using a SQUID readout. At the avoided crossing, the readout cannot distinguish the two classical states since the net magnetic polarization is zero.* **H)** *Simplified schematic for the flux qubit readout using a DC SQUID magnetometer. The qubit is mutually coupled to the SQUID through either its geometric inductance (not shown) and/or the kinetic inductance* L_{K} *of a shared line. The qubit adds/subtracts a state-dependent flux to/from the SQUID, modifying its switching current. Ramping a current between these state-dependent values results in a switching event for one state, but not the other. Alternatively, the SQUID inductance in parallel with the capacitor* C *forms a resonant circuit. RF reflectometry techniques can be used to probe the state-dependent frequency and phase of this resonator.*

The flux qubit has a potential energy U equivalent to the total Josephson energy of the three junctions,

$$U = \sum_i E_{\mathrm{J}i}(1 - \cos\phi_i). \tag{58}$$

The fluxoid quantization condition sets $\phi_1 - \phi_2 + \phi_3 = -2\pi f$, where $f \equiv \Phi_{\mathrm{ext}}/\Phi_0$ is the applied external magnetic flux Φ_{ext} normalized by the superconducting flux quantum Φ_0. Eliminating ϕ_3 yields,

$$\begin{aligned} U &= E_{\mathrm{J}}\left[2 + \alpha - \cos\phi_1 - \cos\phi_2 - \alpha\cos(2\pi f + \phi_1 - \phi_2)\right] &(59)\\ &= E_{\mathrm{J}}\left[2 + \alpha - 2\cos\phi_{\mathrm{p}}\cos\phi_{\mathrm{m}} - \alpha\cos(2\pi f + 2\phi_{\mathrm{m}})\right] &(60)\end{aligned}$$

where we have used the sum and difference phases $\phi_{\mathrm{p,m}} = (\phi_1 \pm \phi_2)/2$. The two-dimensional potential U forms an "egg carton" as a function of ϕ_{p} and ϕ_{m} with the unit cells periodic in 2π [128].

The electrostatic energy ($CV^2/2$) stored in the five capacitors in Fig. 5A is (see Ref. [128])

$$\begin{aligned} T &= \frac{1}{2}\left(\frac{\phi_0}{2\pi}\right)^2 \dot{\vec{\phi}}^{\mathrm{T}} \cdot \mathbf{C} \cdot \dot{\vec{\phi}} - \frac{1}{2}\vec{V}_{\mathrm{g}}^{\mathrm{T}} \cdot \mathbf{C}_{\mathrm{g}} \cdot \vec{V}_{\mathrm{g}} &(61)\\ &= \frac{1}{2}\vec{Q}_{\mathrm{tot}}^{\mathrm{T}} \cdot \mathbf{C}^{-1} \cdot \vec{Q}_{\mathrm{tot}} &(62)\end{aligned}$$

where $\dot{\vec{\phi}} = [\dot{\phi}_1, \dot{\phi}_1]^{\mathrm{T}}$, the gate voltage is $\vec{V}_{\mathrm{g}} = [V_{\mathrm{A}}, V_{\mathrm{B}}]^{\mathrm{T}}$, the total island charge is $\vec{Q}_{\mathrm{tot}} = \mathbf{C} \cdot (\Phi_0/2\pi)\dot{\vec{\phi}} \equiv \mathbf{C} \cdot \mathbf{V}$ in terms of the junction voltages $\mathbf{V}$, and the capacitance matrices are,

$$\mathbf{C} = C\begin{pmatrix} 1+\alpha+\gamma & -\alpha \\ -\alpha & 1+\alpha+\gamma \end{pmatrix} \qquad \mathbf{C}_{\mathrm{g}} = \gamma C\begin{pmatrix} 1 & 0 \\ 0 & 1 \end{pmatrix}. \tag{63}$$

The transition from classical Josephson and electrostatic energies to the quantum Hamiltonian follows the correspondance principle and is presented in detail in Ref. [128]. Here, we present the net results only.

In the phase basis, the three-junction flux-qubit Hamiltonian is

$$\begin{aligned} \hat{\mathcal{H}}_{\mathrm{FQB}} = 4E_{\mathrm{C}}\left[\frac{1}{2}\frac{1}{(1+\gamma)}\left(\frac{1}{i}\frac{\partial}{\partial\hat{\phi}_{\mathrm{p}}}\right)^2 + \frac{1}{2}\frac{1}{(1+2\alpha+\gamma)}\left(\frac{1}{i}\frac{\partial}{\partial\hat{\phi}_{\mathrm{m}}}\right)^2\right] + \ldots \\ - E_{\mathrm{J}}\left[2\cos\hat{\phi}_{\mathrm{p}}\cos\hat{\phi}_{\mathrm{m}} + \alpha\cos(2\pi f + 2\hat{\phi}_{\mathrm{m}})\right], \end{aligned} \tag{64}$$

where we have dropped the energy offset $(2+\alpha)E_{\mathrm{J}}$. Note that the kinetic energy term has the form $\hat{P}_{\mathrm{p,m}}^2/2M_{\mathrm{p,m}}$ for momenta $\hat{P}_{\mathrm{p,m}} = -i\partial/\partial\hat{\phi}_{\mathrm{p,m}}$ and masses $M_{\mathrm{p,m}}$. Writing the kinetic term in the charge basis, the Hamiltonian becomes:

$$\begin{aligned} \hat{\mathcal{H}}_{\mathrm{FQB}} = 4E_{\mathrm{C}}\left[\frac{1}{2}\frac{1}{(1+\gamma)}\hat{n}_{\mathrm{p}}^2 + \frac{1}{2}\frac{1}{(1+2\alpha+\gamma)}\hat{n}_{\mathrm{m}}^2\right] + \ldots \\ - E_{\mathrm{J}}\left[2\cos\hat{\phi}_{\mathrm{p}}\cos\hat{\phi}_{\mathrm{m}} + \alpha\cos(2\pi f + 2\hat{\phi}_{\mathrm{m}})\right], \end{aligned} \tag{65}$$

where $\hat{n}_{\rm p,m} = \hat{n}_1 \pm \hat{n}_2$. Or, equivalently, in the mixed basis and in terms of the junction / island numbering,

$$\hat{\mathcal{H}}_{\rm FQB} = 4E_{\rm C}\left[\frac{1+\alpha+\gamma}{(1+\gamma)(1+2\alpha+\gamma)}(\hat{n}_1^2+\hat{n}_2^2) + \frac{2\alpha}{(1+\gamma)(1+2\alpha+\gamma)}\hat{n}_1\hat{n}_2\right] + \ldots \\ - E_{\rm J}\left[\cos\hat{\phi}_1 + \cos\hat{\phi}_2 + \alpha\cos(2\pi f + \hat{\phi}_1 - \hat{\phi}_2)\right]. \quad (66)$$

In either representation ($\hat{\phi}_{1,2}$ or $\hat{\phi}_{\rm p,m}$), the potential term can be converted to the charge representation using the relations in Appendix A.

When the applied flux is close to half a flux quantum, $f \approx 0.5$, the potential (within a unit cell) assumes a two-dimensional, double-well profile. A slice of this double well along the $\phi_{\rm m}$ direction is shown in Fig. 5B. The states in each well corresponds to a circulating persistent currents, clockwise or counterclockwise, around the loop with magnitude $I_{\rm p}$. As illustrated in Fig. 5, $f < 0.5$ tilts the left well (clockwise circulating current) to lower energy, whereas $f > 0.5$ tilts the right well (counterclockwise circulating current) to lower energy.

The two-level system model comprises the lowest-energy circultating current state in each well. These are the classical (diabatic) states (dashed lines, Fig. 5E), and they have energy,

$$\pm\frac{\hbar\varepsilon}{2} = \pm I_{\rm p}\Phi_0(f-1/2) \quad (67)$$

Note that $\delta f \equiv f - 1/2$ is sometimes used (*e.g.,* see Sections 3 and 4) to reference the flux to the degeneracy point at $f = 1/2$. At $f = 0.5$, the lowest-energy quantized states of the wells are degenerate. Quantum tunneling through the double-well barrier (Fig. 5B) hybridizes the classical (diabatic) states into superpositions of circulating currents, opening an avoided crossing of strength Δ (Fig. 5E). The value of Δ is generally found by diagonalizing the Hamiltonian, but it can be estimated using the WKB approximation to be

$$\hbar\Delta_{\rm WKB} \approx 1.3\sqrt{E_{\rm J}E_{\rm C}}e^{-0.64\sqrt{E_{\rm J}/E_{\rm C}}}. \quad (68)$$

Since $E_{\rm J} \propto A_{\rm J}$ and $E_{\rm C} \propto 1/A_{\rm J}$, where $A_{\rm J}$ is the junction area, Δ scales exponentially with the $A_{\rm J}$ and is thus highly sensitive to fabrication variations in the junction size.

The two-level system Hamiltonian for the flux qubit is,

$$\hat{\mathcal{H}}_{\rm FQB}^{\rm TLS} = -\frac{1}{2}\left[2I_{\rm p}\Phi_0(f-1/2)\hat{\sigma}_{\rm x} + \hbar\Delta\hat{\sigma}_{\rm z}\right] \quad (69)$$

$$\equiv -\frac{\hbar}{2}\left[\varepsilon\hat{\sigma}_{\rm x} + \Delta\hat{\sigma}_{\rm z}\right] \quad (70)$$

where $\hat{\sigma}_{\rm x,z}$ are the Pauli spin matrices (see Fig. 3D).

By splitting the small junction into a SQUID loop with two junctions having a Josephson energy $\beta E_{\rm J}$, one can tune Δ using a second external flux $\Phi_{\rm ext,2}$ (Fig. 5B). The Hamiltonians in Eqs. 64, 65, 66 are modified by making the following substitutions [128]

$$\alpha \rightarrow 2\beta \quad (71)$$

$$\alpha\cos(2\pi f + 2\hat{\phi}_{\rm m}) \rightarrow 2\beta\cos(\pi f_a)\cos(2\pi f_b + 2\hat{\phi}_{\rm m}) \quad (72)$$

where $f_a \equiv f_2$ is the reduced flux $\Phi_{\rm ext,2}$, and $f_b \equiv f_1 + f_2/2$ with $f_1 \equiv f$ in the single-loop qubit. Essentially, the flux f_2 tunes the value α via the factor $2\beta\cos(\pi f_a)$. However, because

one of the junctions in loop 2 is shared with loop 1, the flux bias f_b which tilts the double wells picks up a factor $f_2/2$.

As with the CPB and transmon, there is a capacitively shunted version of the flux qubit [182, 129]. Decreasing α decreases the $E_{\rm J}/E_{\rm C}$ ratio in the flux qubit and tends to flatten the energy bands, thereby decreasing the qubit's sensitivity to low-frequency flux noise. However, decreasing the $E_{\rm J}/E_{\rm C}$ ratio also makes the qubit more sensitive to charge noise. This can be mitigated by shunting the small junction with a capacitor.

The flux qubit is read out using either a switching-current method, resonant readout technique, or cavity-QED approach (similar to Fig. 4B). In Fig. 3H, we show a simplified schematic of the SQUID-based switching-current and resonant-readout approach. The DC SQUID is a sensitive magnetometer which can detect the small fluxes generated by the circulating currents. The qubit is mutually coupled to the SQUID by a combination of geometric inductance and, for galvanically connected devices, kinetic inductance. In the conventional switching current readout, a pulse is applied to the SQUID close to its switching current. The precise value of the switching current depends on the state of the qubit, and the pulse amplitude is chosen such that the SQUID switches for one state of the qubit and not the other (see Fig. 15C for an example). By repeating the experiment many times, an estimate for the state probability is generated (Fig. 5G). Alternatively, the SQUID inductance forms a resonator with a parallel capacitor, and the resonance frequency becomes qubit-state dependent through the inductance. RF reflectometry can then be used to probe the SQUID resonator frequency or phase to estimate the qubit state. Since the SQUID inductance is non-linear with its current, the SQUID resonator can be operated in both the linear (low current) or non-linear (large current) regimes.

An example of resonant readout of the flux qubit is shown in Fig. 6. The circuit schematic shows the flux qubit geometrically coupled to a DC SQUID. RF impedance networks are used to match the SQUID to the 50-Ohm lines used to probe the resonator. This has the practical effect of increasing the resonator Q value near the resonance frequency.

A DC current is used to generate an external flux $\Phi_{\rm ext}$ through the SQUID and the qubit. By properly designing the relative areas of the SQUID and qubit, the qubit can be biased at $f = 0.5$ for a value of SQUID switching current that is approximately midway between its maximum and minimum values. In Fig. 6B, the SQUID resonance frequency is plotted as a function of the current that applies the external flux to the qubit and SQUID. The resonance frequency modulates due to the SQUID critical current $I_{\rm c}(\Phi_{\rm ext})$ which, in turn, modulates the SQUID inductance $L_{\rm J}$. Note that the SQUID inductance is only a portion of the total resonator inductance, and the observed modulation is about 300 KHz on top of a resonance frequency $\nu_0 \approx 420$ MHz. A "qubit step" is clearly observed as a "jump" in the resonance frequency; this step corresponds to the qubit ground state changing the polarity of its circulating current as the qubit is stepped through the avoided crossing at $f = 0.5$ (see Fig. 5E).

Because the SQUID Josephson inductance is nonlinear in the SQUID current (the SQUID is an effective Josephson junction, see Section 2.2.5), the SQUID resonator is fundamentally anharmonic and may exhibit non-linear behavior. At large amplitudes, the resonator bifurcates, having multiple solutions (two stable solutions and one unstable solution) over a range of frequencies. The stable solutions are accessed preferentially depending on the initial state of the resonator. For example, as shown in Fig. 6C, sweeping the RF probe signal from low to high frequency (red arrows) accesses the lower-amplitude branch of the resonance up to the bifurcation point, after which the resonator state jumps to the higher-amplitude branch. In turn, starting from the high-frequency side and sweeping to lower frequencies (yellow arrows), the resonator state remains along the high-amplitude branch until the resonance peak is reached, after which

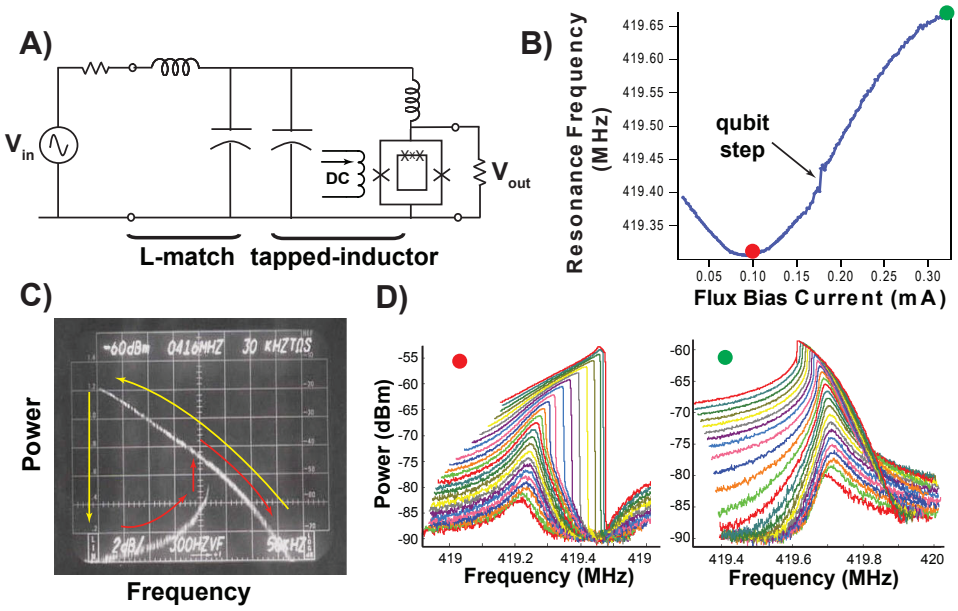

Fig. 6: Resonant readout of a flux qubit [87, 91] A) *Circuit schematic of the flux qubit and its SQUID. The SQUID is isolated from the 50-Ohm environment using an L-match and tapped-inductor impedance-matching network. The SQUID is shunted by a capacitor (not shown) and has a plasma frequency around 420 MHz. RF near the resonance frequency is applied from the left side, and measured at the load on the right side of the schematic in a through configuration.* **B)** *SQUID resonance frequency as a function of the flux applied to the qubit and SQUID. The SQUID critical current is modulated and, simultaneously, the qubit is biased. At a flux bias current around 0.18 mA, the resonance frequency makes an abrupt jump; this step corresponds to the qubit ground state changing the polarity of its circulating current.* **C)** *A strongly driven resonator will bifurcate. This picture is taken on an old oscilloscope that allows us to manually sweep from low- to high frequencies (path shown in red) and then from high- to low frequencies (path shown in yellow) while storing the trace on the screen. The strong asymmetry is indicative of a non-linear resonator.* **D)** *RF transmission as a function of frequency for several values of driving amplitude. As the amplitude increases, the resonance peak becomes asymmetric due to the SQUID nonlinearity. The resonance peak shifts to higher or lower frequency depending on the sign of the leading-order non-linear terms that govern the SQUID dynamics.*

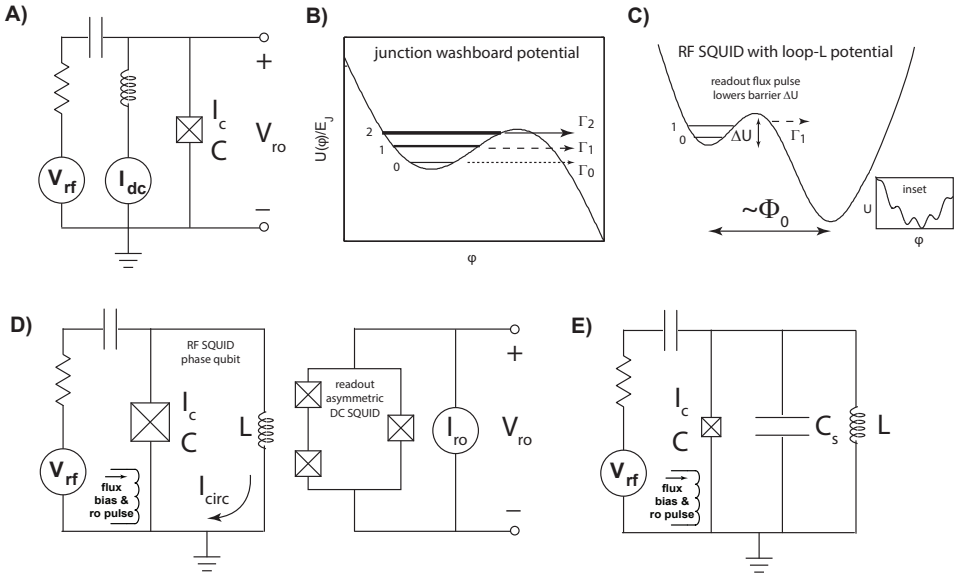

Fig. 7: Phase qubit and its derivatives A) *and* **B)***Single Josephson junction biased near its critical current is a phase qubit. The junction is biased such that the wells of the washboard potential have a few quantized states. Leakage rates to the running mode satisfy* $\Gamma_2 \gg \Gamma_1 \gg \Gamma_0$*. Driving the* ω_{12} *transition constitutes readout, which creates a voltage if the qubit were in state 1 due to tunneling from* $|2\rangle$ *to the running state.* **C** *and* **D)** *Flux-biased phase qubit realized in an RF SQUID geometry. The junction is placed in a loop with geometrical inductance* L*, resulting in a parabolic cosine potential (inset of C). The qubit is flux-biased with a pulsed current, and it is manipulated via RF pulses. Readout is achieved via a fast flux pulse which transiently reduces the potential barrier* ΔU*. If the qubit is in state 1, it will rapidly tunnel to the adjacent well associated with a flux change of about one* Φ_0*. An asymmetric DC SQUID senses the presence or absence of this flux to perform readout.* **E)** *Capacitively shunted phase qubit. Conventional AlOx junction dielectrics tend to be lossy and prone to defect states. Reducing the junction size (while maintaining its* I_c*) and adding a parallel shunt capacitor moves the capacitive energy outside the junction, improving qubit coherence times to the extent one can fabricate a high-Q capacitor.*

it jumps down to the single-valued low-amplitude state. Biasing a readout circuit near a bifurcation point therefore has the potential to increase signal-to-noise ratio (SNR) [88, 91, 92]. The resonance bends to lower or higher frequencies depending on whether the SQUID is at a high or low value of its switching current (Fig. 6D). This can be traced to the sign of the leading-order non-linear terms that govern the SQUID dynamics as discussed in [91]. Intuitively, bending to lower frequencies indicates an inductance that increases in value with increased current, whereas bending to higher frequencies indicates an inductance that decreases with current.

2.3.5 Phase qubit

The phase qubit is a current-biased Josephson junction (see Fig. 7A) [29]. When the junction is biased close to its critical current, the washboard potential (Fig. 7B) is sufficiently tilted that a potential well accommodates only a few quantized states. In this limit, the local potential well is sufficiently anharmonic that the ω_{01} transition can be distiguished from the ω_{12} transition.

The leakage rates from the well to the running mode of the junction satisfy $\Gamma_0 \ll \Gamma_1 \ll \Gamma_2$, such that state $|0\rangle$ is metastable, state $|1\rangle$ is relatively long-lived, and state $|2\rangle$ tunnels rapidly. Qubit readout is performed by driving the transition ω_{12}. If the qubit were in state $|1\rangle$, it would quickly tunnel to the running mode upon being driven to state $|2\rangle$. In the running mode, there is a junction voltage; the presence of a voltage indicates the qubit was in state $|1\rangle$ whereas the absence of a voltage indicates state $|0\rangle$.

To better isolate the junction from its environment and readout circuitry, the phase qubit junction was placed in a loop of inductance L, forming essentially an RF SQUID (Fig. 7C and D) [130]. The qubit potential energy U is the sum of the junction energy and the inductive energy due to the circulating current, (inset, Fig. 7C),

$$\begin{aligned} U &= E_{\rm J}\left[1-\cos\phi+\frac{1}{2}LI_{\rm circ}^2\right] \\ &= E_{\rm J}\left[1-\cos\phi+\frac{(\phi-\phi_{\rm ext})^2}{2\beta_{\rm L}}\right] \\ &= E_{\rm J}(1-\cos\phi)+E_{\rm L}(\phi-\phi_{\rm ext})^2 \end{aligned} \tag{73}$$

where $\phi_{\rm ext} \equiv 2\pi\Phi_{\rm ext}/\Phi_0$, $\beta_{\rm L} = L/L_{\rm J} = 2\pi LI_{\rm c}/\Phi_0$, $E_{\rm L} = (\Phi_0/2\pi)^2/2L$ is the inductive energy, and the fluxoid quantization condition was used.

The qubit loop is biased with an external flux $\Phi_{\rm ext}$, effectively biasing the junction via the loop circulating current. Tuning the external flux effectively shifts the cosine potential wells along the parabola. At particular biases, one can achieve the potential profile illustrated in Fig. 7C, comprising a shallow well isolated by a potential barrier of height ΔU from a relatively deep well. The shallow and deep wells are separated by approximately Φ_0. Typical parameters that allow for a transition $\omega_{01}/2\pi \approx 6$ GHz are $I_{\rm c} = 2$ μA, $C = 1$ pF, and $L = 700$ pH.

Qubit manipulation is through a combination of RF pulses capacitively coupled to the qubit and flux pulses that detune ω_{01} to realize Z rotations. The qubit state is readout is a two-step process. One first uses a fast flux pulse to transiently reduce the potential barrier ΔU (Fig. 7C). Doing so will exponentially increase the tunneling rate of state $|1\rangle$ to the right well, but leaves state $|0\rangle$ essentially metastable. A DC SQUID is then used in a switching-current type experiment (see sections 2.1.4 and 2.3.4) to look for a change in flux of approximately Φ_0 (a huge signal), indicating that a tunneling event occurred, and so the qubit was in state $|1\rangle$. An asymmetric DC SQUID (see section 2.2.4) is used, because it can have sensitivity $dI_{\rm c}/d\Phi_{\rm ext}$ to the external flux generated by the qubit without need for the SQUID having its own static flux bias. Finally, a flux pulse tilts the wells to reset the qubit state back into the left well.

The Hamiltonian for flux-biased phase qubit (an RF SQUID) is [183]

$$\hat{\mathcal{H}}_{\rm RFS} = 4E_{\rm C}(\hat{n}-n_0)^2 - E_{\rm J}\cos\hat{\phi} + E_{\rm L}(\hat{\phi}-\phi_{\rm ext})^2 \tag{74}$$

where n_0 represents fluctuating offset charges across the junction and shunt capacitances, and we have dropped the energy offset from the Josephson energy. Within the two-level system model, the phase qubit Hamiltonian is essentially a pseudospin with energy ω_{01} along $\sigma_{\rm z}$ with a transverse component related to changes in the circulating current $\delta I_{\rm circ}$. However, changing the circulating current will also change the frequency ω_{01}. As a result, the Hamiltonian is approximately [29, 131],

$$\hat{\mathcal{H}}_{\rm RFS}^{\rm TLS} = -\frac{1}{2}\left[\hbar\omega_{01}\hat{\sigma}_{\rm z} + \sqrt{\frac{\hbar}{2\omega_{01}C}}\delta I_{\rm circ}\,(\hat{\sigma}_{\rm x}+\chi\hat{\sigma}_{\rm z})\right] \tag{75}$$

where $\chi = \sqrt{\hbar\omega_{01}/3\Delta U} \approx 4$ for typical parameters.

In early experiments, the phase qubit suffered from loss and defects in the AlOx junction dielectric barrier [132]. An improvement was made by reducing the junction area (while maintaining I_c) and adding a large external shunt capacitor to compensate for the reduced junction capacitance (Fig. 7E) [133]. This design change placed the focus on developing a high-Q capacitor dielectric for the external capacitor as opposed to improving the Q of the junction barrier. Of the various barriers attempted, amorphous silicon dioxide (a-SiOx) has a relatively high loss tangent (Q^{-1}) of $\sim 5 \times 10^{-3}$ compared with $\sim 1 \times 10^{-4}$ for amorphous silicon nitride (a-SiNx) and yet another factor 10 or so better for hydrogenated amorphous silicon (a-Si:H) [134]. Efforts continue to improve these dielectrics, their surfaces and interfaces, and the development of new materials and fabrication techniques consistent with high-Q qubits.

2.3.6 RF SQUID qubit

The RF SQUID qubit was among the first flux qubits to demonstrate quantized energy levels and an avoided level crossing [24] (the other was the persistent-current flux qubit [25]). Although its Hamiltonian (Eq. 74) is the same as the flux-biased phase qubit, its mode of operation is most similar to the persistent-current flux qubit. The RF SQUID is nominally operated near a symmetric double-well potential configuration. The classical (diabatic) states of the RF SQUID are the circulating current states, and resonant tunneling through the double-well barrier will open an avoided crossing. Coherence in the RF SQUID qubit has not improved as dramatically as other qubits over the past several years, in part due to its strong sensitivity to flux noise.

2.3.7 Fluxonium and metastable RF-SQUID: inductively shunted qubits

Most qubits surveyed thus far have a capacitively shunted version which provided a performance improvement. There are two complementary examples of inductively shunted qubits: the fluxonium qubit [135], and the metastable RF-SQUID qubit [183]. Both are single junction loops shunted by a large inductance, have large anharmonicity, and can be viewed as inductively shunted RF-SQUIDs described by the RF-SQUID Hamiltonian (Eq. 74). They operate in very different parameter regimes.

The fluxonium qubit demonstrated in Ref. [135] has parameters: $E_J = 9.0$ GHz, $E_C = 2.5$ GHz, and $E_L = 0.52$ GHz. The shunt inductance is realized by a series array of junctions (43 junctions were used in Ref. [135]), each with an area about an order of magnitude larger than the small, single junction. The small, single junction acts as the flux-shuttle valve in and out of the loop. The series array of junctions both provides the shunt inductance and a DC short-circuit for offset charges on the islands connected to the small junction. The result is a qubit that is relatively immune to such charge noise. Each junction of the inductor array itself is designed to have parameters that suppress phase slips, that is, acting as a parallel flux-shuttle path to the small junction. These phase slips are in fact related to residual offset charges throughout the array. The coherent interaction of these phase slips across all junctions has led to a beautiful demonstration of Aharonov-Chasher physics with this superconducting qubit [136].

The metastable flux qubit, as designed in Ref. [183], has parameters: $E_J = 120$ GHz, $E_C = 6$ GHz, and $E_L = 60$ GHz. The large shunt inductance is realized via the kinetic inductance of a 5-nm thick niobium nitride (NbN) nanowire of the type used in single-photon detectors. A key feature of the nanowire is that it is compact, exhibits extremely large kinetic inductance, and yet has an extremely low shunt capacitance. For example, a 10×10 μm^2 me-

ander of 100-nm wide wire has an inductance $L \sim 500$ nH and yet only 0.4 fF of capacitance (based on EM simulations) [183, 137]. The qubit is designed to have a very small tunnel coupling ($\Delta \sim 50$ kHz), which increases T_1 times by reducing the transverse coupling of the qubit states, making it metastable (*e.g.,* the qubit used in Ref. [38] had $\Delta \sim 10$ MHz and correspondingly $T_1 \rightarrow 1$ms away from the qubit degeneracy point). Although it remains to be tested, the quantum phase-slip rate through the nanowire, which acts to increase Δ and thereby decrease T_1, is expected to be much lower than for a series array of junctions. Since $\hbar\Delta \ll k_{\rm B}\Theta$ at degeneracy, the qubit must be operated far from the degeneracy point, $f \ll 0.5$ or $f \gg 0.5$. Although there is non-zero energy dispersion away from degeneracy, the large inductance serves to dramatically reduce the flux sensitivity $d\omega_{01}/df$, such that simulation suggests that $T_2 \sim 15$ μs (this "T_2" is actually a Gaussian decay time due to 1/f noise, see Section 3.3.2) is achievable with standard levels of 1/f flux noise. Qubit control is achieved by parametrically modulating Δ at frequency ω_{01} through a split-junction loop of the type discussed in Section 2.3.4. The large inductance suppresses the circulating current to a degree that a switching current readout is no longer feasible. Rather, both a dispersive-type readout or qubit-mediated coupling techniques [70] can be used to readout the metastable flux qubit.

3 Free- and driven evolution of two-level systems

Quantum gate operations in superconducting qubits (and most qubit modalities in general) are broadly realized by two categories of coherent evolution: free evolution and driven evolution. During these periods of evolution, unwanted environmental noise acts to decohere the qubit and increase the gate error rate. Characterizing the noise which couples to the qubit during these two periods is therefore an important first step towards either mitigating or eliminating these sources of decoherence.

In this section, we will review the Bloch sphere representation of a two-level system, and consider how parameter fluctuations (*i.e.,* noise) impacts qubit dynamics in the laboratory, qubit (eigenstate), and rotating frames. We will then present a general perturbative approach to analyzing noise based on the approach used by Ithier *et al.* [7]. This will allow us to make a connection between the decay functions measured in experiments and the noise power spectral density $S_\lambda(\omega)$. The analogy between free- and driven evolution when viewed on a Bloch sphere allows us to define analogous energy-relaxation times (T_1 and $T_{1\rho}$) and coherence times (T_2 and $T_{2\rho}$) respectively for these two categories of evolution. The characteristic times need not correspond to exponential decay functions, and this is the case for decay functions corresponding to low-frequency noise. Table 3 summarizes the results discussed in this section.

3.1 Representations of the qubit Hamiltonian

3.1.1 Laboratory frame

In general, noise physically couples to a qubit in the laboratory frame. The Hamiltonian of the a two-level system in the laboratory frame (Fig. 8A) is

$$\begin{aligned}\hat{\mathcal{H}} &= \frac{\hbar}{2}\left\{\left[\Delta + \delta\Delta(t)\right]\hat{\sigma}_z + \left[\varepsilon + \delta\varepsilon(t)\right]\hat{\sigma}_x + A_{\mathrm{rf}}\cos(\omega_{\mathrm{rf}}t + \varphi)\hat{\sigma}_x\right\} \\ &= \frac{\hbar}{2}\left[\Delta\hat{\sigma}_z + \varepsilon\hat{\sigma}_x + A_{\mathrm{rf}}\cos(\omega_{\mathrm{rf}}t + \varphi)\hat{\sigma}_x\right] + \left[\delta\Delta(t)\hat{\sigma}_z + \delta\varepsilon(t)\hat{\sigma}_x\right] \\ &\equiv \hat{\mathcal{H}}_0 + \hat{\mathcal{H}}_F\end{aligned} \tag{76}$$

where $\hat{\sigma}_z$ and $\hat{\sigma}_x$ are Pauli operators. ε and Δ are parameters that depend on the particular physical qubit modality, for example, the energies corresponding to the circulating currents and tunnel coupling of a flux qubit. The oscillating term represents the harmonic drive with amplitude A_{rf}, carrier frequency $\nu_{\mathrm{rf}} = \omega_{\mathrm{rf}}/2\pi$ and phase φ. Note that A_{rf} is generally shaped and of finite duration (*e.g.*, a Gaussian pulse) in order to implement a particular gate operation (*e.g.*, a $\pi/2$ pulse around X) or set to zero (free evolution). We consider $\delta\varepsilon(t)$ and $\delta\Delta(t)$ to be temporal fluctuations of the parameters ε and Δ. To avoid clutter, we will not continue to write explicitly the time dependence. To make the presentation clearer, we do not explicitly carry through fluctuations δA_{rf} of the driving field A_{rf}, although they can be treated in a similar manner to $\delta\varepsilon$ and $\delta\Delta$. These fluctuations are considered to be the main physical sources of decoherence in many experiments. Although they have a clear physical manifestation in the lab frame, the decoherence they cause occurs in the frame spanned by the qubit eigenbasis. To facilitate presentation in what follows, we have gathered the terms in Eq. 76 into a static Hamiltonian $\hat{\mathcal{H}}_0$ and a fluctuating Hamiltonian $\hat{\mathcal{H}}_F$.

3.1.2 Qubit frame (qubit eigenbasis)

By making the transformation,

$$\begin{aligned}\hat{\sigma}_{x'} &= \cos\theta\,\hat{\sigma}_x - \sin\theta\,\hat{\sigma}_z\ , \\ \hat{\sigma}_{y'} &= \hat{\sigma}_y\ , \\ \hat{\sigma}_{z'} &= \cos\theta\,\hat{\sigma}_z + \sin\theta\,\hat{\sigma}_x\ ,\end{aligned} \tag{77}$$

where $\theta = \arctan(\varepsilon/\Delta)$ is the rotation angle of the quantization axis from the lab frame, we can write the Hamiltonian in Eq. 76 in the qubit (eigenbasis) frame (Fig. 8b):

$$\begin{aligned}\hat{\mathcal{H}}' &= \hat{\mathcal{H}}'_0 + \hat{\mathcal{H}}'_F \\ \hat{\mathcal{H}}'_0 &= \frac{\hbar}{2}\left[\omega_{\mathrm{q}}\hat{\sigma}_{z'} + A_{\mathrm{rf}}\cos\theta\cos(\omega_{\mathrm{rf}}t + \varphi)\hat{\sigma}_{x'} + A_{\mathrm{rf}}\sin\theta\cos(\omega_{\mathrm{rf}}t + \varphi)\hat{\sigma}_{z'}\right] \\ \hat{\mathcal{H}}'_F &= \frac{\hbar}{2}\left[\left(\delta\varepsilon\sin\theta + \delta\Delta\cos\theta\right)\hat{\sigma}_{z'} + \left(\delta\varepsilon\cos\theta - \delta\Delta\sin\theta\right)\hat{\sigma}_{x'}\right]\end{aligned} \tag{78}$$

where $\omega_{\mathrm{q}} = \sqrt{\varepsilon^2 + \Delta^2}$ is the qubit's level-splitting. The coherence times T_1 and T_2 associated with free-evolution can be visualized in this reference frame (Fig. 9A and B).

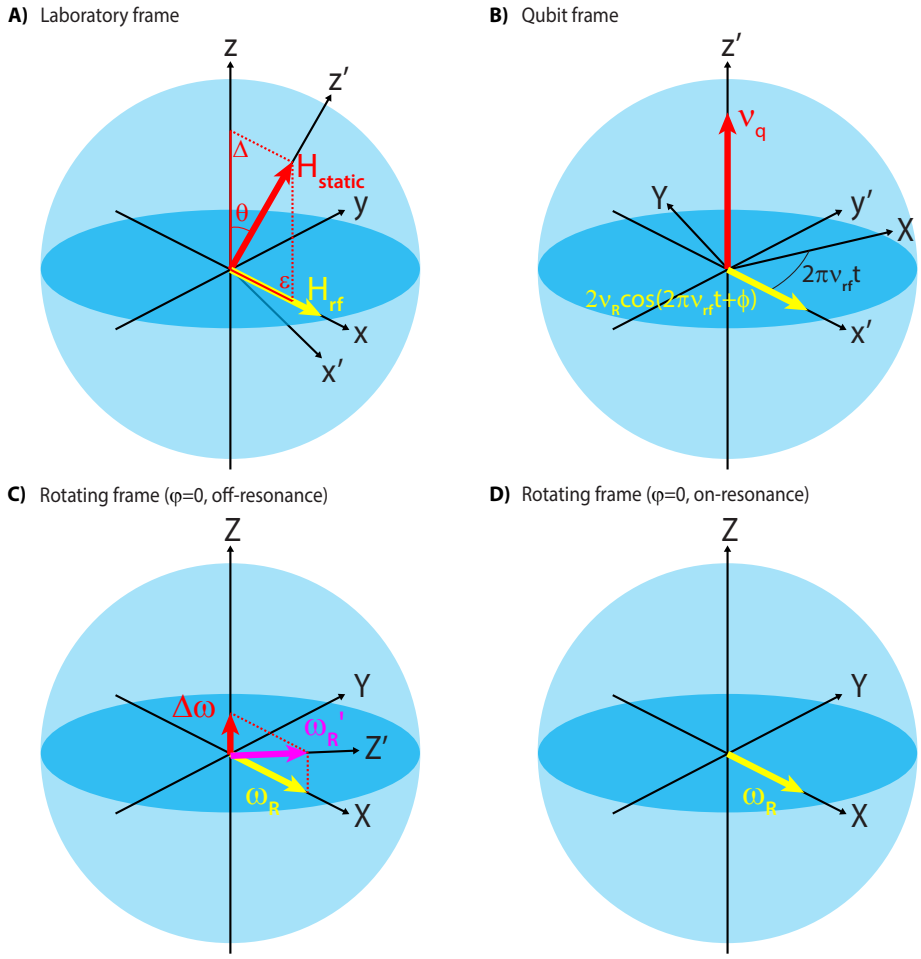

Fig. 8: The two-level system Hamiltonian represented in the Bloch picture for different reference frames. **A)** *Laboratory frame.* $\hat{\mathcal{H}}_{\rm static} = \Delta\hat{\sigma}_z + \varepsilon\hat{\sigma}_x$, $\hat{\mathcal{H}}_{\rm rf} = A_{\rm rf}\cos(\omega_{\rm rf}t + \varphi)\hat{\sigma}_x$. *$\theta$ indicates the rotation required transform into the qubit frame.* **B)** *Qubit frame. The qubit's eigenbasis. The red arrow ($\omega_{\rm q}$) is the free-evolution quantizing field. $\omega_{\rm rf}t$ indicates the time-dependent transformation required to transform into the rotating frame.* **C)** *Rotating frame ($\varphi = 0$). The pink arrow ($\omega'_{\rm R}$) indicates the effective driven-evolution quantizing (Rabi) field in the rotating frame in the presence of a finite drive-frequency detuning $\Delta\omega$.* **D)** *Rotating frame (same as (c) but with $\Delta\omega = 0$). The yellow arrow ($\omega_{\rm R}$) indicates the resonantly driven quantizing field, which corresponds to a pseudospin.*

3.1.3 Rotating frame

Driven-evolution dynamics are conveniently described in a reference frame which rotates around z' at the drive frequency $\nu_{\rm rf}$. This frame is accessed through a second transformation,

$$\begin{aligned}\hat{\sigma}_X &= \cos(\omega_{\rm rf}t)\hat{\sigma}_{x'} + \sin(\omega_{\rm rf}t)\hat{\sigma}_{y'} \ , \\ \hat{\sigma}_Y &= \cos(\omega_{\rm rf}t)\hat{\sigma}_{y'} - \sin(\omega_{\rm rf}t)\hat{\sigma}_{x'} \ , \\ \hat{\sigma}_Z &= \hat{\sigma}_{z'} \ , \end{aligned} \tag{79}$$

which applied to the Hamiltonian in Eq. 78 yields (keeping only static terms for the moment):

$$\begin{aligned}\hat{\tilde{\mathcal{H}}}_0 = \frac{\hbar}{2}\big[\Delta\omega\hat{\sigma}_Z &+ \frac{1}{2}A_{\rm rf}\cos\theta\big(\cos\varphi\,\hat{\sigma}_X + \sin\varphi\,\hat{\sigma}_Y\big) \\ &+ \frac{1}{2}A_{\rm rf}\cos\theta\big(\cos(-2\omega_{\rm rf}t-\varphi)\hat{\sigma}_X + \sin(-2\omega_{\rm rf}t-\varphi)\hat{\sigma}_Y\big) \\ &+ A_{\rm rf}\sin\theta\cos(\omega t+\varphi)\hat{\sigma}_Z\big] \ , \end{aligned} \tag{80}$$

where $\Delta\omega = \omega_{\rm q} - \omega_{\rm rf}$ is the frequency detuning between the qubit and the driving field (Fig. 8C). In the weak driving limit ($\omega_{\rm R} \ll \omega_{\rm rf}$), the last two lines in Eq. 80 can be omitted, since these rapid oscillations average to zero on any appreciable time scale of the (weakly driven) qubit dynamics in this rotating frame; this is called the rotating wave approximation. The static Hamiltonian within the rotating wave approximation is:

$$\hat{\tilde{\mathcal{H}}}_0 = (\hbar/2)\big[\Delta\omega\hat{\sigma}_Z + \omega_{\rm R}(\cos\varphi\,\hat{\sigma}_X + \sin\varphi\,\hat{\sigma}_Y)\big] \ , \tag{81}$$

where $\omega_{\rm R} = \frac{1}{2}A_{\rm rf}\cos\theta$ is the Rabi frequency under resonant driving ($\omega_{\rm rf} = \omega_{\rm q} \rightarrow \Delta\omega = 0$) (Fig. 8D). More generally, in the presence of non-zero frequency detuning $\Delta\omega$ (Fig. 8C), Eq. 81 describes an effective driving field, whose effective Rabi frequency

$$\begin{aligned}\omega'_{\rm R} &= \omega_{\rm R}\sqrt{1+(\Delta\omega/\omega_{\rm R})^2} \\ &\approx \omega_{\rm R} + \Delta\omega^2/2\omega_{\rm R} \end{aligned} \tag{82}$$

is linearly sensitive to variations in $\omega_{\rm R}$ and quadratically sensitive in $\Delta\omega$.

Within the RWA, the full Hamiltonian (static and fluctuating terms) is

$$\hat{\tilde{\mathcal{H}}} = \hat{\tilde{\mathcal{H}}}_0 + \hat{\tilde{\mathcal{H}}}_F \tag{83}$$

$$\hat{\tilde{\mathcal{H}}}_0 = (\hbar/2)\big[\Delta\omega\hat{\sigma}_Z + \omega_{\rm R}(\cos\varphi\,\hat{\sigma}_X + \sin\varphi\,\hat{\sigma}_Y)\big] \ ,$$

$$\begin{aligned}\hat{\tilde{\mathcal{H}}}_F = (\hbar/2)\big[&(\delta\Delta\cos\theta + \delta\varepsilon\sin\theta)\,\hat{\sigma}_Z \ldots \\ &+ (-\delta\Delta\sin\theta + \delta\varepsilon\cos\theta)\cos(\omega_{\rm rf}t)\hat{\sigma}_X \ldots \\ &- (-\delta\Delta\sin\theta + \delta\varepsilon\cos\theta)\sin(\omega_{\rm rf}t)\hat{\sigma}_Y\big] \ , \end{aligned} \tag{84}$$

where we have kept certain terms which contain sinusoids at frequency $\omega_{\rm rf}$, because these sinusoids will mix down any existing high-frequency components (*e.g.*, noise at frequencies $\omega \pm \omega_{\rm rf}$) of the fluctuation terms $\delta\varepsilon$ and $\delta\Delta$ to a lower frequency ω that *is* relevant for the time scales of the qubit dynamics and, therefore, cannot be omitted within the RWA. The coherence times $T_{1\rho}$ and $T_{2\rho}$ associated with driven-evolution can be visualized in this reference frame (Fig. 9C and D).

3.2 General perturbation expansion of Hamiltonian

Following Ithier *et al.* [7, 181] and using their notation, we consider a general expansion of the unperturbed Hamiltonian $\hat{\mathcal{H}}_0'$ so that we can make connections to the fluctuation terms in the laboratory, qubit, and rotating frame Hamiltonians.

The Hamiltonian in the absence of fluctuation (unperturbed Hamiltonian) is

$$\hat{\mathcal{H}} = -\frac{1}{2}\vec{H}_0(\lambda_0)\cdot\vec{\hat{\sigma}} \tag{85}$$

which is a function of parameter(s) λ_0, corresponding to the static values of flux, charge, critical current, *etc.* used to bias the qubits. Expanding to second order in the perturbation(s) $\delta\lambda$, that is, fluctuations in flux, charge, critical current, *etc.*, yields:

$$\hat{\mathcal{H}} = -\frac{1}{2}\left[\vec{H}_0(\lambda_0) + \frac{\partial\vec{H}_0}{\partial\lambda}\delta\lambda + \frac{\partial^2\vec{H}_0}{\partial\lambda^2}\frac{\delta\lambda^2}{2} + \cdots\right]\vec{\hat{\sigma}}. \tag{86}$$

Following Refs. [181, 7], we introduce the notation

$$\vec{D}_\lambda \equiv \frac{1}{\hbar}\frac{\partial\vec{H}_0}{\partial\lambda} \tag{87}$$

$$\vec{D}_{\lambda 2} \equiv \frac{1}{\hbar}\frac{\partial^2\vec{H}_0}{\partial\lambda^2} \tag{88}$$

In the eigenbasis of the qubit (section 3.1.2, Fig. 8B),

$$\hat{\mathcal{H}} = -\frac{1}{2}\hbar\left[\omega_{\rm q}\hat{\sigma}_{z'} + \delta\omega_{z'}\hat{\sigma}_{z'} + \delta\omega_\perp\hat{\sigma}_\perp\right] \tag{89}$$

$$= -\frac{1}{2}\hbar\left[\omega_{\rm q}\hat{\sigma}_{z'} + (D_{\lambda,z'}\delta\lambda + D_{\lambda 2,z'}\frac{\delta\lambda^2}{2} + \ldots)\hat{\sigma}_{z'} + (D_{\lambda,\perp}\delta\lambda + \ldots)\hat{\sigma}_\perp\right] \tag{90}$$

where $\hbar\omega_{\rm q} \equiv |\vec{H}_0(\lambda_0)| = h\nu_{\rm q}$ is the static unperturbed qubit level splitting. The longitudinal coefficients are

$$D_{\lambda,z} = \frac{\partial\omega_{\rm q}}{\partial\lambda} \tag{91}$$

$$D_{\lambda 2,z} = \frac{\partial^2\omega_{\rm q}}{\partial\lambda^2} - \frac{D_{\lambda,\perp}^2}{\omega_{\rm q}} \tag{92}$$

and the transverse coefficient is

$$D_{\lambda,\perp} = \frac{\partial\omega_\perp}{\partial\lambda} \tag{93}$$

Pure dephasing is related to the derivatives of $\omega_{\rm q}(\lambda)$, while the transverse decay (relaxation or depolarization) is related to $\omega_\perp(\lambda)$. The derivatives $\vec{D}_\lambda$ capture the Hamiltonian's sensitivity to a fluctuation $\delta\lambda$ and correspondingly to higher orders.

To calculate or simulate the effect of fluctuations in the qubit basis, Eq. 90, the first-order contribution of the fluctuations should be written using the chain rule:

$$\frac{\partial\omega_{\rm q}}{\partial\lambda} = \frac{\partial\omega_{\rm q}}{\partial\varepsilon}\frac{\partial\varepsilon}{\partial\lambda} + \frac{\partial\omega_{\rm q}}{\partial\Delta}\frac{\partial\Delta}{\partial\lambda}. \tag{94}$$

For second-order contributions, the chain rule becomes:

$$\frac{\partial^2\omega_{\rm q}}{\partial\lambda^2} = \left[\frac{\partial^2\omega_{\rm q}}{\partial\varepsilon^2}\left(\frac{\partial\varepsilon}{\partial\lambda}\right)^2 + \frac{\partial\omega_{\rm q}}{\partial\varepsilon}\frac{\partial^2\varepsilon}{\partial\lambda^2}\right] + \left[\frac{\partial^2\omega_{\rm q}}{\partial\Delta^2}\left(\frac{\partial\Delta}{\partial\lambda}\right)^2 + \frac{\partial\omega_{\rm q}}{\partial\Delta}\frac{\partial^2\Delta}{\partial\lambda^2}\right]. \tag{95}$$

The derivative of $\omega_{\rm q}$ with respect to ε and Δ from the definition $\omega_{\rm q} = \sqrt{\varepsilon^2+\Delta^2}$ accounts for the change in basis between the qubit and lab frames (i.e., the angle θ). These are written:

$$\frac{d\omega_{\rm q}}{d\varepsilon} = \frac{\varepsilon}{\left(\varepsilon^2+\Delta^2\right)^{1/2}} \tag{96}$$

$$\frac{d^2\omega_{\rm q}}{d\varepsilon^2} = \frac{\Delta^2}{\left(\varepsilon^2+\Delta^2\right)^{3/2}} \tag{97}$$

$$\frac{d\omega_{\rm q}}{d\Delta} = \frac{\Delta}{\left(\varepsilon^2+\Delta^2\right)^{1/2}} \tag{98}$$

$$\frac{d^2\omega_{\rm q}}{d\Delta^2} = \frac{\varepsilon^2}{\left(\varepsilon^2+\Delta^2\right)^{3/2}}. \tag{99}$$

We can make a connection between the first-order derivatives here and the longitudinal noise terms ($\sigma_{z'}$ terms) in Eq. 78. From a geometrical argument, since $\theta = \arctan(\varepsilon/\Delta)$,

$$\left(\frac{d\omega_{\rm q}}{d\varepsilon}\right)\delta\varepsilon = \frac{\varepsilon}{\left(\varepsilon^2+\Delta^2\right)^{1/2}}\,\delta\varepsilon = \sin\theta\;\delta\varepsilon \tag{100}$$

$$\left(\frac{d\omega_{\rm q}}{d\Delta}\right)\delta\Delta = \frac{\Delta}{\left(\varepsilon^2+\Delta^2\right)^{1/2}}\,\delta\Delta = \cos\theta\;\delta\Delta. \tag{101}$$

To make a connection to the physical noise source λ (flux, charge, critical current, *etc.*), we insert the noise sensitivities $\xi_{\varepsilon,\lambda} = d\varepsilon/d\lambda$ and $\xi_{\Delta,\lambda} = d\Delta/d\lambda$,

$$\left(\frac{d\omega_{\rm q}}{d\lambda}\right)\delta\lambda = \frac{d\omega_{\rm q}}{d\varepsilon}\frac{d\varepsilon}{d\lambda}\delta\lambda \rightarrow \sin\theta\;\xi_{\varepsilon,\lambda}\;d\lambda \tag{102}$$

$$\left(\frac{d\omega_{\rm q}}{d\lambda}\right)\delta\lambda = \frac{d\omega_{\rm q}}{d\Delta}\frac{d\Delta}{d\lambda}\delta\lambda \rightarrow \sin\theta\;\xi_{\Delta,\lambda}\;d\lambda. \tag{103}$$

For example, the flux (Φ) sensitivities in a typical persistent current qubit with tunable ε and static Δ are $\xi_{\varepsilon,\Phi} = 1$ GHz/mΦ_0 and $\xi_{\Delta,\Phi} = 0$. In general, these sensitivities are inferred either from experiment or from simulations.

3.3 Longitudinal and transverse relaxation

The dynamics of the qubit state within a two-level model can be visualized on the Bloch sphere (see Fig. 9A, B). We consider first the qubit reference frame in the absence of driving, $A_{\rm rf} = 0$. In this case, the Hamiltonian (Eq. 78) contains only the "qubit field" $\nu_{\rm q}$ (red arrow in Fig. 9) which defines the qubit quantization axis along z′.

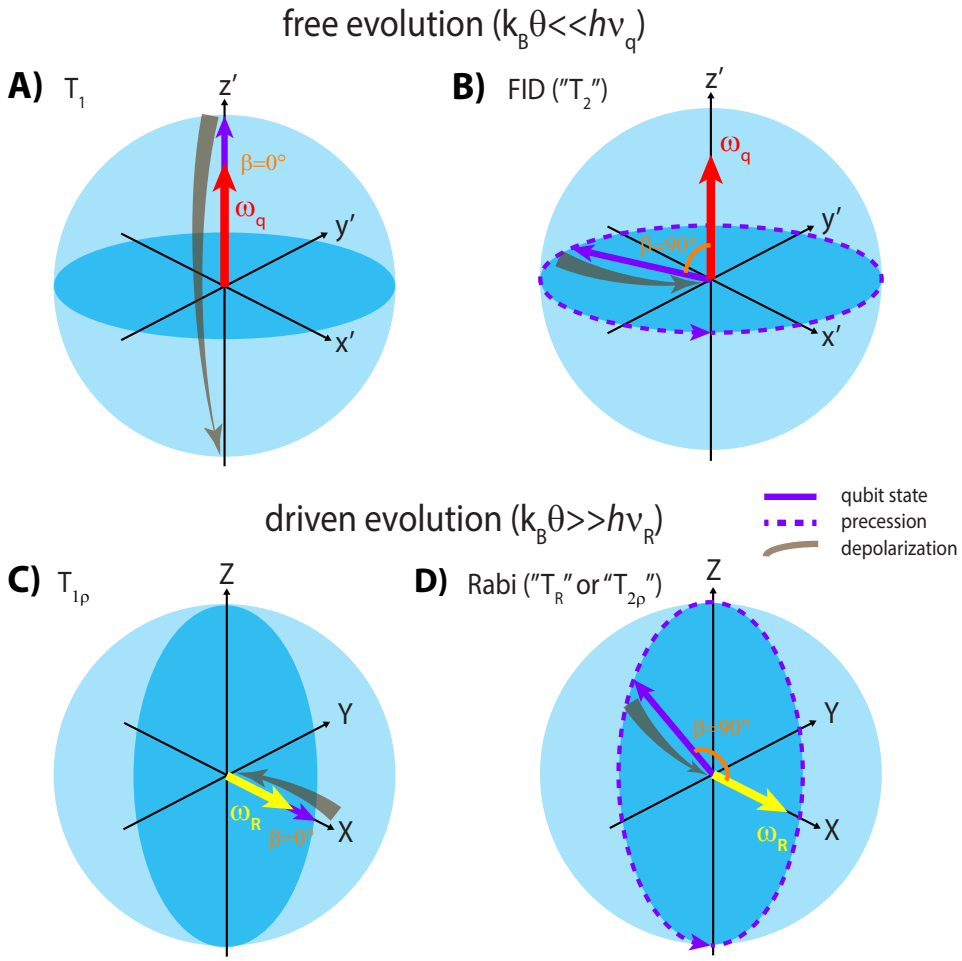

Fig. 9: Schematic diagram of system dynamics in analogous experiments between free evolution and driven evolution. **A)** *and* **B)** *illustrate depolarization during free-evolution in the qubit frame.* **A)** *longitudinal depolarization* T_1. **B)** *transverse free-induction decay (FID). The relaxation FID time is written "*T_2*", because the decay function need not be exponential, and the illustration ignores the effects due to longitudinal relaxation.* **C)** *and* **D)** *illustrate depolarization during driven-evolution in the rotating frame.* **C)** *longitudinal depolarization* $T_{1\rho}$ *in the qubit frame.* **D)** *transverse Rabi oscillations. The characteristic decay time is written "*$T_{\rm R}$*", because the decay function need not be exponential, and the illustration ignores the effects due to longitudinal relaxation. The illustrated longitudinal depolarization in* **A)** *and* **C)** *is based on the condition (typical for superconducting qubits),* $\hbar\omega_{\rm R} \ll k_{\rm B}T \ll \hbar\omega_{\rm q}$*, so that, in the steady state,* $\langle\hat{\sigma}_{z'}\rangle \approx -1$ *for the* T_1 *process, and* $\langle\hat{\sigma}_X\rangle \approx 0$ *for the* $T_{1\rho}$ *process. For the illustrated transverse depolarization in* **B)** *and* **D)***, dephasing (or dephasing-type) processes act to depolarize the Bloch vector to the origin.*

3.3.1 Bloch-Redfield approach

Within the standard Bloch-Redfield [176, 177, 178] picture of two-level system dynamics, noise sources are weakly coupled to the qubits have short correlation times with respect to the system dynamics. In this case, the relaxation processes are characterized by two rates:

$$\text{Bloch-Redfield longitudinal relaxation rate} \qquad \Gamma_1 \equiv \frac{1}{T_1}$$

$$\text{Bloch-Redfield transverse relaxation rate} \qquad \Gamma_2 \equiv \frac{1}{T_2} = \frac{\Gamma_1}{2} + \Gamma_\varphi$$

which contains the pure dephasing rate Γ_φ. Note that the definition of Γ_2 as a sum of rates is only valid if the noise spectra are Lorentzian (centered at $\omega = 0$), that is, the decay functions are exponential. For an initial state ($t = 0$)

$$\alpha|0\rangle + \beta|1\rangle, \tag{104}$$

the density matrix for the qubit is written [181, 7],

$$\rho_{\text{BR}} = \begin{pmatrix} 1 + (|\alpha|^2 - 1)e^{-\Gamma_1 t} & \alpha\beta^* e^{i\Delta\omega t} e^{-\Gamma_2 t} \\ \alpha^*\beta e^{-i\Delta\omega t} e^{-\Gamma_2 t} & |\beta|^2 e^{-\Gamma_1 t}. \end{pmatrix} \tag{105}$$

The longitudinal relaxation rate Γ_1 describes depolarization along the qubit quantization axis. It is caused by *transverse* noise, since off-diagonal elements of an interaction Hamiltonian will connect states $|0\rangle$ and $|1\rangle$. Depolarization in principle occurs due to both up (excitation from $|0\rangle$ to $|1\rangle$) and down (relaxation from $|1\rangle$ to $|0\rangle$) rates:

$$\Gamma_1 \equiv \frac{1}{T_1} = \Gamma_{1\downarrow} + \Gamma_{1\uparrow}. \tag{106}$$

In superconducting qubits, it is generally the case that $k_{\text{B}}\Theta \ll h\nu_{\text{q}}$ (although not always, e.g., see section 4.4), and the up rate is exponentially suppressed by the Boltzmann factor $\exp(-h\nu_{\text{q}}/k_{\text{B}}\Theta)$. Only noise at the qubit frequency mediates qubit transitions, whether absorption or emission, and this noise is generally "well behaved" (short correlation time, weakly coupled to qubit, no divergences) around the qubit frequency in superconducting qubits . Longitudinal depolarization measurements exhibit an exponential decay function, consistent with the Bloch-Redfield picture.

Longitudinal noise fluctuates the qubit field vector in Fig. 9B. This, in turn, varies the precession rate of the Bloch vector on the equator and causes dephasing Γ_φ. Since dephasing is not a resonant process, it is sensitive to broadband fluctuations. In superconducting qubits this noise (e.g., flux noise, charge noise, critical-current noise, ...) tends to exhibit a $1/f$-like behavior. This noise is singular near $\nu = 0$, has long correlation times, and generally does not fall within the Bloch-Redfield description. The decay function of the off-diagonal terms in Eq. 105 are generally non-exponential.

3.3.2 Modification due to $1/f$-type noise

If we assume that the qubit is coupled to many independent fluctuators, then, independent of their individual statistics, they will in concert generate noise with a Gaussian distribution due to the central limit theorem. We therefore say that the longitudinal fluctuations exhibit Gaussian-distributed $1/f$ noise. For $1/f$ noise spectra, the phase decay function is itself a Gaussian

$\exp\left[-(\Gamma_\varphi t)^2\right]$, and it factors from the T_1 exponential decay because the noise remains regular at the qubit frequency. The density matrix in Eq. 105 becomes, following Refs. [181, 11],

$$\rho = \begin{pmatrix} 1+(|\alpha|^2-1)e^{-\Gamma_1 t} & \alpha\beta^* e^{i\Delta\omega t} e^{-\frac{\Gamma_1}{2}t} e^{-\chi_N(t)} \\ \alpha^*\beta e^{-i\Delta\omega t} e^{-\frac{\Gamma_1}{2}t} e^{-\chi_N(t)} & |\beta|^2 e^{-\Gamma_1 t} \end{pmatrix}. \tag{107}$$

where the decay function $\langle \exp(-\chi_N(t)) \rangle$ contains the so-called coherence function χ_N and is used to describe dephasing. The subscript N labels the decay function, and it will refer to the number of π-pulses used to refocus the low-frequency noise, which impacts the form of the decay function.

3.4 Power spectral density (PSD)

The frequency distribution of the noise power for a stationary noise source λ is characterized by its PSD $S_\lambda(\omega)$

$$S_\lambda(\omega) = \int_{-\infty}^{\infty} d\tau \, \langle \lambda(\tau)\lambda(0) \rangle e^{-i\omega\tau}. \tag{108}$$

The PSD is the Fourier transform of the autocorrelation function $c_\lambda(\tau) = \langle \lambda(\tau)\lambda(0) \rangle$ of the noise source λ. Since the integration limits are $(-\infty, \infty)$, this is the bilateral PSD. Symmetrizing the PSD allows one to consider only positive frequencies, which is termed a unilateral PSD. Both unilateral and bilateral PSDs are used, often with the same notation, and so one needs to know how the PSD is defined, keep track of the factors of 2 and π, and also be aware of the implications for quantum systems.

For quantum systems, the autocorrelation function is in general complex due to non-commuting variables in the system (qubit-bath) Hamiltonian. This means that the PSD is not a symmetric function in frequency. Noise at a positive frequency $S(\nu_\mathrm{q})$ corresponds to energy transfer from the qubit to the environment, including both stimulated and spontaneous emission, associated with the down-rate $\Gamma_{1\downarrow}$. Noise at a negative frequency $S(-\nu_\mathrm{q})$ corresponds to energy transfer to the qubit from the environment, associated with the up-rate $\Gamma_{1\uparrow}$. For a detailed discussion, see Refs. [184, 185].

In turn, the inverse Fourier transform of the PSD will yield the autocorrelation function. This implies that integrating the noise power spectral density with $\tau = 0$ yields the variance σ_λ^2 of the noise.

$$c_\lambda(\tau) = \frac{1}{2\pi} \int_{-\infty}^{\infty} d\omega S_\lambda(\omega) e^{i\omega\tau} \tag{109}$$

$$\sigma_\lambda^2 \equiv c_\lambda(0) = \frac{1}{2\pi} \int_{-\infty}^{\infty} d\omega S_\lambda(\omega) \tag{110}$$

Making a connection between $S_\lambda(\omega)$ and the measured qubit decay functions is the basis for noise spectroscopy.

3.5 Connecting T_1 to $S_\lambda(\omega)$

The connection between $S_\lambda(\omega)$ and the measured decay time T_1 can be made using Fermi's Golden Rule, within the assumption that the qubit is weakly coupled to its environment. Considering the transition rate from excited to ground state, $\Gamma_{1\downarrow,\lambda}$ due to a particular noise source λ,

yields: (see Ref. [181, 182, 70, 185] for details):

$$\Gamma_{1\downarrow,\lambda} = \frac{2\pi}{\hbar}|m_\lambda|^2\rho(\hbar\omega_\mathrm{q}) \tag{111}$$

$$= \frac{1}{\hbar^2}|d_\lambda|^2\ S_\lambda(\omega_\mathrm{q}) \tag{112}$$

$$= \quad D^2_{\lambda,\perp}\ S_\lambda(\omega_\mathrm{q}) \tag{113}$$

where $m_\lambda \equiv \langle 1|\hat{m_\lambda}|0\rangle = \langle 1|\hat{\mathcal{H}}^{(\lambda)}_\mathrm{int}|0\rangle$, and $\hat{m}_\lambda \equiv \hat{\mathcal{H}}^{(\lambda)}_\mathrm{int} = (d\hat{\mathcal{H}}_0/d\lambda)\delta\lambda$ is the first-order interaction Hamiltonian between the qubit and the environment due to a fluctuator λ and characterized by a density of states $\rho(\hbar\omega_\mathrm{q})$ at the qubit frequency. The second line writes the expression in terms of the qubit's (energy) susceptibility d_λ to external fluctuations,

$$d_\lambda \equiv \langle 1|\hat{d_\lambda}|0\rangle = \langle 1|\frac{d\hat{\mathcal{H}}_0}{d\lambda}|0\rangle = \hbar D_{\lambda,\perp}, \tag{114}$$

which is the energy-units version of $D_{\lambda,\perp}$ in Eq. 93, and it can be interpreted as the transition dipole for the fluctuator λ [70]. Adopting a PSD is useful, since noise is typically an aggregate effect over many fluctuators, each of which may have a different matrix element m_λ. The noise PSD is correspondingly defined

$$S_\lambda(\omega_\mathrm{q}) = 2\pi\hbar(\delta\lambda)^2\rho(\hbar\omega_\mathrm{q}) \tag{115}$$

and has units of λ^2/s^{-1}. The interaction Hamiltonian and the susceptibility (transition dipole) operators are simply related,

$$\hat{d}_\lambda = \frac{\hat{m}_\lambda}{\delta\lambda}. \tag{116}$$

Examples from the Hamiltonians written in section 2.3 are presented in Table 2.

$\hat{\mathcal{H}}_\lambda$	$\delta\lambda$	$\hat{\mathbf{m}}_\lambda$	$\hat{\mathbf{d}}_\lambda$
$4E_\mathrm{C}(\hat{n}-\hat{n}_\mathrm{g})^2$	δn	$8\delta n E_\mathrm{C}\hat{n}$	$8E_\mathrm{C}\hat{n}$
$-E_\mathrm{J}\cos(\hat{\phi}+2\pi f)$	δf	$2\pi\delta f E_\mathrm{J}\sin(\hat{\phi}+2\pi f)$	$2\pi E_\mathrm{J}\sin(\hat{\phi}+2\pi f)$
$-E_\mathrm{J}\cos(\hat{\phi}+2\pi f)$	δi	$-\delta i E_\mathrm{J}\cos(\hat{\phi}+2\pi f)$	$-E_\mathrm{J}\cos(\hat{\phi}+2\pi f)$

Table 2: *Examples of interaction Hamiltonians used to calculate interaction matrix elements $\hat{m}_\lambda \equiv \hat{\mathcal{H}}_\mathrm{int}$ and susceptibilities $\hat{d}_\lambda \equiv \hat{\mathcal{H}}_\mathrm{int}/\delta\lambda$. Note that $\delta i \equiv \delta I_\mathrm{c}/I_\mathrm{c}$ is the reduced critical current fluctuation.*

With this definition, we can write a general result for the decay rate Γ_1,

$$\Gamma_{1\downarrow} = \sum_\lambda \Gamma_{1\downarrow,\lambda} = \sum_\lambda D^2_{\lambda,\perp}\ S_\lambda(\omega_\mathrm{q}) \tag{117}$$

$$\Gamma_{1\uparrow} = \sum_\lambda \Gamma_{1\uparrow,\lambda} = \sum_\lambda D^2_{\lambda,\perp}\ S_\lambda(-\omega_\mathrm{q}) \tag{118}$$

$$\Gamma_1 \equiv \frac{1}{T_1} = \Gamma_{1\downarrow} + \Gamma_{1\uparrow} \approx \Gamma_{1\downarrow} \tag{119}$$

where the approximation holds for $k_\mathrm{B}\Theta \ll \hbar\omega_\mathrm{q}$ when the qubit is in thermal equilibrium with its environment. This follows from the detailed balance of the transition rates $\Gamma_{1\uparrow} = \exp(-\hbar\omega/k_\mathrm{B}\Theta)\Gamma_{1\downarrow}$ required to obtain the correct state populations in thermal equilibrium.

3.6 Connecting T_φ to $S_\lambda(\omega)$

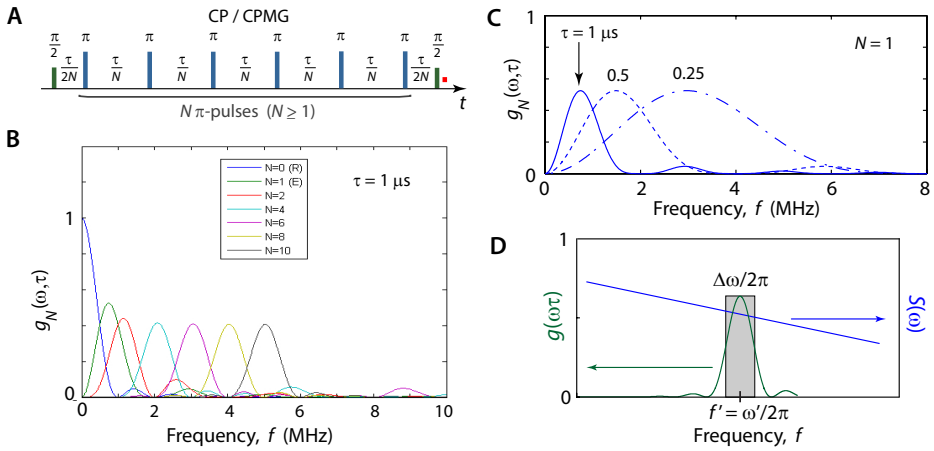

Fig. 10: Filter function $g_N(\omega,\tau)$. A) *Carr-Purcell-Meiboom-Gill sequence with N π-pulses (refocussing pulses). The total time duration between the two $\pi/2$-pulses is τ + $N\tau_\pi$, where τ is the free evolution time, and τ_π the time during during the π pulses.$N = 0$ is a Ramsey experiment, which has only free evolution and no refocusing pulses. $N = 1$ is a Hahn echo (spin echo) experiment.* **B)** *Filter function for $N = 0 \ldots 10$ with $\tau = 1$ μs. For $N = 0$, the Ramsey case, the filter function is peaked at zero frequency, making Ramsey highly susceptible to $1/f$-type noise. As the number N increases, the bandpass filter shifts to higher frequencies and thereby decreases the effective noise power dephasing the qubit. The area under all curves is the same.* **C)** *Filter function for $N = 1$ and $\tau = 0.25,\ 0.5,$ and 1 μs.* **D)** *The filter function shapes the noise PSD $S(\omega)$ and depends on the number of π-pulses N used to refocus the low-frequency noise. In turn, since it connects the PSD to the decay function, and for parameters that give a function narrow in frequency, it can be used to back out the PSD.*

We consider a superposition state undergoing free evolution. For example, we could create an equal superposition state of the qubit (on the equator of the Bloch sphere) by driving the qubit from its ground state by a $\pi/2$ pulse (Fig. 9B, qubit frame). As the superposition state undergoes free evolution, noise in the qubit field will translate to noise in the precession rate, which acts to dephase the qubit.

The superposition state's accumulated phase (relative between the two states),

$$\varphi(t) = \int_0^t \omega_q dt' = \langle\omega_\mathrm{q}\rangle t + \delta\varphi(t) \tag{120}$$

diffuses due to adiabatic fluctuations of the transition frequency,

$$\delta\varphi(t) = (\partial\omega_\mathrm{q}/\partial\lambda)\int_0^t \mathrm{d}t'\delta\lambda(t') = D_{\lambda,z}\int_0^t \mathrm{d}t'\delta\lambda(t'), \tag{121}$$

where $\partial\omega_\mathrm{q}/\partial\lambda = D_{\lambda,z}$ (see Eq. 91) is the qubit's longitudinal sensitivity to λ-noise. For noise generated by a large number of fluctuators that are weakly coupled to the qubit, its statistics are Gaussian. Ensemble averaging over all realizations of the Gaussian-distributed stochastic process $\delta\lambda(t)$, the dephasing is

$$\langle e^{i\,\delta\varphi(t)}\rangle = e^{-\frac{1}{2}\langle\delta\varphi^2(t)\rangle} \equiv e^{-\chi_N(t)}, \tag{122}$$

with the coherence integral

$$\chi_N(\tau) = \frac{\tau^2}{2} \sum_{\lambda} \left(\frac{\partial \omega_{\mathrm{q}}}{\partial \lambda} \right)^2 \int_{-\infty}^{\infty} \mathrm{d}\omega \, S_\lambda(\omega) \, g_N(\omega, \tau), \tag{123}$$

where τ is the free evolution time, N will denote the number of π pulses (if any, $N = 0$ allowed) in pulse sequences applied to the qubit to reduce the noise (e.g., $N = 1$ is the Hahn echo, $N > 1$ are CPMG, *etc.*) [189, 190, 11], and g_N is a dimensionless weighting function defined in equation (124).

The function $g_N(\omega, \tau)$ can be viewed as a frequency-domain filter of the noise $S_\lambda(\omega)$. In general, its filter properties depend on the number N and distribution of π-pulses [191, 189, 192, 190, 193, 11],

$$g_N(\omega, \tau) = \frac{1}{(\omega\tau)^2} \left| 1 + (-1)^{1+N} \exp(i\omega\tau) + 2 \sum_{j=1}^{N} (-1)^j \exp(i\omega\delta_j\tau) \cos(\omega\tau_\pi/2) \right|^2, \tag{124}$$

where $\delta_j \in [0, 1]$ is the normalized position of the centre of the jth π-pulse between the two $\pi/2$-pulses, τ is the total free-induction time, and τ_π is the length of each π-pulse [190, 193], yielding a total sequence length $\tau + N\tau_\pi$. As the number of pulses increases for fixed τ, the filter function's peak shifts to higher frequencies (Fig. 10B), leading to a reduction in the net integrated noise (Eq. 123) for $1/f^\alpha$-type noise spectra with $\alpha > 0$. Similarly, for a fixed N, the filter function will shift in frequency with τ (Fig. 10C). Additionally, for a fixed time separation $\tau' = \tau/N$ (valid for $N \geq 1$), the filter sharpens and asymptotically peaks at $\omega'/2\pi = 1/2\tau'$ as more pulses are added (Fig. 10D). Note that we have have purposefully written $g_N(\omega, \tau)$ as a band-pass filter (Fig. 10), which we will effectively utilize to sample the environmental noise $S_\lambda(\omega)$ by varying the number of pulses N and the total sequence time τ. This interpretation can be contrasted with several previous works [189, 194, 192, 190, 193], in which the quantity $(\omega\tau)^2 g_N(\omega, \tau)$ was interpreted as a high-pass filter acting on a phase noise $S_\lambda(\omega)/\omega^2$.

In the $N = 0$ case, a Ramsey experiment, the decay function is

$$e^{-\chi_0(t)} = \langle e^{i\Delta\phi(t)} \rangle = e^{-\frac{1}{2}\langle \Delta\phi(t)^2 \rangle} \tag{125}$$

$$= \exp\left[\frac{t^2}{2} D_{\lambda,z}^2 \int_{-\infty}^{\infty} d\omega \; S_\lambda(\omega) \mathrm{sinc}^2 \frac{\omega t}{2} \right] \tag{126}$$

$$\equiv \exp\left[\frac{t^2}{2} D_{\lambda,z}^2 \int_{-\infty}^{\infty} d\omega \; S_\lambda(\omega) g_0(\omega, t) \right]. \tag{127}$$

which follows from Eqs. 108, 121, and 122. The Ramsey decay function is proportional to a sinc-function (Fig. 10B) which is centered at $\omega = 0$. For noise that decreases with frequency, *e.g.*, $1/f$-type noise in superconducting qubits, the Ramsey experiment windows $S(\omega)$ where it has the highest value. In this sense, it is a worst possible (noisiest) choice of filter function (see Fig. 11A).

In the $N = 1$ case, a Hahn echo (spin echo) experiment, there is a single π-pulse that is applied at time $\tau/2$ which acts to refocus the Bloch vector. The phase fluctuation $\delta\phi_E(t_1, t_2)$ during the two periods t_1 and t_2 of free evolution is

$$\Delta\phi_E(t_1, t_2) \equiv -\Delta\phi_{t1} + \Delta\phi_{t2} = -D_{\lambda,z} \int_0^{t1} dt' \; \delta\lambda(t') + D_{\lambda,z} \int_{t_1}^{t_1+t2} dt' \; \delta\lambda(t') \tag{128}$$

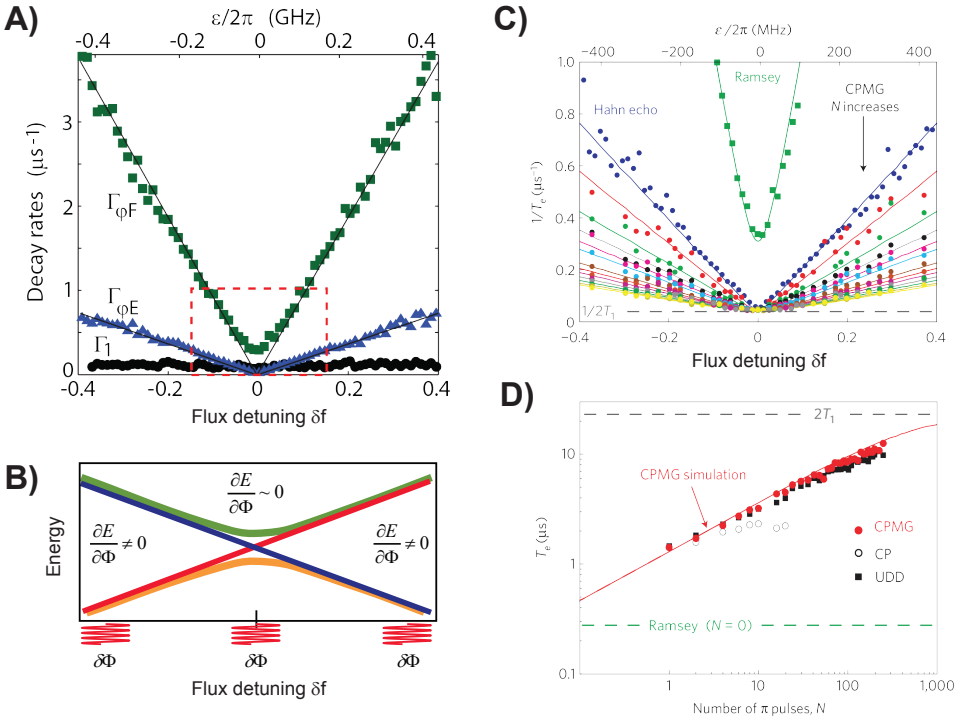

Fig. 11: Dephasing and its relation to Ramsey, spin echo, and CPMG dynamical decoupling *[11].* **A)** *The free-induction Ramsey decay rate* $\Gamma_{\phi \mathrm{F}}$*, spin-echo decay rate* $\Gamma_{\phi \mathrm{E}}$*, and energy relaxation rate* Γ_1 *as a function of flux detuning* $\delta f \equiv f - 1/2$ *for the qubit shown in Fig. 13.* $\Gamma_{\phi \mathrm{F}}$ *is generally larger than* $\Gamma_{\phi \mathrm{E}}$ *due to the filter function. At the degeneracy point* $\delta f = 0$*,* $\Gamma_{\phi \mathrm{F}}$ *and* $\Gamma_{\phi \mathrm{E}}$ *are smallest due to the qubit's first-order protection from flux noise. At this point,* $\Gamma_{\phi \mathrm{E}} = \Gamma_1/2$*,* i.e., $T_{2\mathrm{E}} = 2T_1$*.* **B)** *Energy level diagram illustrating the sensitivity* $\partial E/\partial \Phi$ *due to fluctuation in the flux* $d\Phi$*. At the degeneracy point* $\delta f = 0$*, the energy levels have zero slope, and the qubit is first-order insensitive to flux noise. At* $\delta f \neq 0$*, the energy levels shift with flux, and the qubit is therefore sensitive to flux noise.* **C)** *Decay rates for Ramsey (*$N = 0$*), Hahn (spin) echo (*$N = 1$*), and CPMG with* $N = 1,\ 2,\ 4,\ 6,\ 8,\ 10,\ 16,\ 20,\ 24,\ 30,\ 36,\ 42,\ 48$*. As* N *increases, the filter function* g_N *shifts to higher frequencies, and so the qubit becomes less sensitive to* $1/f$ *flux noise. At degeneracy, a single* π *pulse improves the decay rate to* $\Gamma_2 = \Gamma_1/2$*.* **D)** *Away from degeneracy,* $\delta f = -0.4$ mΦ_0*, the qubit is highly sensitive to flux noise. Increasing* N *up to 200 pulses improves the decay time towards the* $T_2 = 2T_1$ *limit. CPMG (*π*-pulses in quadrature to* $\pi/2$*-pulses) is compared with CP (all pulses in phase) and UDD (sinusoidal pulse spacing) pulse sequences (see Fig. 12 and Ref. [11]).*

and using $t_1 = t_2 = \tau/2$, the echo decay function is

$$e^{-\chi_1(t)} = \left\langle e^{i\Delta\phi_E(t_1=t_2)} \right\rangle = e^{-\frac{1}{2}\langle \Delta\phi_E(t_1=t_2)^2 \rangle} \tag{129}$$

$$= \exp\left[\frac{t^2}{2} D_{\lambda,z}^2 \int_{-\infty}^{\infty} d\omega \; S_\lambda(\omega) \sin^2 \frac{\omega t}{4} \mathrm{sinc}^2 \frac{\omega t}{4} \right] \tag{130}$$

$$\equiv \exp\left[\frac{t^2}{2} D_{\lambda,z}^2 \int_{-\infty}^{\infty} d\omega \; S_\lambda(\omega) g_1(\omega, t) \right]. \tag{131}$$

In Fig. 10B, the $N = 1$ filter function peaks away from $\omega = 0$. For noise that decreases with frequency, as is the case with superconducting qubits, this is advantageous; the integrated noise and, thereby, the decay rate is lower with the echo than with the Ramsey experiment.

The general trend is confirmed as a function of flux detuning $\delta f \equiv f - 1/2$ in Fig. 11A. At the degeneracy point $\delta f = 0$, the qubit is first-order insensitive to flux fluctuations (Fig. 11B)), and so the decoherence rates are lowest at this bias. In fact, the echo rate is T_1-limited, $\Gamma_{\mathrm{E}} = \Gamma_1/2$. Away from $\delta f = 0$, the qubit becomes more sensitive to flux fluctuations, and so both the Ramsey and echo decoherence rates increase [8, 11]. However, since the echo filter function g_1 peaks at higher frequency than the Ramsey filter function g_0, and because the flux noise is $1/f$ type, the echo decay rate is better than the Ramsey decay rate, $\Gamma_{\mathrm{E}} < \Gamma_{\mathrm{R}}$, for any flux bias. The relaxation rate Γ_1 is observed to relatively constant over this range of flux.

This concept extends for N π-pulses in a CPMG experiment (Fig. 11C and Fig. 12). As the number of pulses, N, increases, the filter function g_N continues peak at higher and higher frequencies, reducing the integrated noise seen by the qubit, and so the decay rates Γ_N continue to improve.

The filter functions in Eq. 124 and plotted in Fig. 10B all have the same integrated area. Therefore, if the noise PSD is white noise (uniform with frequency), then there will be no difference in the integrated noise for any number N. Similarly, if a system has a PSD that increases with frequency, than adding more pulses will increase the noise seen by the qubit and therefore decrease its coherence times.

3.7 Noise spectroscopy of a persistent-current flux qubit

In this section, we review several experiments which probe coherence metrics of a persistent-current flux qubit during both free evolution (T_1 and T_2) and driven evolution ($T_{1\rho}$ and $T_{2\rho} = T_{\mathrm{R}}$), where the subscript ρ refers to "rotating frame," and T_{R} is the Rabi decay time. By analyzing the form of the decay function (see Table 3), we can extract information about the noise spectra seen by the qubit in the laboratory frame. In turn, these pulse sequences can be used to mitigate dephasing. The CPMG pulse sequence mitigates dephasing T_ϕ during free evolution, and the rotary echo can mitigate dephasing $T_{\phi\rho}$ during driven evolution.

The device used in this section is a 4-junction persistent current flux qubit (see Fig. 13A) with the small junction a factor $\alpha = 0.54$ smaller in area than the remaining identically sized junctions. The qubit states are coupled with a strength $\Delta \approx 5.4$ GHz, $E_{\mathrm{J}} = 210$ GHz, and $E_{\mathrm{C}} = 4$ GHz. The qubit is read out using a DC SQUID, which is galvanically connected to the qubit to leverage the kinetic inductance of the shared lines, approximately 30 pH, to increase the readout signal. The device was fabricated at NEC using an aluminum double-angle shadow evaporation process, and measurements were made at MIT. For more details regarding the qubit parameters and the measurement setup, see Ref. [11].

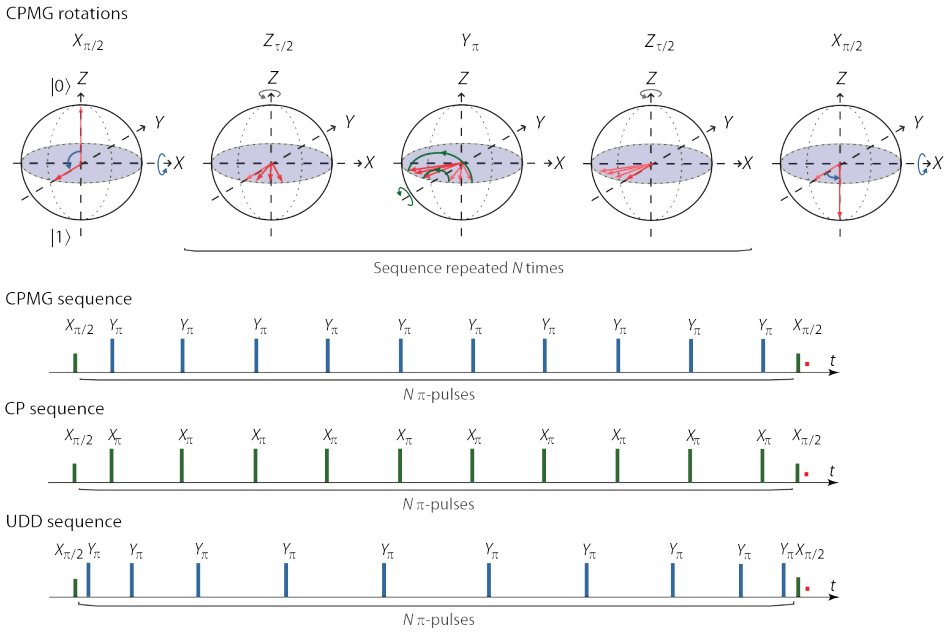

Fig. 12: CP, CPMG, and UDD dynamical decoupling *[11].* **A)** *Bloch sphere representation of refocussing sequences. The Carr-Purcell (CP) sequence has all pulses in phase and equally spaced. The Carr-Purcell-Meiboom-Gill (CPMG) sequence has the π-pulses in quadrature to the $\pi/2$-pulses and equally spaced. The UDD sequence has the π-pulses in quadrature to the $\pi/2$-pulses and the pulses are spaced sinusoidally in time. CPMG is less sensitive to pulse imperfections than CP. For $1/f$ type noise, CPMG and UDD give similar performance.*

Note that in the following, the label T_2 is simply used to designate a process (transverse relaxation), even though the decay function need not be exponential. The actual decay functions are listed in Table 3.

3.7.1 Inversion recovery: T_1

Longitudinal relaxation in the qubit frame is measured via an inversion recovery experiment. The qubit is prepared in its excited state, and the readout is delayed with respect to this preparation pulse in order to monitor the time it takes for the qubit to decay back to the ground state (see pulse sequence in Fig. 13B). As the qubit is not begin driven during the decay period, inversion recovery is a measure of energy decay during free evolution (Fig. 9A).

A typical decay trace taken at the qubit degeneracy point, $f = 0.5$, is shown in Fig. 13B [11]. In this example, $T_1 = 12$ μs. For most superconducting qubits, the observed decay function is exponential. However, the decay function can become non-exponential due to experimental factors, *e.g.*, repeating an experiment too rapidly, which can lead to a non-equilibrium quasiparticle accumulation.

By measuring thd T_1 time versus qubit frequency, we were able to map the noise PSD at frequencies above 5.4 GHz (see Fig. 14A) [11].

3.7.2 Free-induction decay (Ramsey): T_2^*

Transverse relaxation in the qubit frame is measured via a free-induction decay measurement, or Ramsey measurement. The pulse sequence is shown in Fig. 13B, and it comprises a pair of $\pi/2$ pulses. The first pulse brings the Bloch vector to the equator. In the qubit frame, the spin will precess about the the qubit field $\omega_{\rm q}$ (see Fig. 9B). After a time τ, the second $\pi/2$ pulse followed by measurement will project the state against the quantization axis. This projection as a function of τ defines the decay function.

Fluctuations in the qubit frequency will cause the spin to precess at a faster or slower rate, leading to dephasing. Due to $1/f$-type flux noise, the dephasing decay function is typically Gaussian rather than exponential (see Table 3). Repeated trials of the experiment will likely have different precession rates due to low-frequency fluctuations, and it is not possible to "identically prepare" the qubit for each trial. This type of "temporal inhomogeneity" can be compared with the spatially inhomogeneous field distribution in an atomic lattice. The "*" is used to indicate inhomogeneous broadening. In Fig. 13B, the decay function is not purely exponential, but is a combination an exponential function related to T_1 and the Gaussian dephasing function for T_ϕ. The $1/e$ time (the time to reach a factor$1/e$ of the initial value, not an exponential decay time) is 2.5 μs for this device at $f = 0.5$. Despite the qubit being biased at $f = 0.5$, there was enough residual Δ noise in this qubit to dephase the qubit and keep $T_2^* < T_1$ (we were able to rule out second-order flux noise, see Ref. [11]).

It should be noted that the decay trace shown in Fig. 13B is usually interpreted within a frame rotating at the qubit frequency. Detuning the frequency of the $\pi/2$ pulses then results in oscillations at the detuning frequency as observed in Fig. 13B. We have instead chosen to view the Ramsey experiment in the qubit frame to make a clear analogy between the T_2 of free-evolution (Fig. 9B) and the $T_{2\rho}$ of driven evolution (Fig. 9D).

Finally, by rapidly sampling repeated Ramsey measurements, we were able to measure the noise PSD in the 10^{-4} - 10^2 Hz limit (see Fig. 14A) [11, 138].

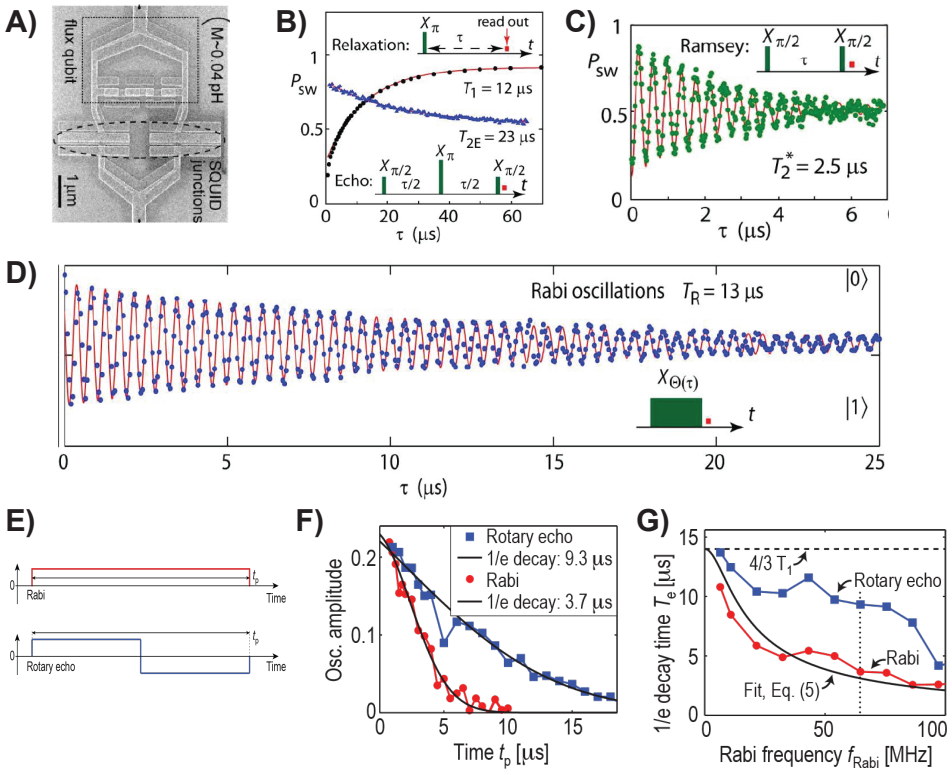

Fig. 13: Free- and driven evolution of a flux qubit. **A)** *SEM image of the flux qubit and SQUID [11].* **B)** *Inversion recovery experiment to extract the relaxation time T_1 (black line). Hahn (spin) echo experiment to extract the echo time T_{2E}. Both traces taken at the flux qubit degeneracy point.* **C)** *Ramsey interferometry with inhomogeneously broadened $T_2^* = 2.5$ μs, measured at the flux qubit degeneracy point.* **D)** *Rabi oscillations at the flux qubit degeneracy point. The Rabi time $T_R \equiv T_{2\rho}$ is approximately T_1 limited: $T_R = 4/3T_1$.* **E)** *Comparison of Rabi and rotary echo pulse sequences. The rotary echo is the driven-evolution analog of spin echo.* **F)** *$1/e$ decay times for a Rabi and rotary echo experiment for a particular driving amplitude (Rabi frequency), and* **G)** *as a function of driving amplitude (Rabi frequency).*

3.7.3 Hahn echo (spin echo): $T_{2\mathrm{E}}$

The Hahn (spin) echo (see Section 3.6) is a Ramsey experiment with a single π-pulse located midway between the two $\pi/2$-pulses. For low-frequency fluctuations, this π pulse serves to refocus the errant precession of the Bloch vector. This is achieved (in an ensemble sense) by "swapping" the leading and lagging spins on the equator such that they will all meet (refocus) at the same point and time coincident with the second $\pi/2$-pulse. How "low" a frequency is "low enough" is dictated by the filter function g_1 described in Section 3.6, but, intuitively, the noise cannot change significantly over the refocusing time.

The spin echo pulse sequence shown in Fig. 13B was implemented with the qubit biased at $f = 0.5$, the first-order flux insensitive point. In this qubit, and at this bias point, the echo was efficient, that is, $T_{2E} = 23\ \mu\mathrm{s} \approx 2T_1$. This means that the observed decay trace is exponential (it is limited by T_1), and the dephasing time after refocussing exceeds $100\ \mu\mathrm{s}$.

3.7.4 CPMG (multi-pulse refocussing): $T_2^{(N)}$

Away from $f = 0.5$, where the qubit is more susceptible to flux noise, the echo was less efficient as described in Section 3.6. In this case, adding additional, equally spaced π-pulses (CPMG) improved the refocussing efficiency. This is because the filter function peak moves to higher frequencies with larger numbers of pulses. Characterizing the decay functions for N-pulse CPMG sequences in conjunction with the filter function enabled the reconstruction of the PSD (see Fig. 10, Fig. 14A) [11].

3.7.5 Rabi oscillations: $T_{2\rho} \equiv T_{\mathrm{R}}$

Decay during driven evolution is typically measured via a Rabi experiment (Fig. 13D). The qubit is prepared in its ground state. A harmonic field then continuously drives the qubit state for a time τ, and then a measurement projects the qubit state on the measurement axis. This projection as a function of τ determines the Rabi decay function. The observed decay time at $f = 0.5$ is $T_{\mathrm{R}} = 13\ \mu s$, nearly T_1 limited ($T_{\mathrm{R}} \approx 4/3T_1$).

The Rabi experiment can be viewed in the rotating frame (Fig. 9D) as "precession" about the driving field ω_{R} in the plane perpendicular to the driving field vector. This is analogous to the Ramsey precession about the qubit field in the free-evolution case (Fig. 9D). Within this language, the decay time T_{R} is alternatively called $T_{2\rho}$.

Unless limited by T_1 (as it is here at the degeneracy point), the Rabi decay function is generally not exponential. The corresponding decay function is somewhat complicated due to low-frequency noise of the driving field and qubit parameters (see Table 3). Nonetheless, noise at the Rabi frequency can be extracted using the functions in Table 3 to infer points on the PSD (yellow dots, Fig. 14A)) [11, 186].

3.7.6 Rotary echo: $T_{2\rho\mathrm{E}}$

The rotary echo pulse sequence (Fig. 13E) is the driven-evolution analog to the spin echo. To implement rotary echo, the Rabi driving field is split into two equally sized sections, with the driving field phase flipped 180 degrees for the second section. This results in the driving field going from $+X$ to $-X$ in Fig. 9D. As a result, the spin "precesses" about the driving field in the opposite direction, ideally returning to its starting point. If the driving field has low-frequency amplitude fluctuations, the "precession frequency" (Rabi frequency) will also

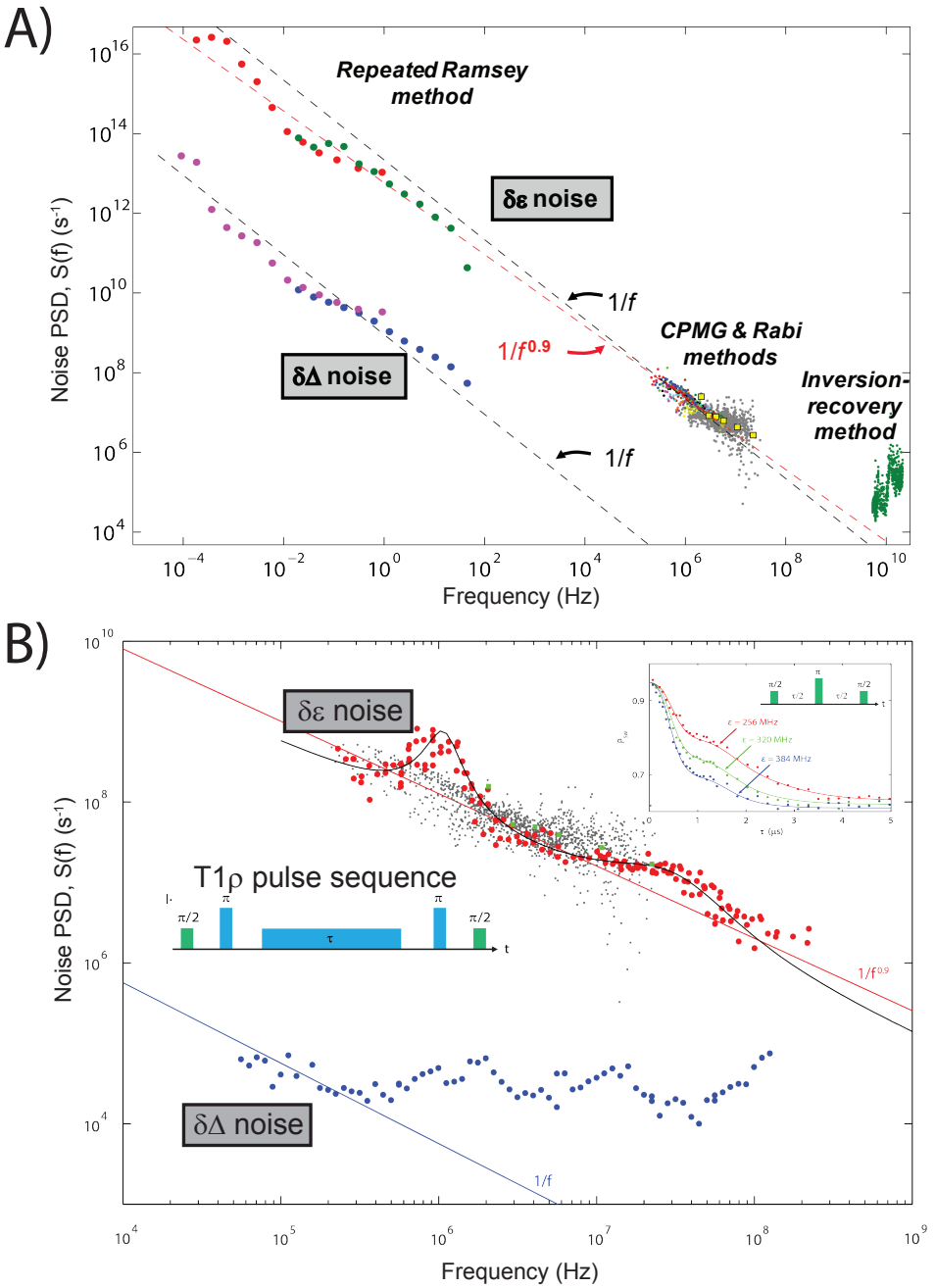

Fig. 14: Noise power spectral densities ($\delta\varepsilon$ noise and $\delta\Delta$ noise) for of a flux qubit during free- and driven evolution. **A)** *Noise spectroscopy during free evolution [11]. A low-frequency Ramsey method is used to obtain the PSD in the frequency range* 10^{-4} *to* 10^{2} *Hz range. CPMG is used to measure the noise in the* 50 *kHz - 20 MHz range. The yellow points are derived from Rabi measurements (driven evolution). The high frequency noise is measured through inversion recovery (green data).* **B)** *Noise spectroscopy of a flux qubit during driven evolution [186]. The* $T_{1\rho}$ *pulse sequence is used to extract relaxation and dephasing in the with respect to the driving field in the rotating frame. The* $\delta\varepsilon$ *noise exhibits Lorentzian features, corresponding to defects. The defect at 1 MHz is observed to be active in a free-evolution echo experiment (inset).*

change. By reversing the direction of the spin evolution, this low-frequency noise is mitigated. Fig. 13F shows a standard Rabi decay trace and the corresponding rotary echo decay trace for a given driving field amplitude (Rabi frequency), and Fig. 13G presents the extracted decay times as a function of the driving field amplitude (Rabi frequency). The rotary echo exhibits longer decay times $T_{2\rho\mathrm{E}}$ than the Rabi oscillation decay time $T_{2\rho} = T_{\mathrm{R}}$ [140].

3.7.7 Spin locking: $T_{1\rho}$

$T_{1\rho}$ is an inversion-recovery-type experiment during driven evolution, and spin locking is a means to measure it. The spin-locking sequence is shown in Fig. 14B inset. The spin vector is first brought to the equator with a $\pi/2$ pulse. Then, a driving field is applied colinear with the spin vector (Fig. 9C). In the rotating frame and under resonant driving conditions, the driving field establishes a new quantization axis, and the spin is now pointing along this axis. This is analogous to the spin being collinear with the qubit quantization axis in the free-evolution case (Fig. 9A). The distinction for the driven evolution case is that the Rabi frequency is typically in the 10-100 MHz range, which is much smaller than the thermal energy at the operating temperature. As a result, both the up and down relaxation rates $\Gamma_{1\rho\uparrow}$ and $\Gamma_{1\rho\downarrow}$ contribute to depolarization. And, as with T_1, the decay function for $T_{1\rho}$ tends to be exponential provided the noise is "regular" about the Rabi frequency, which it generally is (see Table 3). The exponential decay function (with no oscillations) is straightforward to analyzer compared with the relatively complicated Rabi decay function. Using the $T_{1\rho}$ method, we extracted the noise PSD during driven evolution over a frequency range 50 kHz - 200 MHz for both $\delta\varepsilon$ and $\delta\Delta$. Interestingly, we observed two Lorentzian features in the $\delta\varepsilon$ noise during driven evolution. The 1-MHz feature was also manifest in the free-evolution spin-echo experiment (inset, Fig. 14B), causing a sharp drop in coherence around $1\ \mu\mathrm{s}$ when the echo filter function passes through $1\mathrm{MHz}$.

4 Control of superconducting qubits in the strong-driving limit

Due to their relatively large size, superconducting artificial atoms can be strongly coupled to their external control fields. It is this feature, along with their quantum coherence, that we utilize in the present section. A large-amplitude harmonic control field can drive an artificial atom throughout its energy-level spectrum. When driven through an avoided level crossing, a Landau-Zener-Stückelberg (LZS) transition occurs. This is a coherent process akin to a beamsplitter for photons, taking an input state of the atom and outputting a superposition of states. Repeated passages through an avoided crossing act as an atom interferometer, causing the atomic superposition state to interfere quantum mechanically with itself. Since the weighting of the superposition state depends sensitively on the size of the avoided crossing and the velocity with which it is traversed, the quantum interference reflects the energy spectrum of the artificial atom. In turn, the quantum interference can be leveraged to facilitate non-adiabatic quantum control.

We begin this sesction with an overview of Landau-Zener-Stückelberg (LZS) transitions. We then present three experimental works that utilize LZS transitions in a strongly-driven persistent-current qubit [127, 128]. The first is Mach-Zehnder-type interferometry between repeated LZS transitions [38], for which we observed quantum interference fringes in n-photon transition rates, with n=1 ... 50 [39]. The second is microwave-induced cooling [44], by which we achieved effective qubit temperatures less than 3 mK, a factor 10-100 times lower than

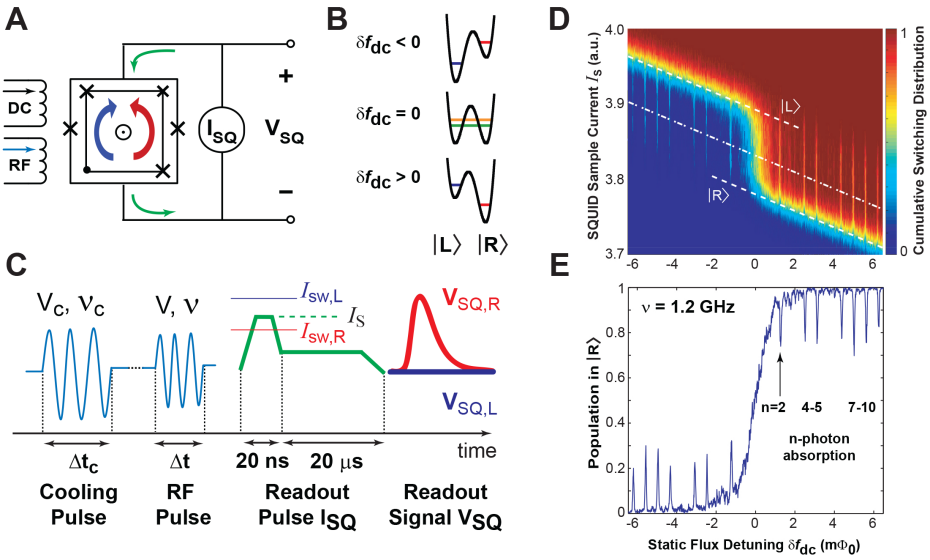

Fig. 15: Artificial atom (persistent current qubit) and measurement set-up. A) *Schematic of the qubit and surrounding DC SQUID readout.* **B)** *Double well qubit potential comprising energy levels for static magnetic flux bias δf_{dc} about $\Phi_0/2$, where Φ_0 is the superconducting flux quantum. Diabatic states of the left (right) well corresponds to a persistent current with clockwise (counterclockwise) circulation. At detuning $\delta f_{dc} = 0$, the double-well potential is symmetric and the diabatic-state energies are degenerate.* **C)** *Qubit excitation and read-out pulse sequence. The qubit is first prepared in its ground state with a harmonic cooling pulse with amplitude V_c and frequency ν_c. Quantum-state transitions are induced with a subsequent harmonic RF pulse with amplitude V and frequency ν. The qubit state is read-out using the DC SQUID switching response.* **D)** *Qubit step. Cumulative switching current distribution of the SQUID for each δf_{dc} value following a 3-μs RF driving pulse at 1.2 GHz applied to the qubit. Resonant multiphoton transitions (of order n) are observed between states $|L\rangle$ and $|R\rangle$.* **E)** *The switching distribution along the dashed-dotted line discriminates between states $|L\rangle$ and $|R\rangle$.*

the environmental temperature. The third is amplitude spectroscopy [50, 51], a spectroscopy technique that monitors the system response to amplitude rather than frequency. Amplitude spectroscopy allowed us to probe the energy spectra of our artificial atom from 0.01 - 120 GHz, while driving it at a fixed frequency equal to 0.16 GHz. Finally, we consider the application of LZS transitions to quantum information science and technology.

4.1 Flux qubit parameters

In this section, we use a superconducting persistent-current qubit to implement an artificial atom [127, 128]. In this implementation, the persistent-current qubit is a superconducting loop interrupted by three Josephson junctions (Fig. 15A). When biased with a static magnetic flux $f_{\rm dc} \sim \Phi_0/2$, where Φ_0 is the superconducting flux quantum, the system assumes a double-well potential profile (Fig. 15B). The diabatic state of the left (right) well corresponds to a persistent current $I_{\rm p}$ with clockwise (counterclockwise) circulation. The lowest two diabatic energy levels have a separation $\varepsilon = 2I_{\rm p}\delta f_{\rm dc}$ linear in the flux detuning $\delta f_{\rm dc} \equiv f_{\rm dc} - \Phi_0/2$. Higher-excited states of the double-well potential (see Fig. 19C) will be considered in Subsections 4.4 and 4.5.

The two-level Hamiltonian for the lowest two diabatic states is shown in Eq. 132. At

detuning $\delta f_{\rm dc} = 0$, the double-well potential is symmetric and the diabatic-state energies are degenerate. At this "degeneracy point," resonant tunneling between the diabatic states opens an avoided level crossing of energy Δ. Here, the qubit states are σ_x eigenstates, corresponding to symmetric and anti-symmetric combinations of diabatic circulating-current states. Detuning the double-well away from this point tilts the double well, allowing us to tune the eigenstates and eigenenergies of the artificial atom. Far from the degeneracy point, the qubit states are approximately σ_z eigenstates and have well-defined circulating current. The qubit is read out using a hysteretic DC SQUID (superconducting quantum interference device), a sensitive magnetometer that can distinguish the flux generated by circulating current states.

In addition to the static flux biases, the artificial atom is controlled and read out using the pulses illustrated in Fig. 15C. As we describe below, the qubit is first prepared in its ground state using a harmonic cooling pulse with amplitude $V_{\rm c}$ and frequency $\nu_{\rm c}$. Quantum-state transitions are then driven using a harmonic RF pulse with amplitude V and frequency ν. These fields are mutually coupled to the qubit through a small antenna. This is followed by a SQUID readout current pulse using the "sample and hold" technique [30, 38]. If the sample current exceeds the SQUID switching current, a voltage pulse will appear at the output during the hold phase. Threshold detection looks for the presence or absence of a SQUID voltage, and this constitutes a digital measurement of the qubit state. Alternatively, although not used in these experiments, we have incorporated the SQUID into a resonant circuit and realized qubit readout via the shift in resonance frequency and phase for both the linear and non-linear resonance regimes [87, 91].

The "qubit step" is shown in Fig. 15D as a function of the SQUID sample current and the flux detuning. The diabatic states $|L\rangle$ and $|R\rangle$ correspond to different levels of sample current (dashed lines) located symmetrically about the degeneracy point $\delta f_{\rm dc}$=0. This plot constitutes a cumulative switching current distribution of the SQUID for each $\delta f_{\rm dc}$ value. Additionally, a 3-μs RF pulse at 1.2 GHz is applied to the qubit, and resonant transitions can be observed as fingers extending down (up) from state $|L\rangle$ ($|R\rangle$) when n$\times$1.2 GHz becomes resonant with the energy-level separation. A best-estimator (dashed-dotted line) can be determined to provide the best statistical discrimination between states $|L\rangle$ and $|R\rangle$. The resulting qubit step with its saturated n-photon resonances along the best estimator line is shown in Fig. 15E.

The device used in this work was fabricated at Lincoln Laboratory using a fully-planarized niobium trilayer process and optical lithography. It has a critical current density $J_{\rm c} \approx 160\,{\rm A/cm^2}$, and the characteristic Josephson and charging energies are $E_{\rm J} \approx (2\pi\hbar)300\,{\rm GHz}$ and $E_{\rm C} \approx (2\pi\hbar)0.65\,{\rm GHz}$ respectively. The ratio of the qubit JJ areas is $\alpha \approx 0.84$, and $\Delta \equiv \Delta_{0,0} \approx (2\pi\hbar)10\,{\rm MHz}$. Although dependent on the flux detuning, the approximate values for coherence times are: interwell relaxation time $T_1 \sim 100\,\mu$s, intrawell relaxation time $T_1 \sim 0.1\,\mu$s, homogeneous transverse decay time $T_2 \sim 20\,$ns, inhomogeneous transverse decay time $T_2^* \sim 10\,$ns. The experiments were performed in a dilution refrigerator at a base temperature of 20 mK. The device was magnetically shielded, and all electrical lines were carefully filtered and attenuated to reduce noise (see Ref. [50] for details).

4.2 Landau-Zener transitions

Landau-Zener-Stückelberg (LZS) transitions occur when a quantum system is driven through an energy-level avoided crossing [141, 142, 143]. The resulting quantum dynamics of the LZS mechanism [144] in driven systems [145] have been developed [146, 147] within a two-level coherent scattering formalism [148, 149, 150, 151] with potential application to quantum information science and technology [150, 151, 152, 153, 154].

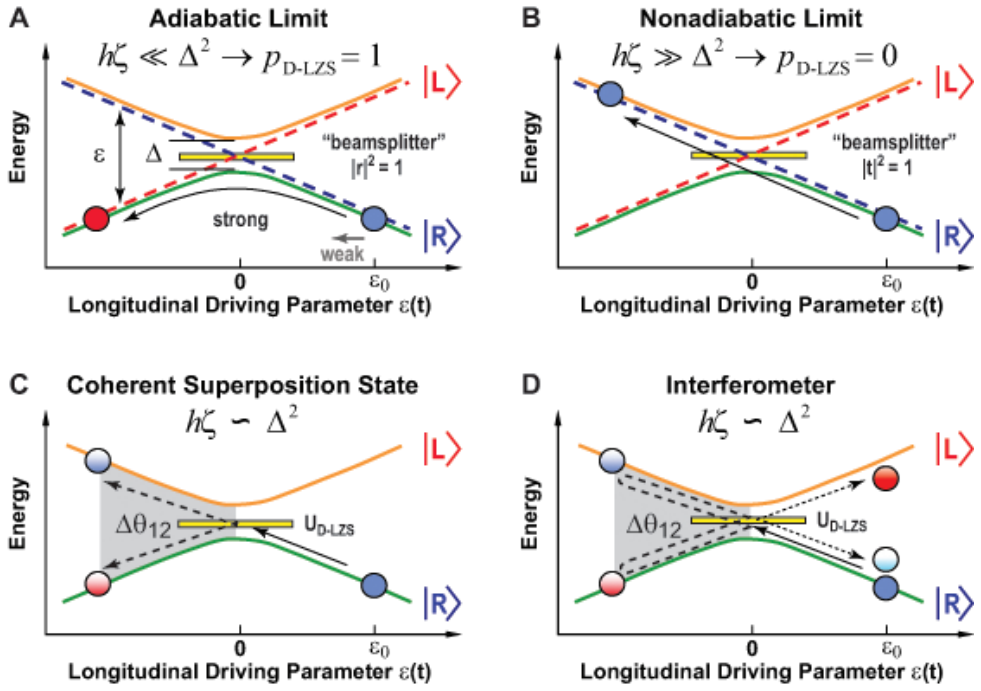

Fig. 16: Landau-Zener-Stückelberg transition. A) *Adiabatic limit: $h\zeta \ll \Delta^2$; the probability of a transition from state $|R\rangle$ to state $|L\rangle$ approaches unity.* **B)** *Nonadiabatic limit: $h\zeta \gg \Delta^2$; the probability of a transition from state $|R\rangle$ to state $|L\rangle$ approaches zero.* **C)** *Coherent superposition of states. At intermediate sweep velocities ($h\zeta \sim \Delta^2$) a superposition state $\alpha|L\rangle + \beta|R\rangle$ results from an excursion through the avoided crossing. A phase difference $\Delta\theta_{12}$ accrues due to the energy difference between the states $|L\rangle$ and $|R\rangle$.* **D)** *Quantum interference during a second excursion through the avoided crossing. Interference fringes appear at half-integer and integer values of $\Delta\theta_{12}/2\pi$, which is tunable via the drive amplitude.*

We model a LZS transition at a single crossing using the two-level Hamiltonian

$$\mathcal{H} = -\frac{1}{2}\begin{pmatrix} \varepsilon(t) & \Delta \\ \Delta & -\varepsilon(t) \end{pmatrix}, \tag{132}$$

in which ε is the energy difference between diabatic-state energy levels (dashed lines in Fig. 16A), and Δ is the size of the avoided crossing and corresponds to the coupling strength between diabatic states $|\mathrm{L}\rangle$ and $|\mathrm{R}\rangle$.

The system is prepared in state $|R\rangle$ at a static value $\varepsilon_0 \gg \Delta$ far from the avoided crossing (blue dot, Fig. 16A) and driven longitudinally from that point by making $\varepsilon(t)$ time dependent. We distinguish here between "weak driving," in which the system drive is not large enough to reach the avoided crossing, and "strong driving" for which the avoided crossing is traversed. Under strong-driving conditions, the asymptotic probability $P_{\text{D-LZS}}$ of a transition between diabatic states,

$$P_{\text{D-LZS}} \equiv 1 - P_{\text{E-LZS}} = 1 - \exp\frac{-\pi\Delta^2}{2\hbar\zeta_i}, \tag{133}$$

is governed by the relative-energy sweep rate ζ_i

$$\zeta_i = \frac{d\varepsilon(t)}{dt}|_{t=t_i} \tag{134}$$

evaluated at the time $t = t_i$ at which the system is swept through the avoided crossing. In the original LZS formulation, the system was driven with a fixed sweep rate, whereas we will later consider a harmonically driven system. We also note that we have elected to monitor the probability $P_{\text{D-LZS}}$ of a transition between the diabatic states $|L\rangle$ and $|R\rangle$, because our readout detector is sensitive to changes in diabatic state. This can be written with no loss of generality in terms of the probability $P_{\text{E-LZS}}$ of a transition between the system eigenstates.

There are two strong-driving limits characterized by the relative sizes of the sweep velocity ζ and the avoided crossing Δ. In the adiabatic limit (Fig. 16A), the sweep velocity is small ($h\zeta \ll \Delta^2$) and the probability of a transition from state $|R\rangle$ to state $|L\rangle$ approaches unity, $P_{\text{D-LZS}} \to 1$. In this case, the system dynamics are slow enough that the system adiabatically follows the ground eigenstate through the avoided crossing. In the nonadiabatic limit (Fig. 16B), the sweep velocity is large ($h\zeta \gg \Delta^2$) and the probability of a transition approaches zero $P_{\text{D-LZS}} \to 0$. In this case, the dynamics are too fast for the system to follow; the system remains in diabatic state $|R\rangle$ and, thereby, effectively jumps the energy gap at the avoided crossing.

More generally, a superposition state $\alpha|L\rangle + \beta|R\rangle$ results from an excursion through the avoided crossing, as illustrated in Fig. 16C. Following an idea discussed by Shytov *et al.* [150], the LZS transition acts as a beamsplitter for the atomic state. The amplitudes α and β are determined by a unitary transformation $U_{\text{D-LZS}}$, effectively a 2×2 "beamsplitter matrix" comprising complex reflection r and transmission t coefficients related to the adiabaticity parameter $\Delta^2/\hbar\zeta$ present in Eq. 133 [144] such that $|t|^2 = 1 - P_{\text{D-LZS}}$, $|r|^2 = P_{\text{D-LZS}}$, and $U^\dagger_{\text{D-LZS}} U_{\text{D-LZS}} = I$. Note that we have defined $|t|^2$ and $|r|^2$ from the perspective of a beamsplitter, which "transmits" ("reflects") an input state to the same (opposite) diabatic state, respectively. After the transition, a relative phase $\Delta\theta_{12}$ accrues due to the energy difference between the states $|L\rangle$ and $|R\rangle$. If the drive $\varepsilon(t)$ then returns the system through the avoided crossing a second time, the atomic state collides and quantum mechanically interferes with itself during the second LZS transition (Fig. 16D). The cumulative result is an atom-state interferometer whose output state depends on the LZS transition amplitudes and the interference phase.

An analogy can be made to a Mach-Zehnder interferometer: the atomic states play the role of the photon modes, the LZS transitions play the role of the photon beamsplitters, and the energy-level splitting, which determines the interference phase, plays the role of optical path length difference. The quantum interference is robust provided the evolution time of the state through the interferometer is short compared with the atom's coherence times. In addition to superconducting artificial atoms [38, 39, 27, 40, 41, 33], this concept is generally applicable to other solid-state artificial atoms [158, 159] and generalized spin systems [160] (e.g., molecular magnets [161, 162, 163], natural atoms [164, 165], and molecules [166, 167, 168]) that exhibit avoided level crossings, and it is extensible to multiple energy levels as we demonstrate in Section 19.

4.3 Mach-Zehnder-type interferometry

The structure of the n-photon spectroscopy peaks seen in Fig. 15E consists of regularly-spaced resonances positioned according to the condition n$\times$1.2 GHz being resonant with the energy level separation. Notably, however, for this particular value of driving amplitude, the n=1, 3, and 6 photon peaks are missing. As we describe in this section, the presence and absence of these peaks arise from Mach-Zehnder-type quantum interference at a level crossing. The interference phase can be tuned through the driving amplitude, and leads to a "Bessel staircase" in the observed spectroscopy. The interference oscillations are known as Stückelberg oscillations [143], and they have been observed in both artificial [38, 39, 40, 41] and natural [164, 165, 166] atomic systems.

In a conventional Mach-Zehnder interferometer, an optical signal is passed through two beamsplitters. The first beamsplitter coherently divides the signal into two output paths, which may have different effective optical path lengths. These paths are then recombined at the second beamsplitter, where the signal waves interfere and exit the interferometer. The measured output exhibits interference fringes depending on the relative path length.

Here, we instead utilize LZS transitions at level crossings as beamsplitters for the atomic state [150]. We drive the persistent-current qubit with a harmonic driving field of the form

$$\varepsilon(t) = \varepsilon_0 + A\sin\omega t \tag{135}$$

with $\omega = 2\pi\nu$ the driving frequency and $A > \varepsilon_0$ the field amplitude (in units of energy), which is proportional to the RF voltage at the source. As illustrated in Fig. 16D, the qubit state undergoes two LZS transitions during one period of the driving field. The first LZS transition at time t_1 splits the qubit into a superposition of excited and ground states. A relative phase $\Delta\theta_{12}$ accumulates

$$\Delta\theta_{12} = \frac{1}{\hbar}\int_{t_1}^{t_2}\varepsilon(t)dt, \quad \varepsilon(t) = \varepsilon_{|R\rangle}(t) - \varepsilon_{|L\rangle}(t) \tag{136}$$

until the second LZS transition at time t_2, at which point the qubit state collides with itself and interferes. Interference fringes appear at half-integer and integer values of $\Delta\theta_{12}/2\pi$, which is tunable via the drive amplitude.

It is clear, however, that a second phase must also play a role in this problem, since the qubit state continues to evolve for the remainder of the driving period. It is physically meaningful to consider the total phase θ accumulated over a single period:

$$\theta = \frac{1}{\hbar}\oint\varepsilon(t)dt = 2\pi\varepsilon_0/\hbar\omega, \tag{137}$$

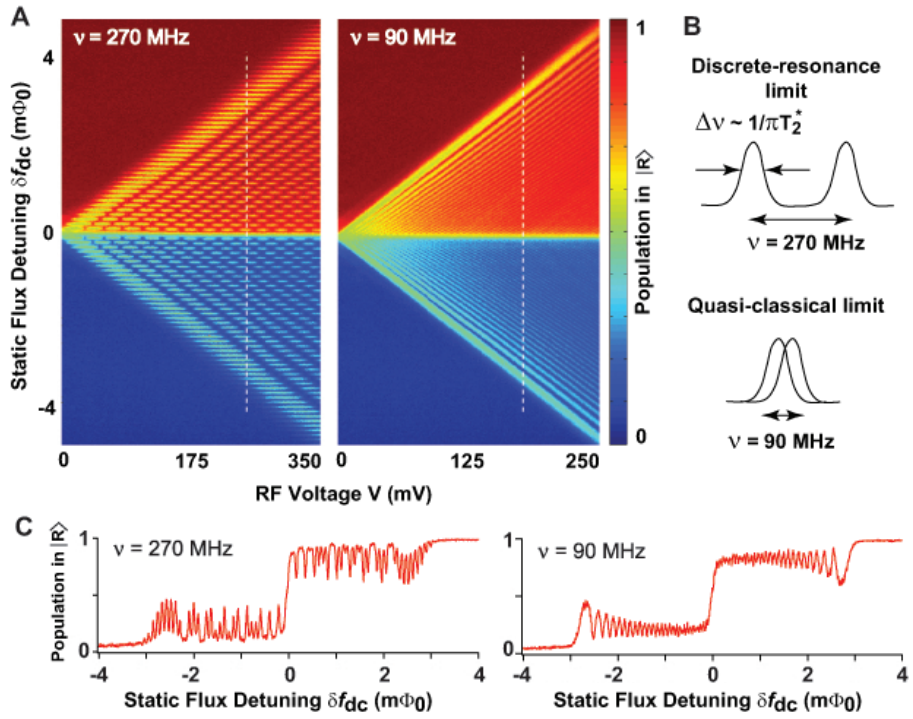

Fig. 17: Mach Zehnder interference. A) *Measured qubit population as a function of excitation amplitude and flux detuning in two excitation regimes. Left:* $\nu = 270$ *MHz. The resonance linewidth is smaller than the excitation frequency* **(B, top)***; individual n-photon resonances can be resolved and a Bessel staircase is observed. Right:* $\nu = 90$ *MHz. The resonance linewidth is larger than the excitation frequency* **(B, bottom)***; individual resonances are no longer resolved but coherent interference is still observed.* **C)** *Interference fringes in qubit population for* $\nu = 270$ *MHz (left)* $\nu = 90$ *MHz (right) along the vertical dashed lines in* **A**.

which is *independent* of the driving amplitude. Over many periods of the driving field, the cascaded pairs of LZS transitions (cascaded interferometers) will constructively interfere provided $\theta = 2\pi n$. One can view this as a "time-domain" formulation for the familiar n-photon resonance condition

$$\varepsilon_{0,n} = nh\nu \tag{138}$$

where n is the number of photons involved in the transition. It is only when the product $nh\nu$ equals the energy separation $\varepsilon_{0,n}$ that the cascaded LZS transitions lead to a net buildup of interference fringes. These oscillations are related to photoassisted transport [169, 170, 171] and Rabi oscillations [27, 33] in the multiphoton regime.

Mach-Zehnder-type interference in the discrete-resonance limit driven towards saturation is shown in Fig. 17A for driving frequency $\nu = 270$ MHz. This frequency is larger than the resonance linewidth (Fig. 17B), and so individual n-photon resonances can be resolved. There are two main features observable in this plot. The first is the presence of equally-spaced n-photon transitions as a function of flux detuning, symmetrically located about the qubit step at $\delta f_{\rm dc} = 0$. As one might expect, the onset of the higher-photon transitions requires larger driving amplitudes. Remarkably, we observe up to 50-photon transitions in this scan. The second main feature is that for each n-photon resonance, the spectroscopy appears and disappears as a function of amplitude, which sweeps the interference phase $\Delta\theta_{12}$. For example, 14 oscillation lobes are visible for the 1-photon transition. A vertical slice of the spectroscopy (dashed white line in Fig. 17A) is plotted in Fig. 17C; at this particular amplitude, one can see the enhancement and suppression of the spectroscopy peaks as was observed in Fig. 15E.

The Mach-Zehnder interference for an n-photon transition yields a modified amplitude-dependent matrix element [38, 27, 160]

$$\Delta_n = \Delta J_n(\lambda) \tag{139}$$

where $J_n(\lambda)$ is the nth-order Bessel-function, and its argument $\lambda = A/\hbar\omega$ is the dimensionless driving amplitude (see Appendix B). Intuitively, the Bessel-function dependence arises because the qubit is driven harmonically through energy levels that are linear in flux detuning and, as a result, the interference phase accumulates with a sinusoidal time dependence. The interference fringes for each n-photon resonance are related to the matrix element squared, Δ_n^2. At specific amplitudes, there is a complete destructive interference of a transition due to the zeros of $J_n(\lambda)$; this is the coherent destruction of tunneling [155, 156, 157] condition for driven n-photon transitions [38, 39].

In the discrete resonance limit, n-photon resonances are distinguishable, because the coherence time of the qubit is sufficiently longer than the driving period. By reducing the frequency to $\nu = 90$ MHz (Fig. 17A, right panel), we effectively made the drive period comparable with the linewidth, $\nu T_2^* \sim 1$ (Fig. 17B). In this spectroscopy plot, the individual n-photon resonances are no longer resolvable. However, the Mach-Zehnder interference fringes (vertical slice, Fig. 17C) are clearly visible, because the qubit remains coherent during the critical fraction of the drive period during which the phase $\Delta\theta_{12}$ accumulates and the Mach-Zehnder interference occurs. Intuitively, provided $\nu T_1 \gg 1$, the output populations of each quantum interferometer are then preserved (frozen) until the subsequent interferometer is reached in the following period; therefore, although the resonance condition is lost, the Mach-Zehnder quantum interference remains. This behavior can be contrasted with driven Rabi oscillations, for which there would be no signature of coherence in the limit $\nu T_2^* \sim 1$.

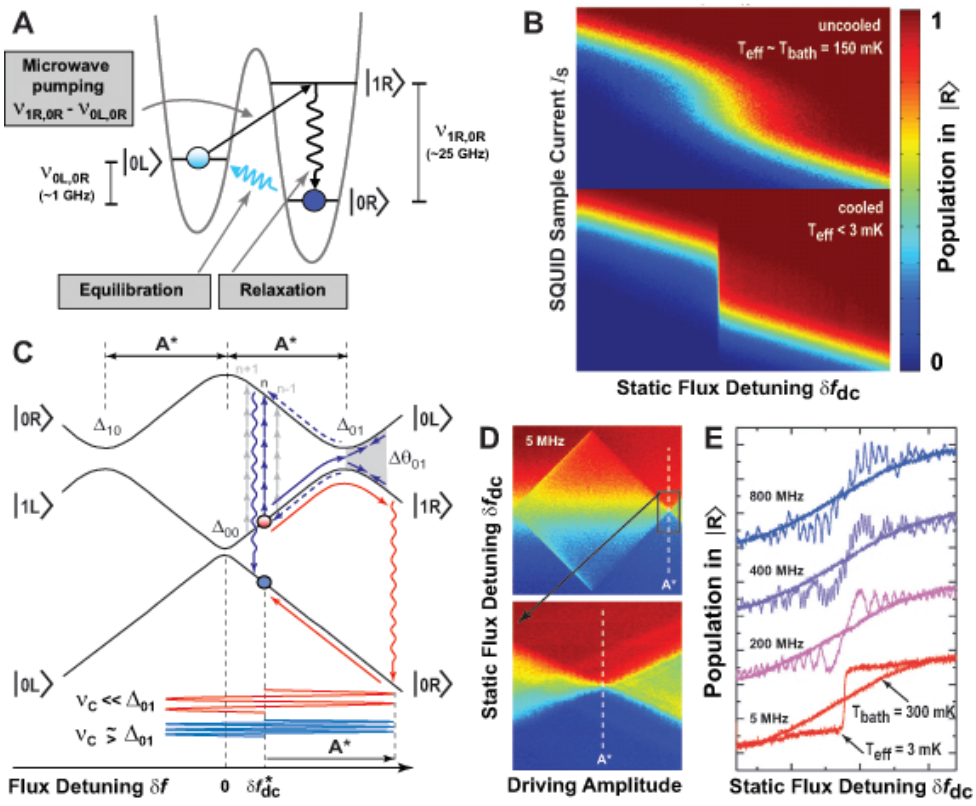

Fig. 18: Cooling of and artificial atom via an ancillary excited state. A) *External excitation transfers the thermal population from state* $|0L\rangle$ *to state* $|1R\rangle$ *(straight line) from which it decays into the ground state* $|0R\rangle$*. Wavy lines represent spontaneous relaxation and absorption leading to equilibration.* **B)** *Qubit step at* $T_{\rm bath}$ *= 150 mK in equilibrium with the bath (top) and after a 3-*μ*s cooling pulse at 5 MHz (bottom). The average level populations exhibit a qubit step about* $\delta f_{\rm dc} = 0$*, with a width proportional to* $T_{\rm bath}$ *(top) and* $T_{\rm eff} \ll T_{\rm bath}$ *(bottom).* **C)** *Schematic level diagram illustrating resonant and adiabatic cooling.* $|0L\rangle \rightarrow |1R\rangle$ *transitions are resonant at high driving frequency* ν *(blue lines) and occur via adiabatic passage at low* ν *(red lines).* Δ_{00} *and* Δ_{01} *are the tunnel splittings between* $|0R\rangle$ - $|0L\rangle$ *and* $|0L\rangle$ - $|1R\rangle$*.* **D)** *Optimal cooling parameters. State* $|0R\rangle$ *population vs. flux detuning* $\delta f_{\rm dc}$ *and driving amplitude* A *with* ν *= 5 MHz,* $\Delta t_c = 3\,\mu$s*, and* $T_{\rm bath}$*= 150 mK. Optimal conditions for cooling are realized at* $A = A^*$*, where* A^* *is defined in* **C**. **E)** *Cooling at driving frequencies* ν *= 800, 400, 200 and 5 MHz. State* $|0R\rangle$ *population vs.* $\delta f_{\rm dc}$ *for the cooled qubit and for the qubit in thermal equilibrium with the bath (black lines,* $T_{\rm bath} = 300\,$mK*). Measurements for* $\nu = 800$*, 200 and 5 MHz are displaced vertically for clarity. A cooling factor of 100, independent of detuning, is obtained in the adiabatic limit (5 MHz).*

4.4 Microwave cooling

The previous discussion involved driving transitions in the lowest two energy levels in the double-well potential of our artificial atom (Fig. 18A), which constitute the two-level qubit subsystem of a more complex energy level diagram (Fig. 19C). When higher-excited states are accessed, the driven system behavior can be markedly different from the population saturation observed when only two levels are involved. For example, at least three levels are required to achieve population inversion, and such a multi-level artificial atom coupled to a microwave cavity has been used to demonstrate masing (microwave lasing) [172]. In that work, Josephson quasi-particle states were driven to achieve inversion. Alternatively, population inversion can be established by accessing an ancilliary excited state via direct or LZS transitions. This will be briefly discussed in the next section.

Here, by reversing the cycle that leads to population inversion, we show that one can pump population from the qubit excited state $|0L\rangle$ to the qubit ground state $|0R\rangle$ (Fig. 18A) via an ancillary energy level $|1R\rangle$. In the case where the population in $|0L\rangle$ results from thermal excitation, the transfer of population to $|0R\rangle$ effectively cools the qubit by lowering its effective temperature. This kind of active cooling represents a means to initialize and reset qubits with high fidelity, key elements for quantum information science and technology. Alternatively, the pumping mechanism can be used to refrigerate environmental degrees of freedom [173], or to cool neighboring quantum systems [46, 47].

More explicitly, for a qubit in equilibrium with its environment, the population in $|0L\rangle$ that is thermally excited from $|0R\rangle$ follows the Boltzmann relation

$$p_{0L}/p_{0R} = \exp[-\varepsilon/k_{\rm B}T_{\rm bath}], \tag{140}$$

where $p_{0L,0R}$ are the qubit populations for energy levels $\varepsilon_{0L,0R}$, $\varepsilon = \varepsilon_{0L} - \varepsilon_{0R}$, $k_{\rm B}$ is the Boltzmann constant, and $T_{\rm bath}$ is the bath temperature. To cool the qubit subsystem below $T_{\rm bath}$, a microwave magnetic flux of amplitude A and frequency ν targets the $|0L\rangle \rightarrow |1R\rangle$ transition, driving the state-$|0L\rangle$ thermal population to state $|1R\rangle$, from which it quickly relaxes to the ground state $|0R\rangle$. Efficient cooling only occurs when the driving-induced population transfer to $|0R\rangle$ is faster than the thermal repopulation of $|0L\rangle$. The hierarchy of relaxation and absorption rates required, $\Gamma_{0R,1R} \gg \Gamma_{0L,1R}, \Gamma_{0L,0R}$, is achieved in our system owing to a relatively weak tunneling between wells, which inhibits the interwell relaxation and absorption processes $|1R\rangle \rightarrow |0L\rangle$ and $|0R\rangle \rightarrow |0L\rangle$, compared with the relatively strong intrawell relaxation process $|1R\rangle \rightarrow |0R\rangle$.

Figure 18B shows the qubit step at $T_{\rm bath}$ = 150 mK in equilibrium with the bath (top) and after a 3-μs cooling pulse at 5 MHz (bottom). Under equilibrium conditions, the average level populations exhibit a thermally-broadened qubit step about $\delta f_{\rm dc} = 0$, with a width proportional to $T_{\rm bath}$. The presence of microwave excitation targeting the $|0L\rangle \rightarrow |1R\rangle$ transition acts to increase the ground-state population and, thereby, sharpens the qubit step. Cooling can thus be quantified in terms of an effective temperature $T_{\rm eff} < T_{\rm bath}$, a signature that is evident from the narrowing of the qubit steps in Fig. 18B after cooling. More precisely, using the notation from Fig. 16, the effective qubit temperature is obtained by fitting an effective temperature that would have been required in equilibrium to achieve the observed qubit population p_{0R},

$$p_{0R} = \frac{\varepsilon}{\sqrt{\varepsilon^2+\Delta^2}}\left[\tanh\left(\frac{\sqrt{\varepsilon^2+\Delta^2}}{2k_{\rm B}T_{\rm eff}}\right)+1\right]. \tag{141}$$

Universal cooling (cooling that is independent of flux detuning) occurs near an optimal driving amplitude A^* (Fig. 18C). This is demonstrated in Fig. 18D where we present the $|0R\rangle$ state population $P_{\rm sw}$ measured as a function of the microwave amplitude A and flux detuning $\delta f_{\rm dc}$ for $\nu = 5\,{\rm MHz}$. Cooling and the diamond feature can be understood in terms of the energy level diagram (Fig. 19C). As the amplitude of the microwave pulse is increased from $V = 0$, population transfer first occurs when the $\Delta_{0,0}$ avoided crossing is reached, *i.e.* $A > |\delta f_{\rm dc}|$; this defines the front side of the observed diamond symmetric about the qubit step (see also Fig. 17A). For amplitudes $A^*/2 \leq A \leq A^*$, the $\Delta_{0,1}$ ($\Delta_{1,0}$) side avoided crossing dominates the dynamics, resulting in a second pair of thresholds $A = A^* - |\delta f_{\rm dc}|$, which define the back side of the diamond. In the region outside of the diamond's backside, the qubit is cooled. As the diamond narrows to the point $A = A^*$, the narrowest qubit step is observed. This is the universal cooling condition: only one of the two side avoided crossings ($\Delta_{0,1}$ or $\Delta_{1,0}$) is reached and, thereby, strong transitions with relaxation to the ground state result for all $\delta f_{\rm dc}$. In contrast, for $A > A^*$, both side avoided crossings ($\Delta_{0,1}$ and $\Delta_{1,0}$) are reached simultaneously for $|\delta f_{\rm dc}| < A - A^*$, leading once again to a large population transfer between $|0R\rangle$ and $|0L\rangle$, and opening the second diamond feature (see Fig. 19).

The cooling exhibits a rich structure as a function of driving frequency and detuning, resulting from the manner in which state $|1R\rangle$ is accessed (Fig. 18C). Transitions occur via a (multiphoton) resonant or adiabatic passage process when the driving frequency is high or low enough, respectively [39, 44]. At high frequencies (800 and 400 MHz in Fig. 18E) well-resolved resonances of n-photon transitions are observed and cooling is thus maximized near resonances. At intermediate frequencies (400 and 200 MHz), Mach-Zehnder interference at the side avoided crossing Δ_{01} becomes more prominent and modulates the intensity of the n-photon resonances [38, 39]. Below $\nu = 200\,{\rm MHz}$, individual resonances are no longer discernible, but as in Fig. 17C, the modulation envelope persists [39]. At the lowest frequencies ($\nu < 10\,{\rm MHz}$), state $|1R\rangle$ is reached via adiabatic passage through the Δ_{01} crossing (Fig. 18C), and the population transfer and cooling become conveniently independent of detuning (see $\nu = 5$ MHz in Fig. 19E). As shown in Fig. 18E, we achieve an effective qubit temperature $T_{\rm eff}$ = 3 mK, even for $T_{\rm bath}$ = 300 mK. In our qubit, our determination of $T_{\rm eff}$ was limited primarily by decoherence (linewidth), which limited the resolution with which we could distinguish the states $|0R\rangle$ and $|0L\rangle$ near degeneracy. Nonetheless, we can estimate the ideally resolvable cooling factor $\alpha_{\rm c}$ for this type of cooling process using Eq. 140,

$$\alpha_{\rm c} \sim \frac{T_{\rm bath}}{T_{\rm eff}} = \frac{\varepsilon_{1R\rightarrow 0R}}{\Delta}, \tag{142}$$

where $\varepsilon_{1R\rightarrow 0R} \approx h \times 25$ GHz is the energy separation where the relaxation $|1R\rangle \rightarrow |0R\rangle$ occurs and $\Delta \approx h \times 0.01$ GHz for our qubit, yielding a cooling factor $\alpha_{\rm c} \sim 2500$. For a bath temperature $T_{\rm bath} = 50$ mK, this would correspond to an effective temperature $T_{\rm eff} = 20\ \mu$K in our qubit. Using this approach, in principle, lower temperatures can be resolved in systems with smaller energy gaps.

Cooling a qubit in equilibrium with the bath requires a characteristic cooling time. In turn, a cooled qubit will thermalize to the environmental bath temperature over a characteristic equilibration time. The relationship between these two times determines if it is possible to drive the qubit while it is still cold. We found in this qubit that equilibration times are at least one order of magnitude larger than cooling times at $T_{\rm bath} < 250$ mK and up to three order of magnitude larger at $T_{\rm bath} < 100$ mK [44]. This allowed us ample time to drive the qubit after cooling it. The implementation of an active cooling pulse prior to a generic driving pulse is

highly advantageous. On the one hand, it sensibly shortens measurement times, enabling us to acquire data at repetition rates that far exceed the intrinsic equilibration rate due to interwell relaxation after each measurement trial. By adopting active cooling, we gained a factor 50 in data acquisition speed, limited by the bandwidth of our readout circuit. On the other hand, by analogy to the cooling of trapped ions and atoms, active cooling greatly reduces thermal smearing, allowing us to analyze features in the data that would have been hidden otherwise. This type of active cooling protocol was required to obtain the detailed, clean data in Fig. 17. In fact, the necessity of active cooling becomes even more evident in the next section where, without the cooling pulse, the observed level of detail could not have been resolved over such a large parameter space in practical acquisition times.

4.5 Amplitude spectroscopy

Since Newton's dispersion of light into a continuous color "spectrum," spectroscopy has been viewed primarily as a frequency-based technique. Ångström, Bunsen, Foucault, Kirchhoff, and many others identified unique spectral lines for elements and compounds based on the emission and absorption of radiation at various frequencies. The series of spectral lines of hydrogen are named for Balmer and Rydberg, who observed them within and beyond the visible wavelengths. Such frequency-dependent absorption and emission spectroscopy played a fundamental role in the development of quantum mechanics and the "new" atomic theory by identifying discrete energy levels. With the invention of coherent microwave (maser) and optical (laser) sources, high-intensity radiation with tunable, narrow spectral linewidth allowed targeted absorption spectroscopy of atoms and molecules with high frequency resolution [174, 175].

However, the application of broadband frequency spectroscopy is not universally straightforward. This is particularly relevant for artificial atoms engineered from solid-state materials which, when cooled to cryogenic temperatures, assume quantized energy levels that extend into microwave and millimeter wave regimes (10-300 GHz). Although certainly not an impossible task, a broadband frequency-based spectroscopic study of these atoms in excess of around 50 GHz becomes extremely challenging and expensive to implement due to numerous frequency-dependent effects (*e.g.*, frequency dispersion and the requisite tolerances to control impedance).

Amplitude spectroscopy is an alternative approach to broadband spectroscopic characterization of a quantum system. With amplitude spectroscopy, spectroscopic information is obtained from the system response to driving-field amplitude at a *fixed* frequency. The resulting spectroscopic interference patterns, "spectroscopy diamonds," are mediated by multilevel LZS transitions and Mach-Zehnder-type interferometry, and they serve as a fingerprint of the artificial atom's multilevel energy spectrum. The energy spectrum is then determined by analyzing the atomic fingerprint. In this way, the amplitude spectroscopy technique complements frequency spectroscopy: although a less direct approach, it allows one to probe the energy level structure of a quantum system over extraordinarily large (even practically prohibitive) bandwidths by circumventing many of the challenges associated with a frequency-based approach.

In general, the spectroscopy diamonds arise due to an interplay between the static flux detuning $\delta f_{\rm dc}$ and driving amplitude V. As described in Sections 4.2 and 4.3, transitions occur when an avoided crossing is reached for a particular set of values ($\delta f_{\rm dc}$,V). For example, at a flux detuning $\delta f_{\rm dc}^*$, the diamond boundaries occur at $V = V_1, V_2, V_3$.... (Fig. 19 A and C). The Mach-Zehnder interference due to a phase accumulation $\Delta\theta_{q,q'}$ at a given avoided crossing $\Delta_{q,q'}$ can be modulated by varying both $\delta f_{\rm dc}$ and V.

There are two important contributions to the diamond spectroscopy patterns: LZS-mediated

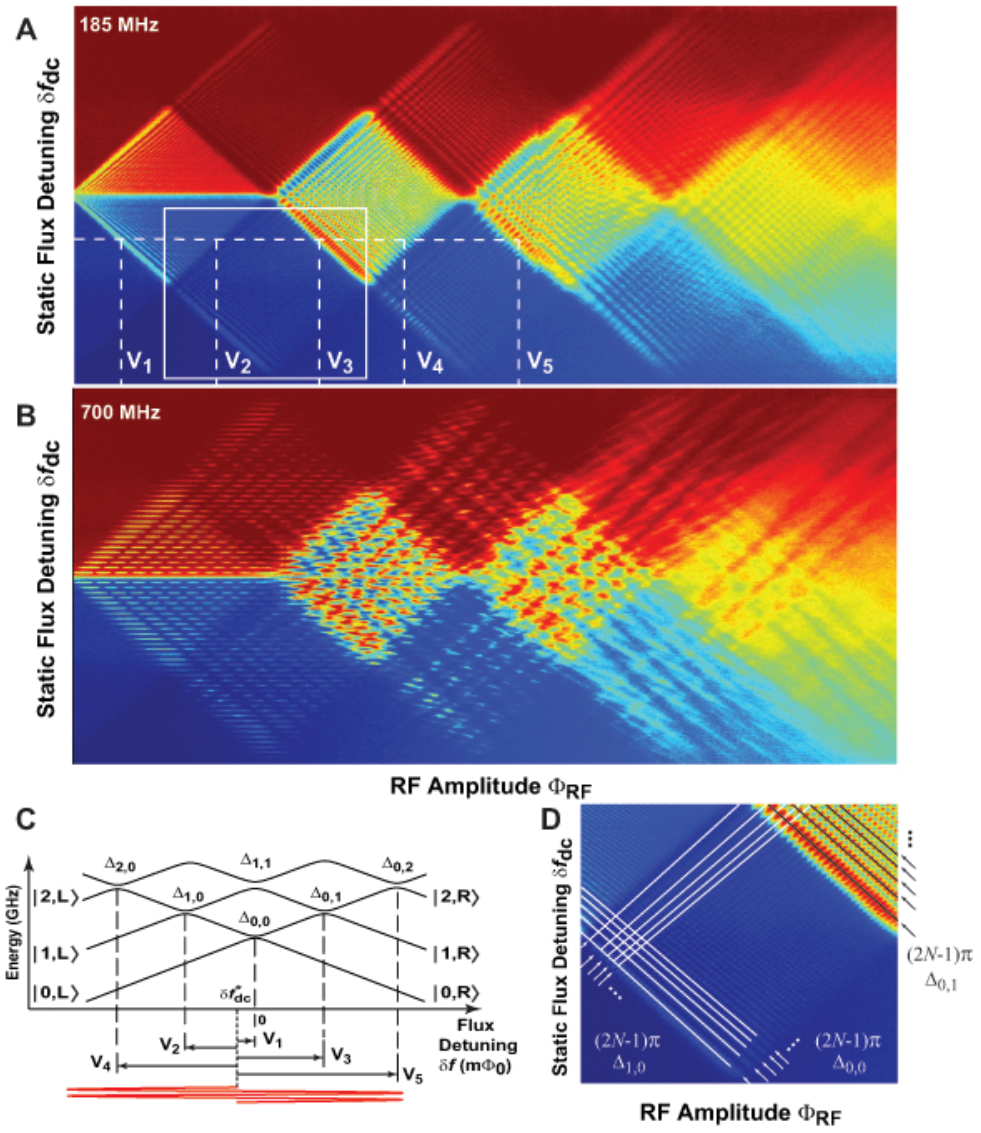

Fig. 19: *Amplitude spectroscopy with long-pulse driving towards saturation. Spectroscopy diamonds obtained at driving frequencies $\nu = 185$ MHz (A) and $\nu = 700$ MHz (B). The color scale represents the net qubit population in state $|q, R\rangle$, where R (L) labels diabatic states of the right (left) well of the qubit double-well potential, and $q = 0, 1, 2, ...$ labels the longitudinal modes. The excitation amplitude V is swept for each static flux detuning $\delta f_{\rm dc}$. The diamond edges mark the driving amplitude V for each value of $\delta f_{\rm dc}$ when an avoided level crossing is first reached (amplitudes $V_1 - V_5$ for $\delta f_{\rm dc} = \delta f_{\rm dc}^*$). C Schematic energy-level diagram illustrating the relation between V and the avoided crossing positions for $\delta f_{\rm dc} = \delta f_{\rm dc}^*$. The arrows represent the amplitudes $V_1 - V_5$ in A. (D) Zoom in of 185-MHz interference patterns (box region, Fig. 19A). The arrows point to lines of constant phase $(2N - 1)\pi$ along which LZS transitions are likely to occur for the avoided crossings $\Delta_{0,0}$, $\Delta_{0,1}$, and $\Delta_{1,0}$.*

transitions and intrawell relaxation. In Fig. 19D, we show a subset of the diamond interference pattern in Fig. 19A. Arrows indicate lines of constant phase accumulation $\Delta\theta_{q,q'} = (2N-1)\pi$ in ($\delta f_{\rm dc}$,V)-space that leads to LZS transitions at each of the three listed avoided crossings, $\Delta_{0,0}$, $\Delta_{0,1}$, and $\Delta_{1,0}$. Where these lines cross, competition (coordination) between avoided crossings act to suppress (enhance) the net transition rate between pairs of energy levels. These crossing lines are the reason for the checkerboard patterns observed inside and outside the diamonds.

The second contribution, intrawell relaxation, provides another means to connect energy levels and results in both cooling and population inversion. In Section 4.4, Fig. 18C, $\Delta_{0,1}$ mediated the transition $|0L\rangle \rightarrow |1R\rangle$, and intrawell relaxation then mediated the transition $|1R\rangle \rightarrow |0R\rangle$; the net result was cooling, since the flux $\delta f_{\rm dc}$ was positive, making $|0R\rangle$ the ground state. However, in Fig. 19D $\delta f_{\rm dc}$ is negative. Furthermore, in the upper-right corner of Fig. 19D, both crossings $\Delta_{0,1}$ and $\Delta_{1,0}$ are accessed. In the bright red regions, $\Delta_{0,1}$ still tends to cause transitions $|0L\rangle \rightarrow |1R\rangle$, and relaxation puts that population in state $|0R\rangle$. However, the interference condition at $\Delta_{1,0}$ on the other side of the energy level diagram (Fig. 19C) tends to keep the population in $|0R\rangle$. Therefore, population builds in state $|0R\rangle$, the first excited state for negative flux detuning, resulting in strong population inversion. Varying the interference conditions at $\Delta_{0,1}$ and $\Delta_{1,0}$ by changing ($\delta f_{\rm dc}$,V) causes the observed modulation between population inversion and cooling.

We have developed several techniques for extracting information about the energy levels from the spectroscopy interference patterns [50, 51]. The key metrics are the positions of the avoided crossings in flux, the values of the splittings $\Delta_{q,q'}$, and the slopes of the energy levels. With this information, one can reconstruct a large portion of the energy level diagram.

The positions of the avoided crossings can be determined precisely from the diamond boundaries, because the onset of each diamond is associated with LZS transitions at a particular level crossing. The splitting of each avoided crossing can be obtained essentially by fitting the LZS formula in Eq. 133 to the Mach-Zehnder interference patterns. Alternatively, one can study the dynamical population transfer between states using the pulsed, short-time implementation of amplitude spectroscopy [50].

The energy level slopes can be determined by two means. The first is by relating the separation between interference nodes to the expected phase accumulation $\Delta\theta_{12}$, since the phase accumulation depends sensitively on the energy-level slope. Alternatively, we show with Rudner *et al.* in Ref. [51] that the two-dimensional Fourier transform of the diamond patterns yields a family of *one-dimensional* sinusoids in Fourier space; the periods of these sinusoids are related to the energy-level slopes. The intuition is that the Fourier transform inverts the energy domain of the spectroscopy to the time domain (scaled by $\hbar$). This means that the sinusoids in Fourier space image the time-dependence of the quantum phase of the qubit, which, in turn, depends sensitively on the energy-level slopes.

Using amplitude spectroscopy, we were able to scan the energy level diagram continuously beyond the fourth energy-level avoided crossing ($\Delta_{0,0} \ldots \Delta_{0,4}$, $\Delta_{4,0}$) with splitting values ranging from $\Delta_{0,0} \approx 0.01$ GHz to $\Delta_{0,4}, \Delta_{4,0} \approx 2.2$ GHz [50]. The equivalent information obtained using frequency spectroscopy would have required scanning frequencies from 0.01 GHz out to beyond 100 GHz (each avoided crossing is separated by approximately 25 GHz). Remarkably, with amplitude spectroscopy, the entire scan performed in Fig. 19A was performed at a fixed frequency $\nu = 185$ MHz. The scan in Fig. 19B shows the amplitude spectroscopy of the same system for a fixed frequency $\nu = 700$ MHz, clearly in the discrete resonance limit. The resonance condition adds another constraint, making a more complex and interesting checkerboard pattern.

4.6 Summary and applications

Strongly driving a superconducting artificial atom through an avoided level crossing results in a Landau-Zener-Stückelberg transition, which, in general, creates a superposition of atomic states whose weighting depends on the size of the avoided crossing and the velocity with which it is traversed. In this sense, as we discussed in Section 4.2, the LZS mechanism acts as a beamsplitter for artificial atoms.

In Section 4.3, we described how harmonically driving the system cascades two LZS transitions per driving period, resulting in an atomic analog to a Mach-Zehnder interferometer. The relative phase acquired between LZS transitions is the interference phase of the interferometer, and it is tunable by the driving amplitude. The buildup of population over many driving periods exhibits Stückelberg oscillations as a function of the driving amplitude (interference phase) due to the cascaded Mach-Zehnder-type interference effect. To observe these oscillations, the coherence time must only be longer than the small portion of the drive period when the interference phase accrues, and the relaxation time must be long enough to maintain the population until readout.

The total phase accumulated over one period, in contrast, is amplitude independent. For coherence times longer than the drive period, cascaded interferometers yield a net population change when this round-trip phase accumulation is $2\pi n$ per driving period, a condition which can be viewed as the "time-domain" counterpart to the n-photon resonance condition $nh\nu = \varepsilon_{0,n}$. By making the drive period commensurate with the coherence time, we showed that we could still observe the Stückelberg oscillations, even though the discrete resonances were no longer discernable.

We utilized strong driving and the LZS mechanism with higher-energy levels to achieve both cooling and population inversion in our artificial atom. In Section 4.4, we described using a microwave pumping scheme to cool the atomic degrees of freedom a factor 10-100 times colder than the ambient dilution refrigerator temperature. The scheme involved pumping unwanted thermal population to an ancillary excited state, from which it relaxed to the ground state. In Section 4.5, we showed that by reversing the order, we could pump population through an ancillary state to achieve inversion.

The energy level structure can be probed over extraordinarily large bandwidth using amplitude spectroscopy in Section 4.5. Since the LZS mechanism and Mach-Zehnder interference are sensitive to the defining features in the energy level diagram (energy band slopes, level splittings, and their locations), the interference patterns that result from sweeping the amplitude are a "fingerprint" of the artificial atom's energy spectrum. Using amplitude spectroscopy at a fixed driving frequency of only 185 MHz, we could access continuously multiple energy levels from about 10 MHz out to beyond 120 GHz.

Large-amplitude driving and the LZS mechanism have application to quantum information science and technology. Active cooling has utility as an "entropy pump" in state initialization and refreshing ancilla qubits in quantum error correction protocols. Amplitude spectroscopy provides an means to ascertain over large bandwidth the energy level structure of a qubit system beyond the lowest two levels. The Mach-Zehnder-type interference can facilitate nonadiabatic control schemes, in which the quantum interference at an avoided crossing is used to achieve state transitions that approach the intrinsic coupling rate Δ. In cold atoms and molecules, this kind of non-adiabatic control has been used to drive transitions that would otherwise be challenging to realize in a weak-driving limit. In addition, this type of non-adiabatic detuning is widely used for the implementation of single-qubit Z gates (phase

gates) and coupled-qubit controlled-phase gates based on changing the energy-level separation of qubit states (although not generally involving Mach-Zehnder-type interference).

5 Acknowledgements

I wish to thank Simon Gustavsson, Jamie Kerman, and Terry Orlando for a careful reading of this manuscript. I also wish to acknowledge David Berns, Jonas Bylander, Janice Lee, Leonya Levitov, Yasunobu Nakamura, Mark Rudner, Sergio Valenzuela, Tsuyoshi Yamamoto, Fei Yan, Fumiki Yoshihara, and my other co-workers at MIT and Lincoln Laboratory for numerous discussions and collaborative works that have led to this manuscript.

Appendices

A Quantum conjugate operators $\hat{n}$ and $\hat{\phi}$

The correspondence between classical and quantum variables and their dynamics has been discussed in detail elsewhere Ref. [195, 196]. In this Appendix, we present several derivatives of those works that are relavent to the present discussion.

The general prescription is to start with a classical representation of the circuit using circuit network theory. This generally comprises a network of branches and nodes. One chooses either the branch or node variables, and proceeds to derive the classical Hamiltonian. For example, the sum of the branch energies in terms of the branch variables will yield the classical Hamiltonian. Alternatively, one can determine the Lagrangian of the classical circuit to obtain its classical equations of motion, and then proceed to derive the classical Hamiltonian. In either case, the classically conjugate variables satisfying a Poisson bracket equation are "transitioned" via the correspondence principle to quantum operators satisfying a quantum commutation relation.

For our purposes here, we take the number of Cooper pairs $\hat{n}$ and the Josephson phase $\hat{\phi}$ as the quantum operators [197]:

$$\hat{n}|n\rangle = n|n\rangle \tag{143}$$

$$\hat{\phi}|\phi\rangle = \phi|\phi\rangle \tag{144}$$

$$[\hat{\phi}, \hat{n}] = i. \tag{145}$$

As conjugate operators, their eigenstates are related through the Fourier transforms,

$$|\, n\rangle = \frac{1}{\sqrt{2\pi}} \int_0^{2\pi} d\phi \; e^{-i\hat{n}\phi} |\phi\rangle \tag{146}$$

$$|\, \phi\rangle = \frac{1}{\sqrt{2\pi}} \sum_n \; e^{in\hat{\phi}} |n\rangle. \tag{147}$$

The number operator $\hat{n}$ and the phase operator $\hat{\phi}$ are then expressed in their respective conjugate spaces via the relations

$$\hat{n}|\phi\rangle = |\phi\rangle \frac{1}{i} \frac{\partial}{\partial \phi} \langle\phi| \tag{148}$$

$$\hat{\phi}|n\rangle = |n\rangle i \frac{\partial}{\partial n} \langle n|. \tag{149}$$

Translation of the number and phase is represented by the following relations,

$$e^{in_0\hat{\phi}}|n\rangle = |n + n_0\rangle \tag{150}$$

$$e^{-i\hat{n}\phi_0}|\phi\rangle = |\phi - \phi_0\rangle \tag{151}$$

Based on these relations, we can make the following equivalence:

$$\cos\hat{\phi} = \frac{1}{2}\left(e^{i\hat{\phi}} + e^{-i\hat{\phi}}\right) \tag{152}$$

$$= \frac{1}{2}\sum_n |n+1\rangle\langle n| + |n-1\rangle\langle n| \tag{153}$$

$$= \frac{1}{2}\sum_n |n+1\rangle\langle n| + |n\rangle\langle n+1| \tag{154}$$

B Two-level system Hamiltonian in the strong driving limit

The two-level-system dynamics in the strong driving regime can be obtained by moving to a non-uniformly rotating frame with sinusoidal rotation frequency. One then rotates a second time to make a resonance approximation.

Applying a classical RF field of amplitude A, the Hamiltonian is

$$\mathcal{H} = -\frac{1}{2}\begin{pmatrix} \varepsilon + A\cos\omega t & \Delta \\ \Delta & -\varepsilon - A\cos\omega t \end{pmatrix}. \tag{155}$$

We use $\cos\omega t$ rather than $\sin\omega t$ for pedagogical reasons only. We are interested in the general case which includes the strongly driven regime, $|a| \geq \hbar\omega$ and $|a| \geq \varepsilon, \Delta$. Defining the transformation,

$$R_z(\Theta) = \exp\left[-i\frac{\sigma_z}{2}\Theta\right] \tag{156}$$

$$\tilde{\mathcal{H}} \equiv R_z(\Theta)\mathcal{H}R_z(-\Theta) + \frac{\sigma_z}{2}\hbar\Omega(t) \tag{157}$$

$$\Omega(t) = \frac{A}{\hbar}\cos(\omega t) \tag{158}$$

$$\Theta = \int_0^t dt'\Omega(t') = \frac{A}{\hbar\omega}\sin\omega t \equiv -\lambda\sin\omega t \tag{159}$$

where $\lambda = A/\hbar\omega$ is a dimensionless scaling of the RF amplitude to the drive frequency, we can obtain the form for the rotated Hamiltonian,

$$\tilde{\mathcal{H}} = -\frac{1}{2}\begin{pmatrix} \varepsilon & e^{-i\Theta}\Delta \\ e^{i\Theta}\Delta & -\varepsilon \end{pmatrix} = -\frac{1}{2}\begin{pmatrix} \varepsilon & e^{-i\lambda\sin\omega t}\Delta \\ e^{i\lambda\sin\omega t}\Delta & -\varepsilon \end{pmatrix}. \tag{160}$$

The generating function for the Bessel functions of the first kind of order n is:

$$e^{x(t-1/t)/2} = \sum_{n=-\infty}^{\infty} J_n(x)t^n \tag{161}$$

Identifying $t \equiv \exp(-i\omega t)$ and $x \equiv \lambda$, one obtains the off-diagonal factor:

$$\Delta e^{-i\lambda \sin \omega t} = \sum_{n=-\infty}^{\infty} \Delta J_n(\lambda) e^{i\omega n t} \tag{162}$$

$$\equiv \sum_{n=-\infty}^{\infty} \Delta_n e^{i\omega n t} \tag{163}$$

$$\Delta_n = \Delta J_n(\lambda) \tag{164}$$

$$\tilde{\mathcal{H}} = -\frac{1}{2} \begin{pmatrix} \varepsilon & \sum_{n=-\infty}^{\infty} \Delta_n e^{i\omega n t} \\ \sum_{n=-\infty}^{\infty} \Delta_n e^{-i\omega n t} & -\varepsilon \end{pmatrix}. \tag{165}$$

For flux biases $n\hbar\omega \approx \varepsilon$, only the n^{th} Fourier harmonic of the off-diagonal term dominates. This is effectively a resonance approximation. In its current form, all off-diagonal terms oscillate (rotate) at a large frequency compared with the present rotating frame. By rotating at one of the Fourier harmonic frequencies, $\Omega' = n\omega$, one reduces the Hamiltonian to

$$\tilde{\mathcal{H}}_n = -\frac{1}{2} \begin{pmatrix} \varepsilon - \hbar n\omega & \sum_{m=-\infty}^{\infty} \Delta_m e^{i\omega(m-n)t} \\ \sum_{m=-\infty}^{\infty} \Delta_m e^{-i\omega(m-n)t} & -(\varepsilon - \hbar n\omega) \end{pmatrix}, \tag{166}$$

in which only $m = n$ term will exist within the resonance approximation. It is in this limit that the diagonal energy terms are small compared with the coupling. Defining $\varepsilon_n \equiv \varepsilon - \hbar n\omega$, one obtains in the resonance approximation,

$$\tilde{\mathcal{H}}_n = -\frac{1}{2} \begin{pmatrix} \varepsilon_n & \Delta_n \\ \Delta_n & -\varepsilon_n \end{pmatrix}. \tag{167}$$

C Summary of noise spectroscopy during free- and driven-evolution

	Free-evolution decoherence	**Driven-evolution Decoherence**
Working frame	Qubit frame	Rotating frame
Quantization axis	z'-axis	X-axis
Nutation freq.	level splitting $\nu_{\rm q}$	Rabi frequency $\nu_{\rm R}$
	Longitudinal relaxation	
Method	Inversion recovery [30, 187]	Spin locking - $T_{1\rho}$ [7, 186]
Process	$T_1\ (=1/\Gamma_1)$	$T_{1\rho}\ (=1/\Gamma_{1\rho})$
Longitudinal decay	z'-axis	X-axis
Starting state	$\vert+z'\rangle$	$\vert\pm X\rangle$
Steady state	$\vert-z'\rangle$	$\vert\langle\hat{\sigma}_X\rangle=0\rangle$
Decay rate	Γ_1 (exponential)	$\Gamma_{1\rho}$ (exponential)
Decay law	$\exp\{-\Gamma_1\tau\}, \Gamma_1=\frac{1}{2}\,S_{x'}(\nu_{\rm q})$	$\exp\{-(\frac{1}{2}\,\Gamma_1+\Gamma_\nu)\tau\}, \Gamma_\nu=\frac{1}{2}\,S_{z'}(\nu_{\rm R})$
Noise susceptibility		
• in general	$S_{\perp z'}(\nu_{\rm q})$	$S_{\perp X}(\nu_{\rm R})$
• flux qubit	$S_{x'}(\nu_{\rm q})$	$S_{x'}(\nu_{\rm q}\pm\nu_{\rm R}\approx\nu_{\rm q}),\ S_{z'}(\nu_{\rm R})$
Noise of interest	$S_{x'}(\nu_{\rm q})$	$S_{z'}(\nu_{\rm R})$
	Transverse decoherence	
Method	FID [30, 8], CPMG [11]	Rabi [11, 188], Rotary echo [140]
Process	$T_2\ (=1/\Gamma_2)$	$T_{2\rho}\ (=1/\Gamma_{2\rho})$
Transverse decay	$x'-y'$ plane	$Y-Z$ plane
Starting state	e.g., $\vert\pm x', \pm y'\rangle$	$\vert-Z\rangle$ (= $\vert-z'\rangle$)
Steady state	$\vert\langle\hat{\sigma}_{x',y'}\rangle=0\rangle$	$\vert\langle\hat{\sigma}_{Y,Z}\rangle\approx0\rangle$
Decay rate		
• Bloch-Redfield	$\Gamma_2=\frac{1}{2}\,\Gamma_1+\Gamma_\varphi$ (exp.)	$\Gamma_{2\rho}=\frac{1}{2}\,\Gamma_{1\rho}+\Gamma_{\varphi\rho}$ (exp.)
• $1/f$-type noise	exp.×Gaussian (linear)	exp.×Gaussian×algebraic (quadratic)
Decay law (FID/Rabi)	$\exp\{-\frac{1}{2}\,\Gamma_1\tau-\frac{1}{2}\,\langle\delta\nu^2\rangle\tau^2\}$ $\times\cos(2\pi\Delta\nu\tau)$	$\exp\{-(\frac{3}{4}\,\Gamma_1+\frac{1}{2}\,\Gamma_\nu)\tau-\frac{1}{2}\,\langle\delta\nu_{\rm R}^2\rangle\tau^2\}$ $\times[1+(\frac{\langle\delta\nu^2\rangle}{\nu_{\rm R}}\tau)^2]^{-1/4}\cos(2\pi\nu_{\rm R}\tau)$
Noise susceptibility		
• in general	Γ_1: $S_{\perp z'}(\nu_{\rm q})$; Γ_φ: $\Delta\nu$ inhom.	$\Gamma_{1\rho}$: $S_{\perp X}(\nu_{\rm R})$; $\Gamma_{\varphi\rho}$: $\nu'_{\rm R}$ inhom.
• flux qubit	Γ_1: $S_{x'}(\nu_{\rm q})$; Γ_φ: $\Delta\nu$ inhom.	$\Gamma_{1\rho}$: $S_{x'}(\nu_{\rm q}\pm\nu_{\rm R}\approx\nu_{\rm q})$, $S_{z'}(\nu_{\rm R})$; $\Gamma_{\varphi\rho}$: $S_{x'}(\nu_{\rm q})$, $\nu_{\rm R}$ and $\Delta\nu$ inhom.
Noise of interest	$\langle\delta\nu^2\rangle$	$\Gamma_\nu=\frac{1}{2}\,S_{z'}(\nu_{\rm R})$

Table 3: *Comparison of decohering properties of a superconducting flux qubit during free evolution and driven evolution (weak and resonant driving).*

References

[1] J. Clarke and F.K. Wilhelm, Superconducting quantum bits, Nature **453**, 1031-1042 (2008).

[2] D.P. DiVincenzo, "Quantum computation," Science **270**, 255-261 (1995).

[3] Y. Nakamura, Y.A. Pashkin, J.S. Tsai, Coherent control of macroscopic quantum states in a single-Cooper-pair box, Nature **398**, 786-788 (1999).

[4] D. Vion, A. Aassime, A. Cottet, P. Joyez, H. Pothier, C. Urbina, D. Esteve, and M. H. Devoret, Manipulating the quantum state of an electrical circuit, Science **296**, 886-889 (2002).

[5] G. Burkard, R.H. Koch, D.P. DiVincenzo, Multi-level quantum description of decoherence in superconducting flux qubits, Phys. Rev. B **69**, 064503 (2004).

[6] P. Bertet, I. Chiorescu, G. Burkard, K. Semba, C.J.P.M. Harmans, D.P. DiVincenzo, J.E. Mooij, Dephasing of a superconducting qubit induced by photon noise, Phys. Rev. Lett. **95**, 257002 (2005).

[7] G. Ithier, E. Collin, P. Joyez, P.J. Meeson, D. Vion, D. Esteve, F. Chiarello, A. Shnirman, Y. Makhlin, J. Schriefl, G. Schön, Decoherence in a superconducting quantum bit circuit, *Phys. Rev. B* **72**, 134519 (2005).

[8] F. Yoshihara, K. Harrabi, A.O. Niskanen, Y. Nakamura, and J.S. Tsai, Decoherence of flux qubits due to $1/f$ flux noise, *Phys. Rev. Lett.* **97**, 167001 (2006).

[9] J. Koch, T.M. Yu, J. Gambetta, A.A. Houck, D.I. Schuster, J. Majer, A. Blais, M.H. Devoret, S.M. Girvin, R.J. Schoelkopf "Charge insensitive qubit design derived from the Cooper pair box," Phys. Rev. A **76**, 042319 (2007).

[10] A.A. Houck, J.A. Schreier, B.R. Johnson, J.M. Chow, J. Koch, J.M. Gambetta, D.I. Schuster, L. Frunzio, M.H. Devoret, S.M. Girvin, R.J. Schoelkopf "Controlling the spontaneous emission of a superconducting transmon qubit," Phys. Rev. Lett. **101**, 080502 (2008).

[11] J. Bylander, S. Gustavsson, F. Yan, F. Yoshihara, K. Harrabi, G. Fitch, D.G. Cory, Y. Nakamura, J.S. Tsai, and W.D. Oliver, Noise spectroscopy through dynamical decoupling with a superconducting flux qubit, Nature Physics **7**, 565-570 (2011).

[12] H. Paik, D.I. Schuster, L.S. Bishop, G. Kirchmair, G. Catelani, A.P. Sears, B.R. Johnson, M.J. Reagor, L. Frunzio, L.I. Glazman, S.M. Girvin, M.H. Devoret, R.J. Schoelkopf, Observation of High Coherence in Josephson Junction Qubits Measured in a Three-Dimensional Circuit QED Architecture, Phys. Rev. Lett. **107**, 240501 (2011).

[13] C. Rigetti, J.M. Gambetta, S. Poletto, B.L.T. Plourde, J.M. Chow, A.D. Corcoles, J.A. Smolin, S.T. Merkel, J.R. Rozen, G.A. Keefe, M.B. Rothwell, M.B. Ketchen, M. Steffen, Phys. Rev. B **86**, 100506 (2012).

[14] M. Steffen, Viewpoint: superconducting qubits are getting serious, Physics **4**, 103 (2011).

[15] A.G. fowler, A.M. Stephens, and P. Groszkowski, High threshold universal quantum computation on the surface code, Phys. Ref. A **80**, 052312 (2009).

[16] D.P. DiVincenzo, Fault tolerant architectures for superconducting qubits, Phys. Scr. T **137**, 014020 (2009).

[17] A.G. Fowler, M. Mariantoni, J.M. Martinis, A.N. Cleland, Surface codes: towards practical large-scale quantum computation, Phys. Rev. A **86**, 032324 (2012).

[18] E. Lucero, M. Hofheinz, M. Ansmann, R.C. Bialczak, N. Katz, M. Neeley, A. D. OConnell, H. Wang, A. N. Cleland, and J.M. Martinis, High-Fidelity Gates in a Single Josephson Qubit, Phys. Rev. Lett. **100**, 224701 (2008).

[19] J.M. Chow, J.M. Gambetta, L. Tornberg, J. Koch, L.S. Bishop, A.A. Houck, B.R. Johnson, L. Funzio, S.M. Girvin, R.J. Schoelkopf, Randomized Benchmarking and Process Tomography for Gate Errors in a Solid-State Qubit, Phys. Rev. Lett. **102**, 119901 (2009).

[20] J.M. Chow, L. DiCarlo, J.M. Gambetta, F. Motzoi, L. Funzio, S.M. Girvin, R.J. Schoelkopf, Optimized driving of superconducting artificial atoms for improved single-qubit gates, Phys. Rev. A **82**, 040305 (2010).

[21] S. Gustavsson, O. Zwier, J. Bylander, F. Yan, F. Yoshihara, Y. Nakamura, T.P. Orlando, W.D. Oliver, Improving quantum gate fidelities by using a qubit to measure microwave pulse distortions, arXiv:1211.2175 (2011).

[22] T. Yamamoto, M. Neeley, E. Lucero, R.C. Bialczak, J. Kelly, M. Lenander, M. Mariantoni, A.D. OConnell, D. Sank, H. Wang, M. Weides, J. Wenner, Y. Yin, A.N. Cleland, J.M Martinis, Quantum process tomography of two-qubit controlled-Z and controlled-NOT gates using superconducting phase qubits, Phys. Rev. B **82**, 184515 (2010).

[23] J.M. Chow, J.M. Gambetta, A.D. Corcoles, S.T. Merkel, J.A. Smolin, C. Rigetti, S. Poletto, G.A. Keefe, M.B. Rothwell, J.R. Rozen, M.B. Ketchen, M. Steffen, Universal Quantum Gate Set Approaching Fault-Tolerant Thresholds with Superconducting Qubits, Phys. Rev. Lett. **109**, 060501 (2012).

[24] J.R. Friedman, V. Patel, W. Chen, S. K. Tolpygo, J. E. Lukens, Quantum superposition of distinct macroscopic states, Nature **406**, 43-46 (2000).

[25] C.H. van der Wal, A. C. J. ter Haar, F. K. Wilhelm, R. N. Schouten, C. J. P. M. Harmans, T. P. Orlando, S. Lloyd, J. E. Mooij, Quantum superposition of macroscopic persistent-current states, Science **290**, 773-777 (2000).

[26] A.J. Berkley, H. Xu, R. C. Ramos, M. A. Gubrud, F. W. Strauch, P. R. Johnson, J. R. Anderson, A. J. Dragt, C. J. Lobb, F. C. Wellstood, Entangled macroscopic quantum states in two superconducting qubits, Science **300**, 1548-1550 (2003).

[27] Y. Nakamura, Y.A. Pashkin, J.S. Tsai, Rabi oscillations in a large Josephson-junction charge two-level system, Phys. Rev. Lett. **87**, 246601 (2001).

[28] Y. Yu, S. Han, X. Chu, S.-I. Chu, Z. Wang, Coherent temporal oscillations of macroscopic quantum states in a Josephson junction, Science **296**, 889-892 (2002).

[29] J.M. Martinis, S. Nam, J. Aumentado, C. Urbina, Rabi oscillations in a large Josephson-junction qubit, Phys. Rev. Lett. **89**, 117901 (2002).

[30] I. Chiorescu, Y. Nakamura, C.J.P.M. Harmans, J.E. Mooij, Coherent quantum dynamics of a superconducting flux qubit, Science **299**, 1869-1871 (2003).

[31] J. Claudon, F. Balestro, F.W.J. Hekking, O. Buisson, Coherent oscillations in a superconducting multilevel quantum system, Phys. Rev. Lett. **93**, 187003 (2004).

[32] B.L.T. Plourde, T.L. Robertson, P.A. Reichardt, T. Hime, S. Linzen, C.-E. Wu, and John Clarke, Flux qubits and readout device with two independent flux lines, Phys. Rev. B **72**, 060506(R) (2005).

[33] S.Saito, T. Meno, M. Ueda, H. Tanaka, K. Semba, and H. Takayanagi, Parametric control of a superconducting flux qubit, Phys. Rev. Lett. **96**, 107001 (2006).

[34] J. Lisenfeld, A. Lukashenko, M. Ansmann, J.M. Martinis, and A.V. Ustinov, Temperature dependence of coherent oscillations in josephson phase qubits, Phys. Rev. Lett. **99**, 170504 (2007).

[35] H. Paik, S.K. Dutta, R.M. Lewis, T.A. Palomaki, B.K. Cooper, R.C. Ramos, H. Xu, A.J. Dragt, J.R. Anderson, C.J. Lobb, F.C. Wellstood, Decoherence in dc SQUID phase qubits, Phys. Rev. B **77**, 214510 (2008).

[36] Z. Kim, B. Suri, V. Zaretskey, S. Novikov, K.D. Osborn, A. Mizel, F.C. Wellstood, B.S. Palmer Decoupling a Cooper-pair box to enhance the lifetime to 0.2 ms, Phys. Rev. Lett. **106**, 120501 (2011).

[37] A. Izmalkov, M. Grajcar, E. Il'ichev, N. Oukhanski, Th. Wagner, H.-G. Meyer, W. Krech, M. H. S. Amin, A. Maassen van den Brink and A. M. Zagoskin, Observation of macroscopic Landau-Zener transitions in a superconducting device, Europhys. Lett. **65**, 844-849 (2004).

[38] W.D. Oliver, Y. Yu, J.C. Lee, K.K. Berggren, L.S. Levitov, and T.P. Orlando, Mach-Zehnder interferometry in a strongly driven superconducting qubit Science **310**, 1653 (2005).

[39] D. M. Berns, W. D. Oliver, S. O. Valenzuela, A. Shytov, K. K. Berggren, L. Levitov, and T. P. Orlando, Coherent quasiclassical dynamics of a persistent-current qubit, Phys. Rev. Lett. **97**, 150502 (2006).

[40] M. Sillanpaa, T. Lehtinen, A. Paila, Yu. Makhlin, P. Hakonen, Continuous-time monitoring of Landau-Zener interference in a Cooper-pair box, Phys. Rev. Lett. **96**, 187002 (2006).

[41] C.M. Wilson, T. Duty, F. Persson, M. Sandberg, G. Johansson, and P. Delsing, Coherent times of dressed states of a superconducting qubit under extreme driving, Phys. Rev. Lett. **98**, 257003 (2007).

[42] A. Izmalkov, S.J.W. van der Ploeg, S.N. Shevchenko, M. Grajcar, E. Il'ichev, U. Huebner, A.N. Omelyanchouk, and H.-G.Meyer, Consistency of ground state and spectroscopic measurements on flux qubits, Phys. Rev. Lett. **101**, 017003 (2008).

[43] S.N. Shevchenko, S. Ashhab, F. Nori, Landau-Zener-Stueckelberg interferometry, Phys. Rep. **492**, 1-30 (2010).

[44] S. O. Valenzuela, W. D. Oliver, D. M. Berns, K. K. Berggren, L. S. Levitov, T. P. Orlando, Microwave-induced cooling of a superconducting qubit, Science **314**, 1589-1592 (2006).

[45] A.O. Niskanen, Y. Nakamura, and J.P. Pekola, Information entropic superconducting microcooler, Phys. Rev. B **76**, 174523 (2007).

[46] J.Q. You, Yu-xi Liu, and Franco Nori, Simultaneous cooling of an artificial atom and its neighboring quantum system, Phys. Rev. Lett. **100**, 047001 (2008).

[47] M. Grajcar, S.H.W. van der Ploeg, A. Izmalkov, E. Il'ichev, H.-G. Meyer, A. Fedorov, A. Shnirman, and G. Schon, Sisyphus cooling and amplification by a superconducting qubit, Nature Phys. **4**, 612-616 (2008).

[48] J.E. Johnson, C. Macklin, D.H. Slichter, R. Vijay, E.B. Weingarten, J. Clarke, I. Siddiqi, Heralded state preparation in a superconducting qubit, Phys. Rev. Lett. **109**, 050506 (2012).

[49] D. Riste, J.G. van Leeuwen, H.S. Ku, K.W. Lehnert, L. DiCarlo, Initialization by measurement of a superconducting quantum bit circuit, Phys. Rev. Lett. **109**, 050507 (2012).

[50] D.M. Berns, M.S. Rudner, S.O. Valenzuela, K. K. Berggren, W. D. Oliver, L. S. Levitov, T. P. Orlando, Amplitude spectroscopy of a solid-state artificial atom, Nature **455**, 51-57 (2008).

[51] M.S. Rudner, A.V. Shytov, L. S. Levitov, D. M. Berns, W. D. Oliver, S. O. Valenzuela, T. P. Orlando, Quantum phase tomography of a strongly driven qubit, Phys. Rev. Lett. **101**, 190502 (2008).

[52] K.V.R.M. Murali, Z. Dutton, W.D. Oliver, D.S. Crankshaw, and T.P. Orlando, "Probing decoherence with electromagnetically induced transparency in superconductive quantum circuits," Phys. Rev. Lett. **93**, 087003 (2004).

[53] Z. Dutton, K.V.R.M. Murali, W.D. Oliver, and T.P. Orlando, Electromagnetically induced transparency in superconducting quantum circuits: effects of decoherence, tunneling, and multilevel crosstalk, Phys. Rev. B **73**, 104516 (2006).

[54] W.R. Kelly, Z. Dutton, J. Schlafer, B. Mookerji, T.A. Ohki, J.S. Kline, D.P. Pappas, Direct observation of coherent population trapping in a superconducting artificial atom, Phys. Rev. Lett. **104**, 163601 (2010).

[55] P.J. Leek, J.M. Fink, A. Blais, R. Bianchetti, M. Goppl, J.M. Gambetta, D.I. Schuster, L. Frunzio, R.J. Schoelkopf, and A. Wallraff, Observation of Berry's phase in a solid-state qubit, Science **318**, 1889-1892 (2007).

[56] I. Chiorescu, P. Bertet, K. Semba, Y. Nakamura, C.J.P.M. Harmans, and J.E. Mooij, Coherent dynamics of a flux qubit coupled to a harmonic oscillator, Nature **431**, 159-162 (2004).

[57] A. Wallraff, D. I. Schuster, A. Blais, L. Frunzio, R.-S. Huang, J. Majer, S. Kumar, S. M. Girvin and R. J. Schoelkopf, Strong coupling of a single photon to a superconducting qubit using circuit quantum electrodynamics, Nature **431**, 162-167 (2004).

[58] J. Johansson, S. Saito, T. Meno, H. Nakano, M. Ueda, H. Tanaka, K. Semba, and H. Takayanagi, Vacuum rabi oscillations in a macroscopic superconducting qubit LC oscillator system, Phys. Rev. Lett. **96**, 127006 (2006).

[59] F. Deppe, M. Mariantoni, E.P. Menzel, A. Marx, S. Saito, K. Kakuyanagi, H. Tanaka, T. Menon, K. Semba, H. Takayanagi, E. Solano, and R. Gross, Two-photon probe of the Jaynes-Cummings model and controlled symmetry breaking in circuit QED, Nature Phys. **4**, 686-691 (2008).

[60] J.M. Fink, M. Goppl, M. Baur, R. Bianchetti, P.J. Leek, A. Blais, and A. Wallraff, Climbing the Jaynes-Cummings ladder and observing its root n nonlinearity in a cavity QED system, Nature **454**, 315-318 (2008).

[61] A. Fragner, M. Goppl, J.M. Fink, M. Baur, R. Bianchetti, P.J. Leek, A. Blais, and A. Wallraff, Resolving vacuum fluctuations in an electrical circuit by measuring the Lamb shift, Science **322**, 1357-1360 (2008).

[62] M. Hofheinz, E.M. Weig, M. Ansmann, R.C. Bialczak, E. Lucero, M. Neeley, A.D. O'Connell, H. Wang, J.M. Martinis, and A.N. Cleland, Generation of Fock states in a superconducting quantum circuit, Nature **454**, 310-314 (2008).

[63] R.J. Schoelkopf and S.M. Girvin, Wiring up quantum systems, Nature **451**, 664-669 (2008).

[64] Y. Makhlin, G. Schon, A. Shnirman, Quantum-state engineering with Josephson-junction devices, Rev. Mod. Phys. **73**, 357-400 (2001).

[65] J. E. Mooij, The road to quantum computing, Science **307**, 1210-1211 (2005).

[66] T.D. Ladd, F. Jelezko, R. Laflamme, Y. Nakamura, C. Monroe, and J.L. OBrien, Quantum computers, Nature **451**, 664-669 (2008).

[67] T. Hime, P.A. Reichart, B.L.T. Plourde, T.L. Robertson, C.-E. Wu, A.V. Ustinov, and J. Clarke, Solid-state qubits with current-controlled coupling, Science **314**, 1427-1429 (2006).

[68] S.H.W. van der Ploeg, A. Izmalkov, A. Maassen van den Brink, U. Huebner, M. Grajcar, E. Il'ichev, H.-G. Meyer, and A.M. Zagoskin, Controllable coupling of superconducting flux qubits, Phys. Rev. Lett. **98**, 057004 (2007).

[69] A.O. Niskanen, K. Harrabi, F. Yoshihara, Y. Nakamura, S. Lloyd, and J.S. Tsai, Quantum coherent tunable coupling of superconducting qubits, Science **316**, 723-726 (2007).

[70] A.J. Kerman and W.D. Oliver, High-fidelity quantum operations on superconducting qubits in the presence of noise, Phys. Rev. Lett. **101**, 070501 (2008).

[71] J.M. Chow, A.D. Corcoles, J.M. Gambetta, C. Rigetti, B.R. Johnson, J.A. Smolin, J.R. Rozen, G.A. Keefe, M.B. Rothwell, M.B. Ketchen, M. Steffen, Simple All-Microwave Entangling Gate for Fixed-Frequency Superconducting Qubits, Phys. Rev. Lett. **107**, 080502 (2011).

[72] P.C. de Groot, J. Lesnfeld, R.N. Schouten, S. Ashhab, A. Lupascu, C.J.P.M. Harmans, J.E. Mooij, Selective darkening of degenerate transitions demonstrated with two superconducting quantum bits, Nature Phys. **10**, 763-766 (2010).

[73] M.A. Sillanpaa, J.I. Park, and R.W. Simmonds, "Coherent quantum state storage and transfer between two phase qubits via a resonant cavity," Nature **449**, 438-442 (2007).

[74] J. Majer, J.M. Chow, J.M. Gambetta, J. Koch, B.R. Johnson, J.A. Schreier, L. Frunzio, D.I. Schuster, A.A. Houck, A. Wallraff, A. Blais, M.H. Devoret, S.M. Girvin, and R.J. Schoelkopf, "Coupling superconducting qubits via a cavity bus," Nature **449**, 443-447 (2007).

[75] Y.A. Pashkin, T. Yamamoto, O. Astafiev, Y. Nakamura, D. V. Averin, and J. S. Tsai, "Quantum oscillations in two coupled charge qubits," Nature **421**, 823-826 (2003).

[76] T. Yamamoto, Yu. A. Pashkin, O. Astafiev, Y. Nakamura, J. S. Tsai, "Demonstration of conditional gate operation using superconducting charge qubits," Nature **425**, 941-944 (2003).

[77] R. McDermott, R. W. Simmonds, M. Steffen, K. B. Cooper, K. Cicak, K.D. Osborn, S. Oh, D. P. Pappas, J. M. Martinis, "Simultaneous state measurement of coupled Josephson phase qubits," Science **307**, 1299-1302 (2005).

[78] J.H. Plantenberg, P.C. de Groot, C.J.P.M. Harmans, and J.E. Mooij, "Demonstration of controlled-NOT quantum gates on a pair of superconducting quantum bits," Nature **447**, 836-839 (2007).

[79] M. Neeley, R.C. Bialczak, M. Lenander, E. Lucero, M. Mariantoni, A.D. OConnell, D. Sank, H. Wang, M. Weides, J. Wenner, Y. Yin, T. Yamamoto, A.N. Cleland, J.M. Martinis, Generation of three-qubit entangled states using superconducting phase qubits, Nature **467**, 570-573 (2010).

[80] L. DiCarlo, M.D. Reed, L. Sun, B.R. Johnson, J.M. Chow, J.M. Gambetta, L. Frunzio, S.M. girvin, M.H. Devoret, R.J. Schoelkopf, Preparation and measurement of three-qubit entanglement in a superconducting circuit, Nature **467**, 574-578 (2010).

[81] M. Steffen, M. Ansmann, R.C. Bialczak, N. Katz, E. Lucero, R. McDermott, M. Neeley, E.M. Weig, A.N. Cleland, and J. M. Martinis, Measurement of the entanglement of two superconducting qubits via state tomography, Science **313**, 1423-1425 (2006).

[82] M. Steffen, M. Ansmann, R. McDermott, N. Katz, R.C. Bialczak, E. Lucero, M. Neeley, E.M. Weig, A.N. Cleland, and J. M. Martinis, State tomography of capacitively shunted phase qubits with high fidelity, Phys. Rev. Lett. **97**, 050502 (2006).

[83] M. Neeley, M. Ansmann, R.C. Bialczak, M. Hofheinz, N. Katz, E. Lucero, A. O'Connell, H. Wang, A.N. Cleland, and J. M. Martinis, "Process tomography of quantum memory in a Josephson-phase qubit coupled to a two-level state," Nature Phys. **4**, 523-526 (2008).

[84] J.M. Chow, J.M. Gambetta, A.D. Corcoles, S.T. Merkel, J.A. Smolin, C.Rigetti, S. Poletto, G.A. Keefe, M.B. Rothwell, J.R. Rozen, M.B. Ketchen, M. Steffen, Universal quantum gate set approaching fault-tolerant thresholds with superconducting qubits, Phys. Rev. Lett. **109**, 060501 (2012).

[85] R.J. Schoelkopf, P. Wahlgren, A.A. Kozhevnikov, P. Delsing, D.E. Prober, "The radio-frequency single-electron transistor (RF-SET): a fast and ultrasensitive electrometer," Science **280**, 1238-1242 (1998).

[86] I. Siddiqi, R. Vijay, F. Pierre, C.M. Wilson, M. Metcalfe, C. Rigetti, L. Frunzio, and M.H. Devoret, "RF-driven Josephson bifurcation amplifier for quantum measurement," Phys. Rev. Lett. **93**, 297992 (2004).

[87] J.C. Lee, W.D. Oliver, T.P. Orlando, K.K. Berggren, "Resonant readout of a persistent current qubit," IEEE Trans. Appl. Supercond. **15**, 841-844 (2004).

[88] I. Siddiqi, R. Vijay, F. Pierre, C.M. Wilson, L. Frunzio, M. Metcalfe, C. Rigetti, R.J Schoelkopf, M.H. Devoret, D. Vion, D. Esteve, "Direct observation of dynamical bifurcation between two driven oscillation states of a Josephson junction," Phys. Rev. Lett. **94**, 027005 (2005).

[89] M.A. Sillanpää, T. Lehtinen, A. Paila, Yu. Makhlin, L. Roschier, P.J. Hakonen, "Direct observation of a Josephson capacitance," Phys. Rev. Lett. **95**, 206806 (2005).

[90] N. Katz, M. Ansmann, R.C. Bialczak, E. Lucero, R. McDermott, M. Neeley, M. Steffen, E.M. Weig, A.N. Cleland, J.M. Martinis, A.N. Korotkov, "Coherent state evolution in a superconducting qubit from partial-collapse measurement," Science 312, 1498-1500 (2006).

[91] J.C. Lee, W.D. Oliver, K.K. Berggren, T.P. Orlando, "Nonlinear resonant behavior of a dispersive readout circuit for a superconducting flux qubit," Phys. Rev. B **75**, 144505 (2007).

[92] A. Lupascu, S. Saito, T. Picot, P.C. de Groot, C.J.P.M. Harmans, J.E. Mooij, "Quantum non-demolition measurement of a superconducting two-level system," Nature Phys. **3**, 119-123 (2007).

[93] T. Yamamoto, K. Inomata, M. Watanabe, K. Matsuba, T. Miyazaki, W.D. Oliver, Y. Nakamura, and J.S. Tsai, "Flux-driven Josephson parametric amplifier," Appl. Phys. Lett. **93**, 042510 (2008).

[94] M.A. Castellanos-Beltran, K.D. Irwin, G.C. Hilton, L.R. Vale, and K.W. Lehnert, "Amplification and squeezing of quantum noise with a tunable Josephson metamaterial," Nature Phys. **4**, 929-931 (2008).

[95] O. Naaman, J. Aumentado, L. Friedland, J.S. Wurtele, I. Siddiqi, "Phase-locking transition in a chirped superconducting Josephson resonator," Phys. Rev. Lett. **101**, 117005 (2008).

[96] M.D. Reed, L. DiCarlo, B.R. Johnson, L. Sun, D.I. Schuster, L. Frunzio, R.J. Schoelkopf, High-fidelity readout in circuit quantum electrodynamics using the Jaynes-Cummings nonlinearity, Phys. Rev. Lett. **105**, 173601 (2010).

[97] N. Bergeal, F. Schackert, M. Metcalfe, R. Vijay, V.E. Manucharyan, L. Frunzio, D.E. Prober, R.J. Schoelkopf, S.M. Girvin, M.H. Devoret, Phase-preserving amplification near the quantum limit with a Josephson ring modulator, Nature **465**, 64-70 (2010).

[98] M. Mariantoni, H. Wang, T. Yamamoto, M. Neeley, R.C. Bialczak, Y. Chen, M. Lenander, E. Lucero, A.D. OConnell, D. Sank, M. Weides, J. Wenner, Y. Yin, J. Zhao, A.N Korotkov, A.N. Cleland, J.M. Martinis, Implementing the quantum von Neumann architecture with superconducting circuits, Science **333**, 61-65 (2011).

[99] A. Galiautdinov, A.N Korotkov, J.M. Martinis, Resonator-zero-qubit architecture for superconducting qubits, Phys. Rev. A **85**, 042321 (2012).

[100] M.D. Reed, L. DiCarlo, S.E. Nigg, L. Sun, L. Frunzio, S.M. Girvin, R.J. Schoelkopf, Realization of three-qubit quantum error correction with superconducting circuits, Nature **482**, 382-385 (2012).

[101] L. DiCarlo, J.M. chow, J.M. Gambeteta, L.S. Bishop, B.R. Johnson, D.I. Schuster, J. Majer, A. Blais, L. Frunzio, S.M. Girvin, R.J. Schoelkopf, Demonstration of two-qubit algorithms with a superconducting quantum processor, Nature **460**, 240-244 (2009).

[102] E. Lucero, R. Barends, Y. Chen, J. Kelly, M. Mariantoni, A. Megrant, P. OMalley, D. Sank, A. Vainsencher, J. Wenner, T. White, Y. Yin, A.N. Cleland, J.M. Martinis, Computing prime factors with a Josephson phase qubit quantum processor, Nature Phys. **8**, 719-723 (2012).

[103] A. Barone, G. Paterno, *Physics and applications of the Josephson effect* (John Wiley and Sons, New York, 1982).

[104] T.P. Orlando and K.A. Delin, *Foundations of applied superconductivity* (Prentice Hall, 1991)

[105] T. Van Duzer, C.W. Turner, *Principles of superconductive Devices and Circuits* (Elsevier, New York, 1998)

[106] M. Tinkham, *Introduction to Superconductivity* (Dover, 2004)

[107] W.C. Stewart, "Current-voltage characteristics of Josephson junctions," Appl. Phys. Lett. **12**, 277-280 (1968).

[108] D.E. McCumber, "Effect of ac impedance on dc voltage-current characteristics of superconductor weak-link junctions," J. Appl. Phys. **39**, 3113-3119 (1968).

[109] J. Lisenfeld, *Experiments on superconducting Josephson phase quantum bits* (Friedrich-Alexander-Universität Erlangen-Nürnberg, 2007).

[110] V. Ambegaokar, A. Baratoff, "Tunneling between superconductors," Phys. Rev. Lett. **10**, 486-489 (1963).

[111] H.A. Kramers, "Brownian motion in a field of force and the diffusion model of chemical reactions," Physica **7**, 284 (1940).

[112] M. Büttiker, E. Harris, R. Landauer, "Thermal activation in extremely underdamped Josephson-junction circuits," Phys. Rev. B **28**, 1268-1275 (1983).

[113] M.H. Devoret, J.M. Martinis, D. Esteve, J. Clarke, "Resonant activation from the zero-voltage state of a current-biased Josephson junction," Phys. Rev. Lett. **53**, 1260-1263 (1984).

[114] J.M. Martinis, M.H. Devoret, J. Clarke, "Energy-level quantization in the zero-voltage state of a current-biased Josephson junction," Phys. Rev. Lett. **55**, 1543-1546 (1985).

[115] M.H. Devoret, J.M. Martinis, J. Clarke, "Measurements of macroscopic quantum tunneling out of the zero-voltage state of a current-biased Josephson junction," Phys. Rev. Lett. **55**, 1908-1911 (1985).

[116] J.M. Martinis, M.H. Devoret, J. Clarke, "Experimental tests for the quantum behavior of a macroscopic degree of freedom: the phase difference across a Josephson junction," Phys. Rev. B **35**, 4682-4698 (1985).

[117] T.A. Fulton, L.N. Dunkleberger "Lifetime of the zero-voltage state in Josephson tunnel junctions," Phys. Rev. B **9**, 4760 (1974).

[118] J. Clarke, A.I. Braginski (ed.), *The SQUID Handbook, vol.1* (Wiley-VCH, New York, 1982).

[119] R.C. Dynes, r.A. Fulton "Supercurrent density distribution in Josephson junctions," Phys. Rev. B **3**, 3015 (1971).

[120] W.T. Tsang, T. van Duzer "D.C. analysis of parallel arrays of two and three Josephson junctions," J. Appl. Phys. **46**, 4573 (1975).

[121] H. Grabert, M.H. Devoret (ed.) *Single charge tunneling: Coulomb blockade phenomena in nanostructures* (Springer, 1992).

[122] P. Joyez, P. Lafarge, A. Filipe, D. Esteve, M.H. Devoret, "Observation of parity-induced suppression of Josephson tunneling in the superconducting single electron transistor," Phys. Rev. Lett. **72**, 2458-2461 (1994).

[123] D. Flees, S. Han, J. Lukens, "Interband transitions and band gap measurements in Bloch transistors," Phys. Rev. Lett. **78**, 4817-4820 (1997).

[124] Y. Nakamura, C.D. Chen, J.S. Tsai, "Spectroscopy of energy-level splitting between two macroscopic quantum states of charge coherently superposed by Josephson tunneling," Phys. Rev. Lett. **79**, 2328-2331 (1997).

[125] V. Bouchiat, D. Vion, P. Joyez, D. Esteve, M.H. Devoret, "Quantum coherence with a single Cooper pair," Physica Scripta T **76**, 165-170 (1998).

[126] F. Motzoi, J.M. Gambetta, P. Rebentrost, F.K. Wilhelm, Simple pulses for elimination of leakage in weakly nonlinear qubits, Phys. Rev. Lett. 103, 110501 (2009).

[127] J. E. Mooij, T. P. Orlando, L. S. Levitov, L. Tian, C. H. van der Wal, S. Lloyd, "Josephson persistent-current qubit," Science **285**, 1036-1039 (1999).

[128] T. P. Orlando, J. E. Mooij, L. Tian, C. H. van der Wal, L. S. Levitov, S. Lloyd, and J. J. Mazo, "Superconducting persistent-current qubit," Phys. Rev. B **60**, 15398-15413 (1999).

[129] M. Steffen, S. Kumar, D.P. DiVincenzo, J.R. Rozen, G.A. Keefe, M.B. Rothwell, M.B. Ketchen, High-coherence hybrid superconducting qubit, Phys. Rev. Lett. 105, 100502 (2010).

[130] K.B. Cooper, M. Steffen, R. McDermott, R.W. Simmonds, S. Oh, D.A. Hite, D.P. Pappas, J.M. Martinis, Observation of quantum oscillations between a Josephson phase qubit and a microscopic reonator using fast readout, Phys. Rev. Lett. 93, 180401 (2004).

[131] M.H. Devoret, J.M. Martinis, Implementing qubits with superconducting integrated circuits, Quantum Inf. Proc. 3, 163-203 (2004).

[132] J.M. Martinis, K.B. Cooper, R. McDermott, M. Steffen, M. Ansmann, K.D. Osborn, K. Cicak, S. Oh, D.P. Pappas, R.W. Simmonds, C.C. Yu, Decoherence in Josephson qubits from dielectric loss, Phys. Rev. Lett. 95, 210503 (2005).

[133] M. Steffen, M. Ansmann, R. McDermott, N. Katz, R.C. Bialczak, E. Lucero, M. Neeley, E.M. Weig, A.N. Cleland, J.M. Martinis, State tomography of capacitively shunted phase qubits with high fidelity, Phys. Rev. Lett. 97, 050502 (2006).

[134] J.M. Martinis, Superconducting phase qubits, Quant. Info. Proc. 8, 81-103 (2009).

[135] V.E. Manucharyan, J. Koch, L. Glazman, M.H. Devoret, Fluxonium: single Cooper-pair circuit free of charge offsets, Science 326, 113-116 (2009).

[136] V.E. Manucharyan, N.A. Masluk, A. Kamal, J. Koch, L. Glazman, M.H. Devoret, Evidence for coherent quantum phase slips across a Josephson junction array, Phys. Rev. B 85, 024521 (2012).

[137] A.J. Kerman, E.A. Dauler, W.E. Keicher, J.K.W. Yang, K.K. Berggren, G. Gol'tsman, B. Voronov Kinetic-inductance-limited reset time of a superconducting nanowire photon source, Appl. Phys. Lett. 88, 111116 (2006).

[138] F. Yan, J. Bylander, S. Gustavsson, F. Yoshihara, K. Harrabi, D.G. Cory, T.P. Orlando, Y. Nakamura, J.S. Tsai, W.D. Oliver Spectroscopy of low-frequency noise and its temperature dependence in a superconducting qubit, Phys. Rev. B 85, 174521 (2012).

[139] F. Yan, S. Gustavsson, J. Bylander, X. Jin, F. Yoshihara, D.G. Cory, Y. Nakamura, T.P. Orlando, W.D. Oliver $T_{1\rho}$ experiment as a noise spectrum analyzer of a superconducting qubit undrergoing driven evolution, under review (2013).

[140] S. Gustavsson, J. Bylander, F. Yan, P. Forn-Diaz, V. Bolkovsky, D. Braje, G. Fitch, K. Harrabi, D. Lennon, J. Miloshi, P. Murphy, R. Slattery, S. Spector, B. Turek, T. Weir, P.B. Welander, F. Yoshihara, D.G. Cory, Y. Nakamura, T.P. Orlando, W.D. Oliver Driven dynamics and rotary echo of a qubit tunably coupled to a harmonic oscillator, Phys. Rev. Lett. 108, 170503 (2012).

[141] L.D. Landau, "On the theory of transfer of energy at collisions II," Phys. Z. USSR **2**, 46-51 (1932).

[142] C. Zener, "Non-adiabatic crossing of energy levels," Proc. R. Soc. Lond. A **137**, 696-702 (1932).

[143] E. C. G. Stueckelberg, Helv. Phys. Acta **5**, 369-422 (1932).

[144] H. Nakamura, *Nonadiabatic Transition* (London, England: World Scientific, 2001).

[145] M. Grifoni and P. Hänggi, "Driven quantum tunneling," Phys. Rep. **304**, 229-354 (1998).

[146] Y. Kayanuma, "Phase coherence and nonadiabatic transition at a level crossing in a periodically driven two-level system," Phys. Rev. B **47**, 9940-9943 (1993).

[147] Y. Kayanuma, "Role of phase coherence in the transition dynamics of a periodically driven two-level system," Phys. Rev. B **50**, 843-845 (1994).

[148] Y. Kayanuma, "Stokes phase and geometrical phase in a driven two-level system," Phys. Rev. A **55**, R2495-R2498 (1997).

[149] Y. Kayanuma and Y. Mizumoto, "Landau-Zener transitions in a level-crossing system with periodic modulation of the diagonal energy," Phys. Rev. A **62**, 061401(R) (2000).

[150] A. V. Shytov, D. A. Ivanov, M. V. Feigel'man, "Landau-Zener interferometry for qubits," Eur. Phys. J. B **36**, 263-269 (2003)

[151] S. Ashhab, J.R. Johansson, A.M. Zagoskin, and Franco Nori, "Two-level systems driven by large-amplitude fields," Phys. Rev. A **75**, 063414 (2007).

[152] M. Wubs, K. Saito, S. Kohler, P. Hänggi, and Y. Kayanuma, "Gauging a quantum heat bath with dissipative Landau-Zener Transitions," Phys. Rev. Lett. **97**, 200404 (2006).

[153] K. Saito, M. Wubs, S. Kohler, P. Hänggi, and Y. Kayanuma, "Quantum state preparation in circuit QED via Landau-Zener tunneling," Europhys. Lett. **76**, 22-28 (2006).

[154] K. Saito, M. Wubs, S. Kohler, Y. Kayanuma, and P. Hänggi, "Dissipative Landau-Zener transitions of a qubit: bath-specific and universal behavior," Phys. Rev. B **75**, 214308 (2007).

[155] F. Grossmann, T. Dittrich, P. Jung, and P. Hänggi "Coherent destruction of tunneling," Phys. Rev. Lett. **67**, 516-519 (1991).

[156] J.M. Gomez Llorente and J. Plata, "Tunneling control in a two-level system," Phys. Rev. A **45**, R6958-R6961 (1992).

[157] Y. Kayanuma and K. Saito, "Coherent destruction of tunneling, dynamic localization, and the Landau-Zener formula," Phys. Rev. A **77**, 010101(R) (2008).

[158] W. G. van der Wiel, *et al.*, "Electron transport through double quantum dots," Rev. Mod. Phys. **75**, 1-22 (2003).

[159] R. Hanson, L.P. Kouwenhoven, J.R. Petta, S. Tarucha, and L.M.K. Vandersypen "Spins in few-electron quantum dots," Rev. Mod. Phys. **79**, 1217-1265 (2007).

[160] C. Cohen-Tannoudji, J. Dupont-Roc, and G. Grynberg, *Atom-Photon Interactions: Basic Processes and Applications* Ch. 6 (Wiley, 1992).

[161] F.R. Friedman, *et al.*, "Macroscopic measurement of resonant magnetization tunnelling in high-spin molecules," Phys. Rev. Lett. **76**, 3830-3833 (1996).

[162] L. Thomas, *et al.*, "Macroscopic quantum tunnelling of magnetization in a single crystal of nanomagnets," Nature **383**, 145-147 (1996).

[163] W. Wernsdorfer and R. Sessoli, "Quantum phase interference and parity effects in magnetic molecular clusters," Science **284**, 133-135 (1999).

[164] M. C. Baruch, T. F. Gallagher, "Ramsey interference fringes in single pulse microwave multiphoton transitions," Phys. Rev. Lett. **68**, 3515-3518 (1992).

[165] S. Yoakum, L. Sirko, P. M. Koch, "Stückelberg oscillations in the multiphoton excitation of helium Rydberg atoms: Observation with a pulse of coherent, field and suppression by additive noise," Phys. Rev. Lett. **69**, 1919-1922 (1992).

[166] M. Mark, T. Kraemer, P. Waldburger, J. Herbig, C.Chin, H.-C. Nägerl, and R. Grimm "Stückelberg interferometry" with ultracold molecules," Phys. Rev. Lett. **99**, 113201 (2007).

[167] M. Mark, F. Ferlaino, S. Knoop, J.G. Danzl, T. Kraemer, C.Chin, H.-C. Nägerl, and R. Grimm, "Spectroscopy of ultracold trapped cesium Feshbach molecules," Phys. Rev. A **76**, 042514 (2007).

[168] F. Lang, P.V.D. Straten, B. Brandstätter, G. Thalhammer, K. Winkler, P.S. Julienne, R. Grimm, and J. Hecker Denschlag, "Cruising through molecular bound-state manifolds with radiofrequency," Nature Physics **4**, 223-226 (2008).

[169] P. K. Tien and J. P. Gordon, "Multiphoton process observed in the interaction of microwave fields with the tunneling between superconductor films," Phys. Rev. **129**, 647 (1963).

[170] L. P. Kouwenhoven, S. Jauhar, J. Orenstein, P. L. McEuen, Y. Nagamune, J. Motohisa, and H. Sakaki, "Observation of Photon-Assisted Tunneling through a Quantum Dot," Phys. Rev. Lett. **73**, 3443 (1994).

[171] Y. Nakamura, J. S. Tsai, *J. Supercond.* **12**, 799 (1999).

[172] O. Astafiev, K. Inomata, A.O. Niskanen, T. Yamamoto, Yu. A. Pashkin, Y. Nakamura, and J.S. Tsai, "Single artificial-atom lasing," Nature **449**, 588-590 (2007).

[173] A.O. Niskanen, Y. Nakamura, and J.P. Pekola, "Information entropic superconducting microcooler," Phys. Rev. B **76**, 174523 (2007).

[174] A.L. Schawlow, "Spectroscopy in a new light," Rev. Mod. Phys. **54**, 697-707 (1982).

[175] R.C. Thompson, "High resolution laser spectroscopy of atomic systems," Rep. Prog. Phys. **48**, 531-578 (1985).

[176] R.K. Wangsness, F. Bloch, "The Dynamical Theory of Nuclear Induction," Phys. Rev. **89**, 728-739 (1953).

[177] F. Bloch, "The Dynamical Theory of Nuclear Induction," Phys. Rev. **105**, 1206-1222 (1957).

[178] A.G. Redfield, "On the theory of relaxation processes," IBM Journal of Research and Development **1**, 19 (1957).

[179] Y. Makhlin, "Dephasing of qubits by transverse low-frequency noise," JETP Letters **78**, 497 (2003).

[180] A. Shnirman, G. Schön, I. Martin, Y. Makhlin, "Low- and High-Frequency Noise from Coherent Two-Level Systems," Phys. Rev. Lett. **94**, 127002 (2005).

[181] G. Ithier, *Manipulation, lecture et analyse de la décohérence d'un bit quantique supraconducteur* (Ph.D. thesis, Université Paris VI, 2005).

[182] J.Q. You, X. Hu, S. Ashhab, F. Nori, "Low-decoherence flux qubit," Phys. Rev. B **75**, 140515 (2007).

[183] A.J. Kerman, "Metastable superconducting qubit," Phys. Rev. Lett. **104**, 027002 (2010).

[184] H.A. Haus, *Electromagnetic noise and quantum optical measurements* (Springer, New York 2000).

[185] A.A. Clerk, M.H. Devoret, S.M. Girvin, F. Marquardt, R.J. Schoelkopf, "Introduction to quantum noise, measurement and amplification," Rev. Mod. Phys. **82**, 1155-1208 (2010).

[186] F. Yan, S.Gustavsson, J. Bylander, X. Jin, F. Yoshihara, D.G. Cory, Y. Nakamura, T.P. Orlando, W.D. Oliver, "$T_{1\rho}$ experiment as a noise spectrum analyzer during driven evolution," in preparation (2013).

[187] "Quantum noise in the Joseephson charge qubit," Phys. Rev. Lett. **93**, 267007 (2004).

[188] F. Yoshihara, *et al.*, in preparation (2013).

[189] G.S. Uhrig, "Keeping a Quantum Bit Alive by Optimized π-Pulse Sequences," Phys. Rev. Lett. **98**, 100504 (2007).

[190] M.J. Biercuk, H. Uys, A.P. VanDevender, N. Shiga, W.M. Itano, J.J. Bollinger, "Optimized dynamical decoupling in a model quantum memory," Nature **458**, 996-1000 (2009).

[191] J.M. Martinis, S. Nam, J. Aumentado, K.M. Lang, C. Urbina, "Decoherence of a superconducting qubit due to bias noise," Phys. Rev. B **67**, 094510 (2003).

[192] L. Cywiński, R.M. Lutchyn, C.P. Nave, S. Das Sarma, "How to enhance dephasing time in superconducting qubits," Phys. Rev. B **77**, 174509 (2008).

[193] M.J. Biercuk, H. Uys, A.P. VanDevender, N. Shiga, W.M. Itano, J.J. Bollinger, "Experimental Uhrig dynamical decoupling using trapped ions," Phys. Rev. A **79**, 062324 (2009).

[194] G.S. Uhrig, "Exact results on dynamical decoupling by π pulses in quantum information processes," New J. Phys. **10**, 083024 (2008).

[195] B. Yurke, J.S. Denker, "Quantum network theory," Phys. Rev. A **29**, 1419-1437 (1984).

[196] M.H. Devoret, "Quantum fluctuations in electrical circuits" in *Quantum Fluctuations*, Les Houches Session LXIII (Elsevier, 1997).

[197] A. Cottet, *Implementation of a quantum bit in a superconducting circuit*, (Ph.D. thesis, Saclay, 2002).